



Università degli Studi di Ferrara  
Dottorato di Ricerca in Fisica, ciclo XXIV  
Coordinatore Prof. Filippo Frontera

# **Development of a new trigger system for spin-filtering studies**

TUTORE:  
Dr. Paolo Lenisa

DOTTORANDO:  
Paolo Benati

Anni 2009/2011



# Contents

<b>Abstract</b>	<b>5</b>
<b>Riassunto</b>	<b>7</b>
<b>Introduction</b>	<b>9</b>
<b>1 Physics motivations</b>	<b>13</b>
1.1 Hadron structure at the partonic level . . . . .	13
1.1.1 The spin structure of the proton . . . . .	13
1.1.2 Transversity and polarized antiprotons . . . . .	14
1.2 Magnetic and electric form factors . . . . .	16
1.2.1 The form factors of the protons . . . . .	16
1.2.2 Measurements with antiprotons . . . . .	17
1.3 Spectroscopy of hadrons . . . . .	19
1.4 Antinucleon-nucleon scattering and reactions . . . . .	20
1.4.1 Double polarized hard antiproton-proton scattering . . . . .	20
<b>2 Production of polarized antiprotons</b>	<b>23</b>
2.1 How to polarize antiprotons . . . . .	24
2.2 Spin filtering method . . . . .	27
2.2.1 Filtering polarization cross section . . . . .	29
2.2.2 Estimation of the polarization build-up for COSY . . . . .	32
2.2.3 Antiprotons: theoretical cross section predictions . . . . .	32
<b>3 Spin-filtering studies at COSY</b>	<b>35</b>
3.1 Spin filtering cycle . . . . .	37
3.2 The COSY ring . . . . .	39
3.2.1 Beam lifetime and acceptance . . . . .	40
3.2.2 Beam polarization lifetime and spin flipper efficiency . . . . .	41
3.3 PAX experimental setup . . . . .	42

3.3.1	Atomic beam source . . . . .	43
3.3.2	Target gas analyzer and Breit-Rabi polarimeter . . . . .	44
3.3.3	Target chamber and vacuum system . . . . .	45
3.3.4	Holding field . . . . .	46
3.3.5	Beam polarimeter . . . . .	47
3.3.6	Detectors . . . . .	50
3.3.7	Front-end electronics . . . . .	50
3.4	Extraction of effective polarizing cross-section $\tilde{\sigma}_1$ . . . . .	51
<b>4</b>	<b>Ferrara trigger board</b>	<b>53</b>
4.1	Trigger board description . . . . .	54
4.1.1	Digital-to-Analog Converter . . . . .	55
4.1.2	Timing devices . . . . .	56
4.1.3	Complex Programmable Logic Device . . . . .	58
4.1.4	Field Programmable Gate Array . . . . .	59
4.1.5	PAX_TB control software . . . . .	60
4.2	Trigger board commissioning . . . . .	64
4.2.1	Laboratory: 1 <sup>st</sup> phase . . . . .	64
4.2.2	Jitter tests . . . . .	67
4.2.3	Crosstalk test . . . . .	72
4.2.4	Laboratory: 2 <sup>nd</sup> phase . . . . .	74
4.2.5	Jitter tests . . . . .	78
4.2.6	Crosstalk tests . . . . .	83
4.2.7	Laboratory tests conclusions . . . . .	86
4.2.8	Final commissioning . . . . .	86
	<b>Conclusions</b>	<b>95</b>
<b>A</b>	<b>Detectors</b>	<b>97</b>
A.1	Thin detectors (69 $\mu m$ , 300 $\mu m$ ) . . . . .	97
A.2	Thick detectors (5500 $\mu m$ ) . . . . .	99
A.3	Front-end electronics . . . . .	100
A.4	Cooling . . . . .	103
A.5	Assembly . . . . .	104
A.6	Geometry . . . . .	105
	<b>List of Figures</b>	<b>114</b>
	<b>Bibliography</b>	<b>115</b>
	<b>Acknowledgements</b>	<b>121</b>

# Abstract

Polarized antiprotons allow unique access to a number of fundamental physics observables. One example is the transversity distribution which is the last missing piece to complete the knowledge of the nucleon partonic structure at leading twist in the QCD-based parton model. The transversity is directly measurable via Drell-Yan production in double polarized antiproton-proton collisions. This and a multitude of other findings, which are accessible via  $\vec{p}\vec{\bar{p}}$  scattering experiments, led the **Polarized Antiproton eXperiments (PAX) Collaboration** to propose such investigations at the **High Energy Storage Ring (HESR) of the Facility for Antiproton and Ion Research (FAIR)**. Furthermore the production of intense polarized antiproton beams is still an unsolved problem, which is the core of the PAX proposal.

In this frame, an intense work on the feasibility of this ambitious project is going on at **COSY (COoler SYnchrotron of the Institut für KernPhysik –IKP– of the Forschungs Zentrum Jülich) (FZJ)** where the work of this thesis has been performed.

Presently, the only available method to polarize an antiproton beam is by means of the mechanism of spin-filtering exploiting the spin dependence of the  $(p\bar{p})$  interaction via the repeated interaction with a polarized hydrogen target. Since the total cross section is different for parallel and antiparallel orientation of the beam particle spins relative to the direction of the target polarization, one spin direction is depleted faster than the other, so that the circulating beam becomes increasingly polarized, while the intensity decreases with time.

A spin-filtering experiment with protons has been prepared and finally realized in 2011 at the COSY ring in Jülich. Aims of the spin-filtering experiments at COSY performed by the PAX Collaboration were two. The first was to confirm the present understanding of the spin filtering processes

in storage rings, and the second was the commissioning of the experimental setup, which will be used for the experiments with the antiprotons.

The major part of my PhD work consisted in the development and commissioning of a new trigger board to be implemented in the Data Acquisition System (DAQ) of the experiment. The motivation for the project was the replacement of the existing old-fashioned trigger system based on NIM logic modules, with a modern system based on FPGA programmable chips. This, also in perspective of the more complex detection system that the Collaboration is planning to realize for the future experimental activity.

The trigger board was designed and realized by the electronic workshop of the University of Ferrara and INFN of Ferrara. My first task was to write the control-software of the board. After that I performed a series of development and commissioning tests which successfully demonstrated the full efficiency of the board and gave green light for the implementation of the board in the experimental setup.

# Riassunto

Gli antiprotoni polarizzati garantiscono l'accesso a numerose osservabili fisiche fondamentali. Ad esempio la distribuzione di *transversity*, la quale è l'ultima parte mancante per completare lo studio della struttura partonica dei nucleoni al *leading twist* nel modello partonico basato sulla QCD. La *transversity* è direttamente misurabile tramite produzione Drell-Yan nelle collisioni doppio-polarizzate antiprotone-protone. Questo ed altri aspetti accessibili tramite gli esperimenti di scattering  $\vec{p}\vec{\bar{p}}$ , hanno portato la Polarized Antiproton eXperiments (PAX) Collaboration a proporre ricerche in tal senso all'High Energy Storage Ring (HESR) della Facility for Antiproton and Ion Research (FAIR). Inoltre, la produzione di fasci intensi di antiprotoni polarizzati rimane un problema irrisolto ed è alla base delle ricerche svolte dalla collaborazione.

Al COSY (COoler SYnchrotron dell'Institut für KernPhysik –IKP– del Forschungs Zentrum Jülich) (FZJ) sono in corso intensi studi sulla possibilità di realizzare il progetto della PAX Collaboration. In questo contesto ho svolto il mio lavoro di tesi.

Al giorno d'oggi, l'unico metodo percorribile per polarizzare un fascio di antiprotoni è lo spin-filtering, il quale prevede di fare interagire ripetutamente il fascio con un bersaglio di idrogeno polarizzato per sfruttare la dipendenza dallo spin delle interazioni ( $p\bar{p}$ ). Poichè la sezione d'urto totale è diversa a seconda che lo spin delle particelle del fascio sia parallelo o antiparallelo rispetto alla polarizzazione del bersaglio, una direzione di spin viene estinta più velocemente dell'altra e quindi aumenta la polarizzazione del fascio circolante a scapito tuttavia dell'intensità del fascio che diminuisce nel tempo.

Durante il 2011 al COSY di Jülich è stato realizzato un esperimento di spin-filtering con due finalità: la prima era confermare le attuali conoscenze in merito al processo di spin-filtering all'interno di anelli di accumulazione,

mentre la seconda riguardava la messa in opera dell'apparato sperimentale che verrà impiegato per le attività future della collaborazione.

La maggior parte del mio lavoro di dottorato è consistita nello sviluppo di una nuova scheda di *trigger* che sarà implementata nel sistema di acquisizione dati (DAQ) degli esperimenti pianificati dalla collaborazione. Il progetto ha preso il via dalla necessità di sostituire il vecchio sistema di *trigger* basato su moduli logici NIM, con un moderno sistema basato su *chip* riprogrammabili FPGA. Tutto ciò anche in prospettiva di poter gestire in futuro un sistema di rivelazione molto più complesso che la PAX Collaboration ha in programma di costruire.

La scheda di *trigger* è stata disegnata e realizzata dall'officina elettronica dell'Università di Ferrara ed INFN di Ferrara. Il mio primo compito è stato quello di scrivere il programma di controllo della scheda. Dopodichè ho condotto una serie di test volti allo sviluppo della scheda i quali ne hanno provato la completa efficienza ed hanno quindi dato il via libera alla futura implementazione del modulo all'interno dell'apparato sperimentale.

# Introduction

This thesis has been performed in the frame of the **Polarized Antiproton eXperiments (PAX) Collaboration** [2], that has proposed recently an extensive physics program using a polarized antiproton-polarized proton collider at the **Facility for Antiproton and Ion Research (FAIR)**, at **Gesellschaft für SchwerIonenforschung (GSI, Centre for Heavy Ion Research)** in Darmstadt, Germany [1]. At the core of the PAX proposal there is the challenging project to polarize a stored antiprotons beam. In this frame, an intense work on the feasibility of this ambitious project is going on at **COSY (COoler SYnchrotron of the Institut für KernPhysik –IKP– of the Forschungs Zentrum Jülich) (FZJ)** where I have performed my thesis work. The COSY facility is a cooler synchrotron and storage ring for protons in the momentum range between  $600 \text{ MeV}/c$  and  $3700 \text{ MeV}/c$ . The systematic studies carried on at COSY on the polarization of a stored proton beam will allow to apply the same technique to antiprotons.

The advent of a stored beam of polarized antiprotons and the realization of a double-polarized high-luminosity antiproton-proton collider would enhance enormously the physics potential for QCD experiments. To quote few examples, such a collider would, e.g., give a unique access to the first direct measurement of the transversity distribution of the valence quarks in the proton, a test of the predicted opposite sign of the Sivers-function, related to the quark distribution inside a transversely polarized nucleon and a first measurement of the moduli and the relative phase of the time-like electric and magnetic form factors of the proton. See for reference the PAX proposal [2], and the first chapter of this thesis.

For more than two decades, physicists have tried to produce beams of polarized antiprotons, generally without success. Conventional methods like atomic beam sources (ABS), appropriate for the production of polarized protons and heavy ions cannot be applied, since antiprotons annihilate with

matter. Polarized antiprotons have been produced from the decay in flight of anti-hyperons at Fermilab. The intensities achieved with antiproton polarizations  $P > 0.35$  never exceeded  $1.5 \cdot 10^5 s^{-1}$  [9]. Scattering of antiprotons off a liquid hydrogen target could yield polarizations of  $P \approx 0.2$ , with beam intensities of up to  $2 \cdot 10^3 s^{-1}$  [10]. Unfortunately, both approaches do not allow efficient accumulation in a storage ring, which would greatly enhance the luminosity. Spin splitting using the Stern-Gerlach separation of the given magnetic substates in a stored antiproton beam was proposed already in 1985, but it has never been experimentally demonstrated (see [3]).

To obtain stored polarized antiproton beams, the only possibility is to polarize an initially unpolarized beam while it is circulating in the ring, (in-situ polarization buildup). Prompted by the PAX proposal, interest in the in-situ polarization of nucleons has been recently revived and the mechanism of the polarization discussed and understood in detail. See, for reference, the workshops at Daresbury [4], and at Bad Honnef [5]. In the case of a nucleon, that a fermion and has two spin states, the in-situ polarization would be achieved by either selectively discarding particles in one spin state ("*filtering*"), by multiple passage through a Polarized Internal hydrogen gas Target (PIT), or by selectively reversing the spin of particles in one spin state ("*flipping*"). In the latter case, nucleons in one spin state would be moved into the other state (by spin-flip), scattering on polarized electrons or positrons. The advantage of the spin flip method is that the precious stored beam is conserved by this process, while the filtering method is obviously very expensive in terms of polarized beam intensity. A high spin-flip cross-section would create an effective method to produce a polarized antiproton/proton stored beam by polarized positrons/electrons. As a consequence, this attractive method has received recently a great attention. Arenhovel [12] predicted that the spin-flip cross section in electron-proton scattering at low energy (a few eV) in the center-of-mass system) is very large because of the mutual attraction of the two oppositely charged particles. Walcher and co-workers adopted this idea for a proposal to polarize stored antiprotons with a co-moving beam of polarized positrons [13]. The proper low interaction energy would be achieved by making the two beam velocities almost the same. Even though the achievable positron beam intensities are quite low, the predicted spin-flip cross sections are so large that the scheme would still be feasible. However, a very recent dedicated experiment at COSY, in which the depolarization of a stored polarized

proton beam scattering from unpolarized electrons was measured, rules out the prospect of using spin flip to polarize a stored beam [15].

Thus, at this time, spin-filtering is the only known method that stands a reasonable chance of being successful in the production of a stored beam of polarized antiprotons. This method was suggested in 1968 by Csonka [16]. In his paper he proposed spin-selective attenuation of the particles circulating in a storage ring as a method to polarize the Intersecting Storage Ring (ISR) stored protons at CERN. Particles stored in the ring pass through a polarized target and a fraction of the beam is lost by nuclear scattering in the target. Since the strong interaction cross section is different for beam and target spins parallel ( $\uparrow\uparrow$ ) and anti-parallel ( $\uparrow\downarrow$ ), one spin direction of the circulating beam is depleted more than the other. As a result the circulating beam becomes increasingly polarized. This idea was tested in 1993 by the **FILTer EXperiment** (FILTEX) experiment [17], where stored protons of  $23\text{MeV}$  energy scattered on an internal gas target of the polarized hydrogen atoms. In ninety minutes, the intensity of the beam was 5% of the initial one and the polarization degree amounted to 2.4%. The FILTEX experiment is the first (and so far only) evidence that a stored nucleon beam can be polarized in situ. The recent COSY experiment [15] has demonstrated that, as suggested by Csonka, only the strong interaction will contribute to the spin filtering. However, to predict the final cross-section, and the rate of the polarization buildup, various effects must be taken into consideration. One is the interference of the Coulomb amplitude and the spin-dependent part of the hadronic amplitude. Three different groups came independently to the same conclusion, confirming the estimation of this effect done for the first time by H.O.Meyer, analysing the FILTEX results (see H.O.Meyer in [18][19], and ten years later [20] [21]). Concerning the kinematics of the nucleon-hydrogen atom interaction in the PIT, in principle three different scattering can contribute to the effect. They are the scattering at the target proton out of the acceptance angle, the scattering at the target proton within the acceptance angle and the scattering at the target electrons within the acceptance angle. Scattering at the target electrons out of the ring acceptance does not occur as the maximum scattering angle is always smaller than the machine acceptance due to the smallness of the mass ratio  $m_e/m_p$ . The evaluation of the contributions of the two scattering reactions, in which the nucleon remains in the beam, has been controversial. In his analysis of the FILTEX result, H.O.Meyer (i) observed that stored particles which scatter elastically in the PIT at angles within a storage

ring acceptance angle  $\theta_{acc}$  are retained in the beam and their polarization complements the nuclear polarization by spin-transfer, and (ii) argued that the QED spin-flip from polarized target electrons to scattered protons is crucial for the quantitative understanding of the FILTEX result [18][19] (here is worthwhile to mention that in the FILTEX target proton and electrons were both polarized). Ten years later Milstein and co-workers [20] showed that the relevant quantity to evaluate is the spin-flip cross section, which is different from, and much smaller than the spin-transfer cross section and is in fact negligible for the proton energy used in the FILTEX experiment. This conclusion has been immediately confirmed by [21].

To confirm the FILTEX results, and verify the theoretical interpretations outlined above, the PAX collaboration is performing a spin-filtering experiment at COSY. The scientific objectives of this experiment are twofold. A measurement of the polarization buildup at COSY yields values for the proton-proton spin-dependent total cross sections at different energies, thus allowing us to match these cross sections to the spin-filtering process involving machine related issues. Therefore, spin-filtering experiments at COSY would provide the necessary data to test and improve our present understanding of spin-filtering processes in storage rings. Secondly, understanding of the spin-filtering processes in storage rings would allow us to pave the way to produce stored polarized antiproton beams.

In this frame, I have had the responsibility to develop and test a new trigger system, connected with the data acquisition of the polarimetry system of the experiment. To this aim, I spent most part of the research time for my PhD in Jülich supported by a dedicated grant of the Zentralinstitut für Elektronik (ZEL – Central Institute of Electronic, FZJ). In this thesis, I present the first results of the spin-filtering experiment on the polarization buildup of the stored protons at COSY. The thesis is organized as follow. In the first chapter a short introduction about the PAX physics case is given, in the second chapter few methods for polarizing antiprotons and more in detail the spin-filtering method are discussed, in the third chapter a description of the COSY experimental apparatus is presented and the last spin-filtering measurements at COSY are reported, in the fourth chapter the new trigger system is described along with the performed commissioning work and the dedicated control software. Finally conclusions of my work are given.

# Chapter 1

## Physics motivations

### 1.1 Hadron structure at the partonic level

Unique access to a number of new fundamental physics observables will be provided by polarized antiprotons. The PAX Collaboration [2] has proposed to study polarized proton-antiproton ( $p \bar{p}$ ) interactions at the High Energy Storage Ring (HESR), in the framework of the FAIR. Some of the highlights physics potential of a beam of polarized antiprotons will be outlined in the next sections.

#### 1.1.1 The spin structure of the proton

At leading twist level the quark structure of hadrons is described by three distribution functions: the unpolarized quark distribution  $q(x, Q^2)$ , the helicity distribution  $\Delta q(x, Q^2)$  and the *transversity* distribution  $\Delta_T q(x, Q^2)$  (also denoted as  $h_1^q(x, Q^2)$  or  $\delta(x, Q^2)$ ). The quark longitudinal polarization inside a longitudinally polarized proton is described by  $\Delta q$ , while the quark transverse polarization inside a transversely polarized proton at infinite momentum [22] is described by the *transversity*;  $\Delta q$  and  $\Delta_T q$  are independent quantities which might be equal only in the non-relativistic, small  $Q^2$  limit. Furthermore the gluon polarization and the quark transverse polarization do not mix (since gluons carry only longitudinal spin), and thus the  $\Delta q$  QCD evolution and the  $\Delta_T q$  QCD evolution are quite different. Until all three leading-twist structure functions have been measured, it is not possible to claim to understand the spin structure of the nucleons. Very

little is experimentally known about the nucleon transversity distribution, while the unpolarized distributions are well known and more and more informations are becoming available on  $\Delta q$ . Only a few models exist for  $\Delta_T q$  from the theoretical side; an upper bound on its magnitude has been derived: this bound holds in the naive parton model and, if true in QCD at some scale, it is preserved by QCD evolution. Since  $\Delta_T q$  is a chiral-odd function and consequently decouples from inclusive deep-inelastic scattering,  $\Delta_T q$  has only very recently started to be experimentally accessible, despite its fundamental importance.  $\Delta_T q$  cannot occur alone, but has to be coupled to a second chiral-odd quantity since electroweak and strong interactions conserve chirality. In polarized Drell-Yan (DY) processes it is possible to couple a second chiral-odd quantity, indeed the product of two transversity distributions is measured, or it is possible in semi-inclusive Deep Inelastic Scattering (SIDIS), where  $\Delta_T q$  is coupled to a fragmentation function (the so-called Collins function [23]). Both the HERMES [24] and COMPASS<sup>1</sup> [25] experiments have gathered data on spin asymmetries in SIDIS processes, bringing informations on the convolution of the transversity and the Collins function. Anselmino et al. provided the first extraction of the transversity distribution [27] based on the spin asymmetries in the SIDIS processes and on the data from Belle which provided the first direct measurement of the Collins function by the Belle collaboration from  $e^+ e^- \rightarrow h_1 h_2 X$  processes [26]. The result of this first extraction is puzzling as the value of the transversity distribution is well below all the present theoretical estimations, a discrepancy which may originate from uncertainties in the extraction procedure as well as from the necessity of better theoretical models. To better understand the problem a direct measurement of transversity is highly desirable.

### 1.1.2 Transversity and polarized antiprotons

The measurement of the double transverse spin asymmetries  $A_{TT}$  in Drell-Yan processes with both transversely polarized beam and target is the most direct way to obtain informations on transversity:

$$A_{TT} = \frac{d\sigma^{\uparrow\uparrow} - d\sigma^{\uparrow\downarrow}}{d\sigma^{\uparrow\uparrow} + d\sigma^{\uparrow\downarrow}} = a_{TT} \frac{\sum_q e_q^2 \Delta_T q(x_1, M^2) \Delta_T q(x_2, M^2)}{\sum_q e_q^2 q(x_1, M^2) q(x_2, M^2)} \quad (1.1)$$

---

<sup>1</sup>Common Muon and Proton Apparatus for Structure and Spectroscopy.

where  $q = u, d$ , where the lepton pair invariant mass is indicated by  $M$ , the fractional longitudinal momenta of the colliding hadrons are  $x_{1,2}$  and  $a_{TT}$  is the double spin asymmetry of the QED elementary process  $q \bar{q} \rightarrow l^+ l^-$ .

Measurements of  $A_{TT}$  are planned at RHIC<sup>2</sup>, in Drell-Yan processes with transversely polarized protons; the product of two transversity distributions (one for a quark and one for an antiquark) both in a proton is measured in this case. The expected measurements are at  $\tau = x_1 x_2 = M^2/s = 10^{-3}$  for RICH energies, which mainly lead to the exploration of the sea quark proton content, where the polarization is likely to be tiny [28].

The situation with the PAX measurement of the double transverse spin asymmetry  $A_{TT}$  in Drell-Yan processes with polarized antiprotons and protons is totally different: the PAX experiment will explore ranges which are ideal for the measurement of large values of  $A_{TT}$ , that is ranges of  $s \approx 30 \div 200 \text{ GeV}^2$  and  $M^2 \approx 4 \div 100 \text{ GeV}^2$  combining the fixed target and the collider operational modes. There are some unique features which strongly suggest to pursue the study of  $\Delta_{Tq}$  in the  $p \bar{p}$  channel.

Both the quark (from the proton) and the antiquark (from the antiproton) contributions are large in  $p \bar{p}$  processes. For typical PAX kinematics in the fixed target mode ( $s = 30 \text{ GeV}^2$ ) only quarks and antiquarks with large  $x$  contribute ( $\tau = x_1 x_2 = M^2/s \approx 0.2 \div 0.3$ ), that means valence quarks for which  $\Delta_{Tq}$  is expected to be large and not suppressed by the QCD evolution. The ratio  $A_{TT}/a_{TT}$  is expected to be as large as 30%. The  $(x_1, x_2)$  kinematical region covered by the PAX measurements, both in the fixed target and collider mode, are described in fig.1.1a. The expected values of the asymmetry  $A_{TT}$  as a function of Feynman  $x_f = x_1 - x_2$ , for  $Q^2 = 16 \text{ GeV}^2$  and different values of  $s$  are shown in fig.1.1b. For the transversity distribution  $\Delta_{Tq}$  this experiment plays the same role as polarized inclusive DIS played for the helicity distribution  $\Delta q(x, Q^2)$ , with a kinematical  $(x, Q^2)$  coverage similar to that of the HERMES experiment.

---

<sup>2</sup>Relativistic Heavy Ion Collider.

<sup>3</sup> $s$  is the center of mass energy.

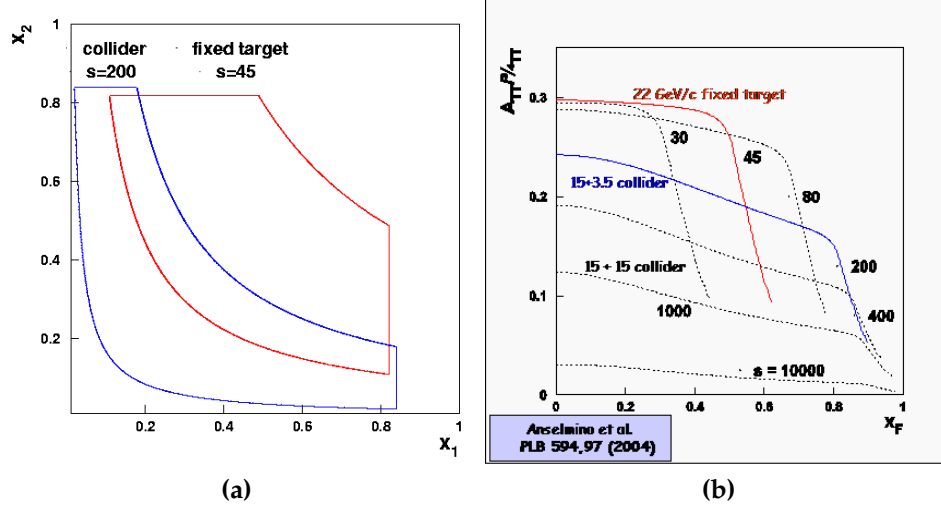


**Figure 1.1:** (a). The kinematic region covered by the  $\Delta_T q$  measurements at PAX in phase II. In the asymmetric collider scenario antiprotons of  $15 \text{ GeV}/c$  impinge on protons of  $3.5 \text{ GeV}/c$  at c.m. energies of  $s \sim 200 \text{ GeV}^2$  and  $Q^2 > 4 \text{ GeV}^2$ . (b). The expected asymmetry as a function of Feynman  $x_F$  for different values of  $s$  and  $Q^2 = 16 \text{ GeV}^2$

## 1.2 Magnetic and electric form factors

### 1.2.1 The form factors of the protons

The electromagnetic structure of the nucleon is traditionally described in terms of form factors (FFs) which are related to the current and magnetic distributions. In a  $P$  and  $T$  invariant theory, a particle of spin  $s$  has  $2s + 1$  form factors: two different FFs describe any nucleon (proton as well as neutron). FFs are experimentally related to the differential cross section and polarization observables and calculable by the nucleon models, which means FFs are measurable quantities. Elastic electron hadron scattering is considered to be the most direct way to access FFs, which contains the information on the ground state of the hadron. The interaction is assumed to occur through one photon exchange. In this particular case FFs are real functions of a single variable, the four momentum of the virtual photon  $t = -Q^2 < 0$ . Annihilation processes as  $e^+ + e^- \leftrightarrow N + \bar{N}$ , also give access to the nucleon FFs, but in another kinematical region where FFs are complex functions of the momentum transfer squared  $q = -Q^2 > 0$  (the so-called

time-like –TL– region).

There is a great theoretical interest in the nucleon time-like form factors. Although the space-like form factors of a stable hadron are real, the time-like form factors have a phase structure reflecting the final state interactions (FSI) of the outgoing hadrons. Kaidalov et al. argue that the same FSI effects are responsible for the enhancement of  $G_M(q^2)$  in the time-like region [31]; their evaluation of the enhancement based on the variation of Sudakov effects from the space-like to the time-like region is consistent with general requirements from analyticity that FSI effects vanish at large  $q^2$  in the pQCD asymptotics (a discussion by Brodsky et al. can be found in [32]). The hybrid pQCD-DR description developed by Hammer, Meissner and Drechsel [33] and vector-dominance based models (VDM) [34] share the same property of vanishing FSI at large  $q^2$ .

Two serious issues rise from recent experiments:

- Fermilab E835 measurements of  $|G_M(q^2)|$  [35] have shown that  $|G_M(q^2)|$  in the time-like region is twice as large as in the space-like region;
- studies of  $e^- p$  polarization transfer in  $e^- p \rightarrow e p^-$  scattering at Jefferson Laboratory [36] have shown that the ratio of the Sachs form factors  $G_E(q^2)/G_M(q^2)$  is monotonically decreasing with increasing  $Q^2 = -q^2$ , in strong contradiction with the  $G_E/G_M$  scaling deduced in the traditional Rosenbluth separation method, which may in fact not be reliable in the space-like region. Additional direct measurements of the form factors are pointed out by both these measurements.

### 1.2.2 Measurements with antiprotons

As stressed by Brodsky et al. [32] the new Jefferson Laboratory result make it fundamental to carefully identify and separate the time-like  $G_E$  and  $G_M$  form factors by measuring the center-of-mass angular distribution and the polarization of the proton in  $e^- e^+ \rightarrow p^- \bar{p}$  or the transverse single spin asymmetry SSA  $A_y = P_y$  in polarized  $p^\uparrow \bar{p} \rightarrow e^- e^+$  reactions. As noted by Dubnickova et al. [37], the non-zero phase difference between  $G_E$  and  $G_M$  entails the normal polarization  $P_y$  of the final state (anti)baryons in  $e^- e^+ \rightarrow p^- \bar{p}$  or the transverse SSA  $A_y = P_y$  in annihilation  $p^\uparrow \bar{p} \rightarrow e^- e^+$

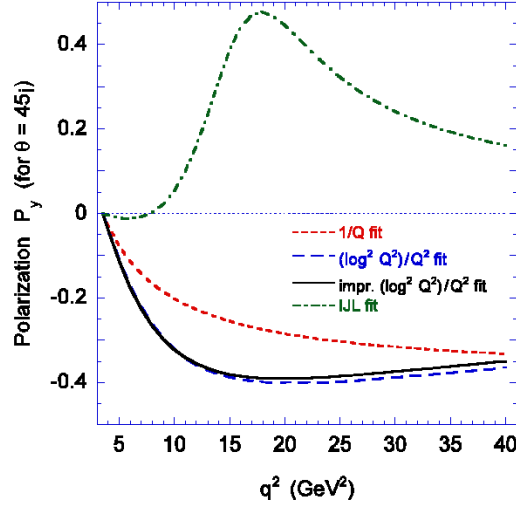


**Figure 1.2:** Predicted single-spin asymmetry  $A_y = P_y$  for  $\theta = 45^\circ$  in the time-like region for selected form factor fits [32].

on transversely polarized protons:

$$A_y = \frac{\sin 2\theta \text{Im} G_E^* G_M}{\left[ \frac{(1+\cos^2 \theta)|G_M|^2 + \sin^2 \theta |G_E|^2}{\tau} \right] \sqrt{\tau}} \quad (1.2)$$

where  $\tau = q^2/4m_p^2 > 1$  and  $\theta$  is the scattering angle.

The knowledge of the phase difference between the  $G_E$  and  $G_M$  may strongly constrain the models for the form factors. The predicted single-spin asymmetry is substantial and has a distinct  $q^2$  dependence which strongly discriminates between the analytic forms which fit the proton  $G_E/G_M$  data in the space-like region (see fig.1.2). Such measurements have never been made, despite the fundamental implications of the phase for the understanding of the connection between space-like and time-like form factors. From the SSA data with transversely polarized proton target the PAX experiment would measure the relative phase  $\Phi_{EM}$  of the form factors. From the angular distribution in an unpolarized measurement for  $p\bar{p} \rightarrow e^+e^-$  the moduli of  $G_E$  and  $G_M$  can be deduced, as it can be carried out independently at PANDA<sup>4</sup> as well as PAX in different cinemactical regions.

<sup>4</sup>antiProton ANnihilation at DArmstadt.

Independent  $G_E - G_M$  separation and check of the Rosenbluth separation in the time like region (which has not been carried out so far) will be provided by the additional measurement of the transverse double spin asymmetry in  $p^\uparrow \bar{p} \rightarrow e^- e^+$ . The separation of magnetic and electric form factors in the time like region allows for the most stringent tests of the asymptotic regime and QCD predictions, as pointed out by Tomasi-Gustafsson and Rekaló [38]. According to Dubnicka et al.:

$$A_{yy} = \frac{\sin^2(|G_M|^2 - |G_E|^2/\tau)}{\left[ \frac{(1+\cos^2 \theta)|G_M|^2 + \sin^2 \theta |G_E|^2}{\tau} \right]} \quad (1.3)$$

Furthermore the polarization of the proton target can readily be changed to the longitudinal direction in the fixed target mode, and in-plane longitudinal-transverse double spin asymmetry would allow to measure

$$A_{xz} = \frac{\sin 2\theta \operatorname{Re} G_E^* G_M}{\left[ \frac{(1+\cos^2 \theta)|G_M|^2 + \sin^2 \theta |G_E|^2}{\tau} \right]} \quad (1.4)$$

which would resolve the remaining  $\Phi_{EM}$  or  $(\pi - \Phi_{EM})$  ambiguity from the SSA data. This will put tight constraints on current models for the form factors.

### 1.3 Spectroscopy of hadrons

The annihilation of antiprotons and protons produces a multitude of final states with two more mesons. They carry the potential of containing new states (exotics) like glue balls of hybrid states composed of quarks and gluons. However, the analysis of the final state is hampered by the need to perform a partial wave analysis which is frequently not unique. The exploitation of spin degrees of freedom for both the projectile antinucleon and the target nucleon should at least halve the contributing amplitudes and increase the significance of the search for the exotics considerably. Furthermore the study of known states would be more selective making an identification clearer and offer an additional parameter in the decay dynamics.

## 1.4 Antinucleon-nucleon scattering and reactions

The same argument holds for antinucleon-nucleon scattering, these cross section have been measured from close to threshold up to many  $GeV$ . The isospin dependence of the antinucleon-nucleon interaction at low energies is a particularly interesting aspect. As well known, the nucleon-nucleon and antinucleon-nucleon potentials are connected in the meson exchange description by the G-parity symmetry. However, whereas it appears that the long range part of the potential is in this way reasonably well described by pion exchange, there is no sensitivity to the short range part attributed to the vector meson exchange, since the annihilation dominates for radii shorter than about  $0.8 fm$  [39]. The different spin orientation of the entrance channel close to threshold, where s- and p-wave scattering dominate, will provide sensitivity to vector mesons, i.e. to the short range of the real part of the antinucleon-nucleon interaction. For the annihilation dynamics the question whether the quark reorientation or the gluonic quark fusion-creation mechanism (OZI rule violation) prevails is not satisfactorily answered. New data with spin degrees of freedom would provide very significant constraints.

### 1.4.1 Double polarized hard antiproton-proton scattering

Very large double transverse asymmetries have been observed in  $p^\uparrow p^\uparrow$  scattering at ZGS [40] [41]. These constitutes the largest asymmetries ever detected in hadron physics and a complete theoretical explanation is still missing.

The HESR data with polarized antiprotons at PAX will complement the AGS-ZGS data in a comparable energy range. To explain the asymmetries, different theoretical attempt exist and all of them would benefit from additional data in the  $\bar{p}p$  sector. In 1974 Nielsen et al. argued [42] that within the independent scattering models, the change from the dominance  $1 \times 1$  parton-parton scattering to the  $2 \times 2$  and  $3 \times 3$  scattering leads in a natural way to the oscillatory (and rising with  $t$ ) behaviour of polarization effects. Within this approach Neat et al. reproduce the gross features of the ZGS data [43]. Within the QCD motivated approach, initiated in [43]. The helicity properties of different hard scattering mechanisms have been studied by Ramsey and Sivers [45]. These authors tried to extract the normalization of the Landshoff amplitude from the combined analysis of  $pp$

and  $\bar{p}p$  elastic scattering and argued that it must be small to induce the oscillations or contribute substantially to the double spin asymmetry  $A_{TT}$ . This leaves open the origin of oscillations in  $R_1$  but leads to the conclusion that the double spin asymmetry  $A_{TT}$  in  $\bar{p}^\uparrow p^\uparrow$  at PAX and  $p^\uparrow p^\uparrow$  as observed at AGS-ZGS must be of comparable magnitude. The comparison of  $A_{TT}$  in the two reactions will also help constrain the Landshoff amplitude. Brodsky and Teramond make a point that opening of the  $|uud\bar{u}udcc\rangle$  channel at the open charm threshold would give rise to a broad structure in the  $J = L = S = 1$  proton-proton partial wave [46]. Such a threshold structure would have a negative parity and affect  $p^\uparrow p^\uparrow$  scattering for parallel spins normal to the scattering plane. The threshold structure also imitates the "oscillatory" energy dependence at fixed angle and the model is able to reproduce the gross features of the  $s$  and  $t$  dependence of  $A_{NN}$ . Arguably in the  $\bar{p}p$  channel the charm threshold is at much lower energy and the charm cross section will be much larger, so the Brodsky-Teramond mechanism would predict  $A_{NN}$  quite distinct from that in  $pp$  channel. Still, around the second charm threshold  $\bar{p}p \rightarrow \bar{p}p c \bar{c}$  for  $\bar{p}p$  may repeat the behaviour exhibited in  $pp$  scattering.



## Chapter 2

# Production of polarized antiprotons

As discussed in chapter 1, polarized antiprotons will provide access to a wealth of single and double spin observables. Despite the interest, up to now, an intense beam of polarized antiprotons has not been realized. Different suggestions, made at the workshop in Bodega Bay (1985) [3] have not yet been tested or do not allow for efficient accumulation in a storage ring. After more than twenty years, the spin filtering is the only tested method to produce a polarized proton beam that may be capable to hold also for polarized antiprotons. See for reference the FILTEX experiment at Heidelberg (1992) [17] and the PAX proposal [2]. The challenging project to polarize a stored antiprotons beam with the filtering method is at the core of the PAX proposal [2].

Although the experimental evidence of the possibility to polarize proton stored beams dates more than fifteen years, a full understanding of the polarization mechanism in filtering processes has only been achieved quite recently. Prompted by the PAX proposal, a complete theoretical description of the interplay of the accelerator and the internal target is now available [18]–[21]. Based on this theoretical considerations, polarization build up and related cross sections can be predicted and compared with experimental measurements.

In this chapter, after a short excursus over the theoretical implementation of the polarization build up (§2.1), the theoretical parametrization of the polarization cross sections and the polarization build up in the filtering processes are presented and compared with the FILTEX existing data

(§2.2.1). The expected polarization build up and polarization cross section for COSY are presented in §2.2.2. The experimental data are consistent with the theoretical predictions, confirming the current understanding of the filtering mechanism. To conclude this chapter, estimations for the protons-antiprotons spin dependent cross sections are given in §2.2.3. Based on these estimates, it is clear that a dedicated storage ring would be able to provide a high polarization degree for antiproton beam.

## 2.1 How to polarize antiprotons

When intense antiprotons beams became a new tool in nuclear and particle physics, the demand of polarizing them came as a straightforward consequence. Although there has always been no shortage of rough ideas on how to accomplish polarized antiprotons beams, polarizing antiprotons is a challenge that lasts for more than twenty years among physicists. Methods which work for the production of polarized protons and heavy ions, like **A**tom**B**eam **S**ources (ABS), have proved to be not useful since antiprotons annihilate with matter. At the workshop of Bodega Bay (CA, USA) in 1985 [3]. all the available ideas for methods to polarize antiprotons were discussed and can be basically summarized in the following list [6]:

- (i) polarized antiprotons from the decay in flight of antihyperons;
- (ii) spin filtering of antiprotons by a polarized hydrogen target in a storage ring;
- (iii) stochastic techniques like "Stochastic Cooling";
- (iv) dynamic nuclear polarization (DNP) in flight using polarized electrons and microwave radiation;
- (v) spontaneous spin-flip synchrotron radiation;
- (vi) spin-flip synchrotron radiation induced by X-ray laser;
- (vii) polarization by scattering;
- (viii) repeated Stern-Gerlach deflection;

- (ix) polarized antiprotons via the formation of antihydrogen and application of the ABS method;
- (x) polarizing during storage in a Penning trap;
- (xi) polarizing by channeling;
- (xii) polarizing through interaction with polarized X-ray from a diamond crystal.

Although the theoretical understanding has much improved since then, not many of the listed ideas have been scrutinized or even put into operation. Up to now, polarized antiprotons have been produced at Fermilab from the decay in flight of  $\bar{\Lambda}$  hyperons with a polarization of  $P > 35\%$  and intensities that never exceeded  $1.5 \cdot 10^5 s^{-1}$  [9], and from the scattering of antiprotons off a liquid hydrogen target, which allows to achieve polarizations of  $P \approx 0.2$  with beam intensities of  $2 \cdot 10^3 s^{-1}$  [10]; however none of these methods provide enough intensity in order to allow efficient accumulation in a storage ring which would improve the luminosity. Below follows a short overview of the methods listed above.

**Atomic Beam Source** Atomic beam sources are largely employed to provide polarized proton beams [11]. For example starting from molecular hydrogen one can form a beam and then manipulate it in order to polarize it and then ionize it to finally get a polarized proton beam. Many polarized gas targets are available at present day (an overview is available in [7]). In principle, from the ABS technique point of view, dealing with thermic antihydrogen beam should be the same as it is for hydrogen beam. Nowadays however the maximum number of antihydrogen atoms that is possible to produce is many orders of magnitude too low in order to allow to feed an atomic beam source system and then generate a polarized antiprotons beam.

**Dynamic Nuclear Polarization in flight** The dynamic nuclear polarization in flight is a way to polarize proton transferring polarization from close electrons [3]. In this case, in a region provided with a high longitudinal magnetic field, polarized electrons should interact with injected unpolarized antiprotons which move at the same velocity as the electrons. Nevertheless even with high electrons density ( $10^{10} cm^{-3}$ ) the

polarization transfer rate is very low ( $10^{-5} s^{-1}$ ). Is therefore impossible to consider this method a useful tool to polarize antiprotons.

**Stern-Gerlach separation** The Stern-Gerlach separation technique entails the use of Stern-Gerlach forces which are intended to split a group of antiprotons into two polarized antiprotons subgroups [3]. There are two basically different ways to accomplish this task: one leads to a spacial separation and involves the transverse Stern-Gerlach forces, while the other implies the use of the longitudinal Stern-Gerlach forces and results in different beam energies. Up to now neither feasibility studies nor experimental tests have been performed about these methods; moreover the experimental test would require a large effort to be carried out, so this idea is into a stall (for a more detailed summary about producing stored polarized antiprotons beam see [4]).

**Antiprotons from antihyperon decay** Polarized antiprotons beam have been produced at Fermilab. The process involves the decay of polarized antihyperons coming from one side of the collisions between a fixed target and  $400 GeV$  protons. The generated antiprotons are succesively focused in a  $200 GeV$  beam with achieved polarization up to 50%. Such a beam has been realized at Fermilab, as remarked above [9]. It is however impossible to utilize the polarized antiprotons obtained in this way because of the low intensity and the large phase space of the beam produced.

**Stochastic techniques** As suggested by the name, the stochastic technique is similar to the stochastic cooling. The stochastic cooling is a method to cool a beam measuring the position of its particles in one point of the accelerator and correcting the position of the particles in another point of the accelerator (kicker). The stochastic technique to polarize antiprotons is based on the idea of a dedicated detector capable of identify the polarization of the particle. This detector should then send a signal to the kicker which will kick out the particles that are in a precise polarization state. The main realization problem arises from the fact that the electric signals generated from the magnetic moment of the protons are very small when compared to the electric signals generated by the protons charge.

**Polarization build up by synchrotron radiation** Magnetic fields are employed in order to force charged particles to close orbits in synchrotrons. In the bending region synchrotron radiation is emitted, part of which comes from the spin-flip processes: for an electron cyclotron with a bending radius  $\rho \approx 13m$  and  $\gamma < 10^4$  the ratio is  $P_{spin-flip}/P_{non-flip} \approx 10^{-11}$ , that means a rather long polarization build up time for the electrons. Even taking into account the Large Hadron Collider (LHC) features and trying to make rough estimations about protons polarization build up time, the interval time is in the order of  $10^{16} years$  [60].

**Channeling through a bent crystal** Bent crystals are widely used to channel many types of particles. The main idea is that such crystals may polarize antiprotons through repeated interactions with the nuclei of a curved channel in their lattice. The channeled beam could gain polarization, provided that the single scattering process has its own analyzing power. From the theory [52] comes the result that with an analyzing power  $A_y = 0.5\%$  one could get beam polarization of more than 50% after the extraction of the primary beam from a bent crystal. This implies that it might be worth to test this method of polarization making.

Concluding, up to now experimental evidences have been collected only about the spin filtering method by the FILTEX Collaboration. In 1992 at the Test Storage Ring of Heidelberg (TSR, Germany) an experiment showed that an initially unpolarized proton beam can be polarized by spin dependent interaction with a polarized hydrogen gas target, this should also work for antiprotons.

## 2.2 Spin filtering method

One of the first ways proposed to polarize nucleons was via the interaction with polarized targets. For example in 1966 it was shown by Shapiro [53] that polarized neutrons could be produced with the method of the spin selective attenuation in a solid polarized proton target because of the strong spin dependence in the  $(n, p)$  cross section. This method today is known as "*spin filtering*".

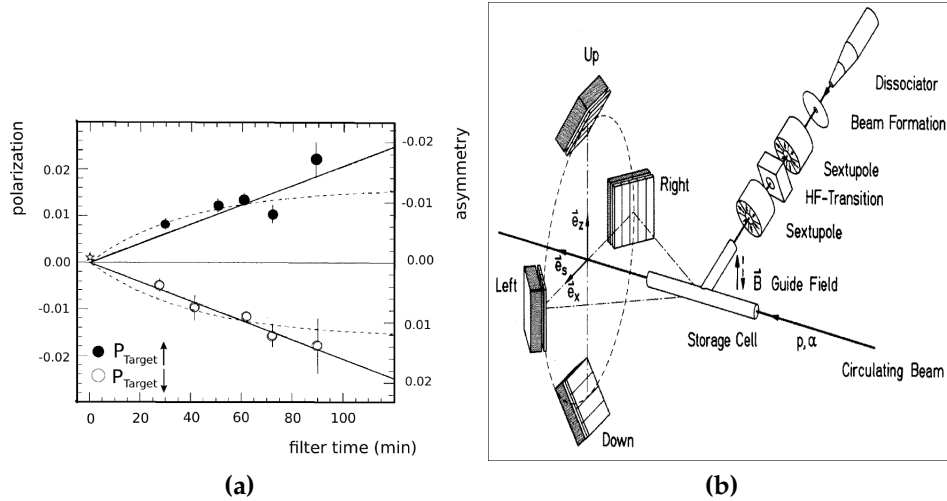


**Figure 2.1:** (a). Asymmetry (right scale) and polarization (left scale) measured after filtering the beam in the TSR for different times  $t$ . The solid lines are based on an assumed rate of polarization build-up of  $1.24 \times 10^{-2} h^{-1}$ , which corresponds to  $\tau_1 = 80 h$ . The dashed lines are based on the expected build-up rate ( $\tau_1 = 42 h$ ) and assumed polarization lifetime of  $\tau_p = 81 min$  [17]. (b). FILTEX experimental setup.

One of the first spin filtering experimental demonstrations was carried out employing an underground nuclear explosion [54] and a solid polarized protons target as source of polarized neutrons; the arrangement of the experiment was in a tower above the test site. Later on the explosive sources have been replaced by the introduction of intense polarized deuteron beams as source of polarized neutrons available in a broad energy range (nowadays polarized neutrons are still produced by means of spin filtering of thermal neutrons by a high pressure polarized  $^3He$  gas target which provides high transmission and polarization [55]).

In 1968 Csonka [16] proposed to try spin filtering on a polarized hydrogen target with  $30 GeV$  stored protons in the ISR at CERN, but at that time polarized ion sources followed by acceleration were already employed to produce polarized beams of stable ions, hence the spin filtering was never tested at such high energies.

In 1982 Kilian and Möhl [58] proposed to perform spin filtering of antiprotons in the Low-Energy Antiproton cooler Ring (LEAR) and in 1984 Povh, Steffens and Walcher improved the theoretical description providing moreover a realistic proposal for LEAR including feasibility studies at the

TSR of Heidelberg to be performed with protons [8].

The build-up of polarization by means of spin filtering was tested for the first time with an initially unpolarized proton beam of kinetic energy  $T = 23 \text{ MeV}$  at the Test Storage Ring (TSR) at Heidelberg [17]. Using multiturn stacking injection while reducing the phase space by electron cooling allowed to store a beam of up to  $1 \text{ mA}$  in the  $55.4 \text{ m}$  long storage ring. The circulating beam passed through a transversely nuclear polarized hydrogen gas target of an areal density of  $(5.3 \pm 0.3) \cdot 10^{13} \text{ H/cm}^2$ , provided by atoms from an atomic beam source, which were injected into a  $250 \text{ mm}$  long aluminum storage cell tube, cooled to about  $100 \text{ K}$ . Thereby, the target density compared to room temperature was increased by about a factor  $\sqrt{3}$ . The target atoms were in a single spin state, i.e., protons and electrons were both polarized. The magnitude of the nuclear target polarization was determined to be  $Q = 0.795 \pm 0.024$  using  $p\text{-}\alpha$  scattering [48],[49]. The FILTEX results are presented in fig.2.1a. It is observed that with positive target polarization the resulting beam polarization was positive, whereas for a negatively polarized target the beam became negatively polarized.

### 2.2.1 Filtering polarization cross section

The beam polarization  $P$  is defined by the relative occupation number of protons (antiprotons) with spins parallel and antiparallel to the quantization axis

$$P = \frac{N_{\uparrow} - N_{\downarrow}}{N_{\uparrow} + N_{\downarrow}}, \quad (2.1)$$

where  $N_{\uparrow,\downarrow}$  are the two possible spin-states and  $N_{\uparrow} + N_{\downarrow}$  denotes the total number of particles in the beam. Since in general the total hadronic cross section is different for parallel ( $\uparrow \uparrow$ ) and antiparallel ( $\uparrow \downarrow$ ) orientation of the beam particle spins relative to the direction of the target polarization, one spin direction is depleted faster than the other, so that the circulating beam becomes increasingly polarized, while the intensity decreases with time. This principle can be deduced from the total hadronic cross section [50], [51]

$$\sigma_{tot} = \sigma_0 + \sigma_1(\vec{P} \cdot \vec{Q}) + \sigma_2(\vec{P} \cdot \hat{k})(\vec{Q} \cdot \hat{k}), \quad (2.2)$$

where  $\vec{P}$  and  $\vec{Q}$  are the polarization vectors of the beam particle and the target particle,  $\sigma_0$  is the spin-independent hadronic cross section and  $\sigma_1$  and  $\sigma_2$  are the spin-dependent cross sections, describing the effect of the

relative orientation of  $\vec{P}$ ,  $\vec{Q}$  and the beam direction, given by the unit vector  $\hat{k}$ . Assuming  $|\vec{P}| = |\vec{Q}| = 1$  the cross sections for the transverse and the longitudinal case are

$$\sigma_{tot\pm}^{\perp} = \sigma_0 \pm \sigma_1 \quad \text{and} \quad (2.3)$$

$$\sigma_{tot\pm}^{\parallel} = \sigma_0 \pm (\sigma_1 + \sigma_2). \quad (2.4)$$

Consequently, the intensity of spin-up and spin-down particles each decreases exponentially but with different time constants. This leads to a polarization build-up with time  $t$ , which can be expressed in the absence of depolarization as

$$P(t) = \tanh(t/\tau_1). \quad (2.5)$$

The spin-dependent cross sections  $\sigma_1$  and  $\sigma_2$  can be extracted from the time constants for transverse ( $\perp$ ) or longitudinal ( $\parallel$ ) filtering, which are given by

$$\tau_1^{\perp} = \frac{1}{\tilde{\sigma}_1 Q d_t f} \quad \text{and} \quad (2.6)$$

$$\tau_1^{\parallel} = \frac{1}{(\tilde{\sigma}_1 + \tilde{\sigma}_2) Q d_t f}, \quad (2.7)$$

respectively. Here,  $d_t$  is the target areal density in  $atoms/cm^2$  and  $f$  is the revolution frequency of the particles in the ring. The polarizing cross sections  $\tilde{\sigma}_1$  and  $\tilde{\sigma}_2$  are closely related to the spin-dependent total cross sections  $\sigma_1$  and  $\sigma_2$ , where the difference arises because protons that scatter at a sufficiently small angle remain in the ring ( $\tilde{\sigma} = \sigma(\Theta > \Theta_{acc})$ ). This is the case if the scattering angle  $\Theta$  is smaller than the acceptance angle  $\Theta_{acc}$  of the machine. It is clearly demonstrated that with this model the polarization build-up rate and the related polarization cross section are strongly dependent on the accelerator parameters such as the diameter, the acceptance and the kinetic energy. In order to predict the polarization build-up rate, the relevant parameters of the machine which contribute to the spin-dependent cross section have to be well known. The polarization build-up depends on the target polarization  $Q$ , the target density  $d_t$ , the revolution frequency  $f$ , the acceptance angle at the target position  $\Theta_{acc}$ , and the polarizing cross section  $\tilde{\sigma}_1$ .

This model has been verified by the FILTEX results. In fact a polarization build-up rate of

$$\frac{dP}{dt} \approx \frac{1}{\tau_1} = 0.0129 \pm 0.0006 \quad \text{per hour} \quad (2.8)$$

has been observed. This corresponds to a polarizing cross section of  $\sigma_{pol} = (73 \pm 6 \text{ mb})$ . It is relevant to observe the theoretical prevision of the polarization cross section  $\sigma_1$  plotted versus the kinetic energy shown in fig.2.2, where the FILTEX measured cross section is comparable with the theoretical calculations.

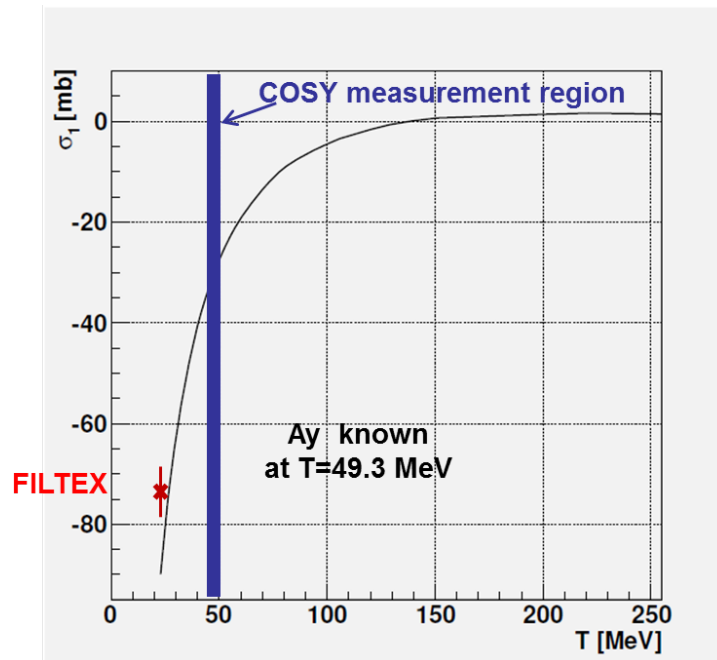


**Figure 2.2:** The polarizing cross section  $\sigma_1$  plotted versus the kinetic energy. Indicated is the TSR measurement of FILTEX (red) and the working energy area for spin-filtering at COSY (blue strip).

### 2.2.2 Estimation of the polarization build-up for COSY

The COSY accelerator has a circumference of 183.4 *m* and will be operated at an energy of  $T = 49.3 \text{ MeV}$ . The used input parameters are

$$\begin{aligned} Q &= 0.8 \\ d_t &= 4.35 \cdot 10^{13} \text{ atoms/cm}^2 \\ f &= 510032 \text{ Hz}(T = 49.3 \text{ MeV}) \\ \Theta_{acc} &= 6.13 \text{ mrad} \end{aligned} \tag{2.9}$$

In order to calculate the rate of polarization build-up, the double-spin asymmetries  $A_{00nn}$  ( $A_{yy}$ ) and  $A_{00ss}$  ( $A_{xx}$ ), the polarization transfer observables, and depolarization spin observables, which contribute to the polarizing cross section, were taken from the SAID database at  $T = 50 \text{ MeV}$  [56]. Consequently, with the given boundary conditions at COSY a polarization build-up rate of

$$\frac{dP}{dt} \approx 0.0019 / h \tag{2.10}$$

is expected.

### 2.2.3 Antiprotons: theoretical cross section predictions

It is interesting to observe that, applying the same modeling of the section §2.2.2 to filtering antiprotons, a dedicated antiproton storage ring could reach an important degree of polarization. The accelerators utilized for protons filtering experiments up to now have not been optimized for this aim.

At present, is not possible to give reliable predictions for the  $p \bar{p}$  cross section below 1 *GeV* and different phenomenological models are usually used for numerical estimations. As a result, the cross sections obtained are model-dependent. All models are based on fitting of experimental data for scattering of unpolarized particles. These models give similar predictions for spin-independent part of the scattering cross sections, but predictions for spin-dependent parts may differ drastically.

In [29] the spin-dependent part of the cross section of  $p \bar{p}$  interaction was calculated (fig.2.3) altogether with the corresponding degree of beam polarization (fig.2.4). The results indicate that a filtering mechanism can

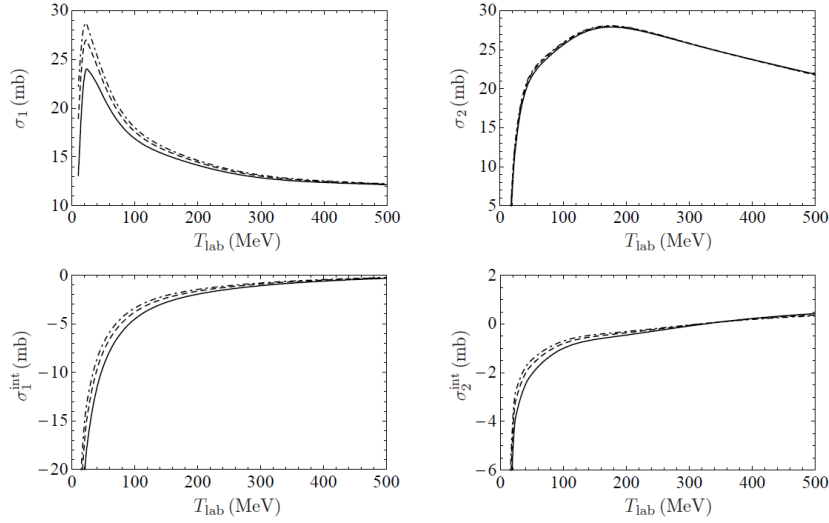


**Figure 2.3:** The dependence of  $\sigma_1$  and  $\sigma_2$  (mb) on  $T_{lab}$  as well as the dependence of  $\sigma_1^{int}$  and  $\sigma_2^{int}$  (mb) (interference contributions) on  $T_{lab}$ . The acceptance angles in the lab frame are  $\theta_{acc}^{lab} = 10$  mrad (solid curve),  $\theta_{acc}^{lab} = 20$  mrad (dashed curve) and  $\theta_{acc}^{lab} = 30$  mrad (dashed-dotted curve) [29].

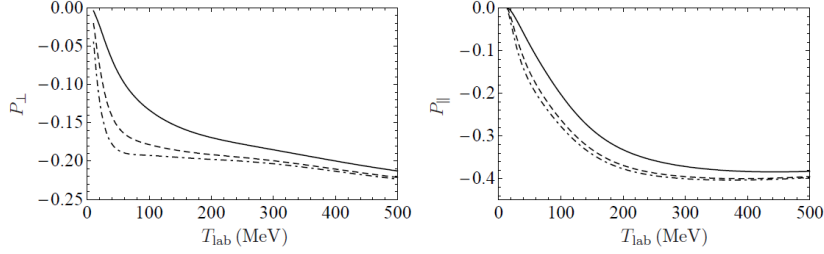


**Figure 2.4:** The dependence of the beam polarization  $P_B(t_0)$  for a target polarization  $P_T = 1$  on  $T_{lab}$  (MeV) for  $P_{\perp} = 0$  and  $P_{\parallel} = 1$ . The acceptance angles in the lab frame are  $\theta_{acc}^{lab} = 10$  mrad (solid curve),  $\theta_{acc}^{lab} = 20$  mrad (dashed curve) and  $\theta_{acc}^{lab} = 30$  mrad (dashed-dotted curve) [29].

provide a noticeable beam polarization in a reasonable time. Different models give significantly different predictions [30] and only experimental investigations of the spin-dependent part of the cross section of  $p\bar{p}$  scattering can prove the applicability of potential models.



# Chapter 3

## Spin-filtering studies at COSY

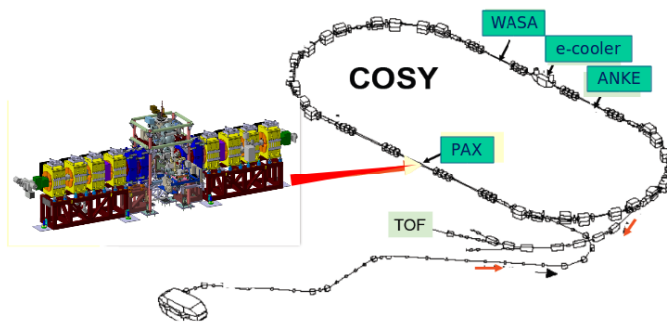


**Figure 3.1:** The COSY ring. In green are highlighted the internal experiments and the electron cooler, while in grey one external experiment. The detail of the PAX interaction point is shown in the expansion.

The method to provide a beam of polarized stored nucleons adopted by the the PAX collaboration is spin-filtering using a polarized internal storage cell target, filled with polarized hydrogen gas. Systematic studies to determine the polarization buildup of a proton beam are carried on at the COSY (fig.3.1). Spin-filtering experiments are crucial to test the present understanding of spin-filtering processes in storage rings.

Aim of the feasibility test at COSY is the measurement of the spin dependence of the  $(pp)$  transverse cross section. This measurement can be accomplished by the determination of the polarization induced in the stored beam through the interaction with a polarized hydrogen target. Since the total cross section is different for parallel and antiparallel orientation of the

beam particle spins relative to the direction of the target polarization, one spin direction is depleted faster than the other, so that the circulating beam becomes increasingly polarized, while the intensity decreases with time.

As already discussed in §2.2, the cross section for a projectile proton impinging on a transversely polarized proton target is:

$$\sigma_{\pm} = \sigma_0 \pm Q\sigma_1 \quad (3.1)$$

where  $+/-$  indicate the two proton spin states and  $Q$  is the target polarization.

As a consequence of the interaction, the number of the spin-up  $N^{\uparrow}$  particles and spin-down  $N^{\downarrow}$  particles decreases exponentially with different time constants leading to a polarization buildup over time that can be described by:

$$P(t) = \frac{N^{\uparrow}(t) - N^{\downarrow}(t)}{N^{\uparrow}(t) + N^{\downarrow}(t)} = \tanh(t/\tau_1) \quad (3.2)$$

The spin-dependent cross section  $\tilde{\sigma}_1$  can be extracted from the time constant  $\tau_1$ :

$$\tau_1 = \frac{1}{\tilde{\sigma}_1 Q d_t f} \quad (3.3)$$

where  $Q$  is the target polarization,  $d_t$  the target density and  $f$  the revolution frequency. In eq.3.3,  $\tilde{\sigma}_1$  indicates the effective polarization cross section in a storage ring and accounts for the fact that only the protons that scatter at angle  $\Theta$  larger than the acceptance angle  $\Theta_{acc}$  effectively contribute to the spin-filtering process  $\tilde{\sigma}_1 = \sigma_1(\Theta > \Theta_{acc})$ .

In section 3.1 the various components of the experimental apparatus and their performances are described. Preliminary results of the measurement are presented in section 3.2 and the COSY ring is briefly presented altogether with the optimization of various accelerator parameters critical for spin filtering experimentation. Section 3.3 accounts for the polarized target located at the PAX Interaction Point (PAX-IP) and for the beam polarimeter and the cluster deuterium target located at the ANKE<sup>1</sup> Interaction Point (ANKE-IP). In section 3.4 the preliminary results of the PAX Collaboration beam time at COSY of August/October 2011 are discussed.

---

<sup>1</sup>Apparatus for studies of Nucleon and Kaon Ejectiles.

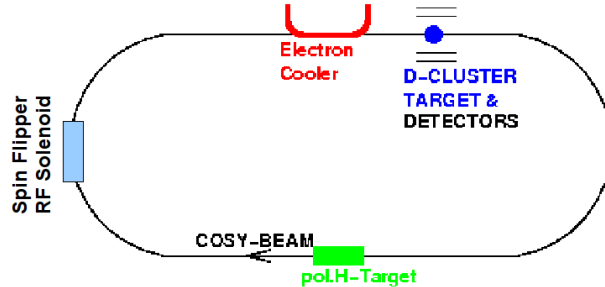


**Figure 3.2:** In the straight section the COSY ring, opposite to the electron cooler, the PAX polarized target installation is located, the RF solenoid of the spin-flipper is located in one of the arcs, its use is further clarified in the text of the report. Behind the electron cooler the detector setup for the beam polarimetry is shown.

### 3.1 Spin filtering cycle

An overview of the COSY ring with the installations utilized in the test is presented in fig.3.2

The sequence of operation in a spin filtering cycle is as follows (see fig.3.3):

- the unpolarized proton beam is injected in the COSY ring at  $48 \text{ MeV}$ . The beam is cooled and accelerated to an energy of  $49.3 \text{ MeV}$  for the measurement. This energy has been chosen because of the  $pd$  analyzing power, as already mentioned. The typical number of particles injected in the ring and accelerated for every cycle was  $5 \cdot 10^9$ .
- After the injection the spin filtering cycle starts. At the PAX Interaction Point the polarized gas is injected into the storage cell and the holding field coils are powered. The typical duration of a spin filtering cycle is  $16000 \text{ s}$ , corresponding to two beam lifetimes.
- The PAX polarized target is switched off after the spin filtering period, then the ANKE deuterium cluster target and the data acquisition of the beam polarimeter are start. The beam polarization is reversed twice by means of the spin flipper during the spin polarization measurements, which allows the determination of the induced beam

polarization for every cycle in order to reduce the systematic errors. The total duration of the polarization measurements is 2500 s.

- Spin filtering cycles are repeated for different directions of the target holding fields. A total of 48 spin filtering cycles with different orientations of the target holding field have been performed and more than  $5 \cdot 10^{-7}$  deuterons and  $2 \cdot 10^{-7}$  elastically scattered protons events have been recorded. A comparable contribution to the statistical error of the final result is expected from the two samples since the analyzing power of the protons is higher than the deuterons analyzing power.

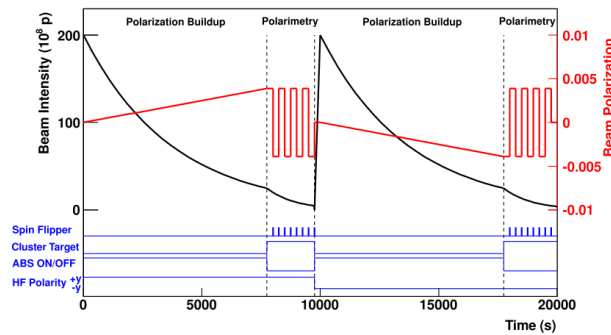


**Figure 3.3:** Schematic representation of a typical spin-filtering cycle. The black curves represent the beam current, while the red ones show the polarization, induced in the beam. While the beam current decreases, the polarization in the beam builds up. At the end of the spin-filtering cycle the spin-flipper was switched on twice to allow for the measurement of the polarization. In the picture, two cycles for different orientations of the target holding field are indicated.

### Zero measurement

A series of cycles without spin filtering has been carried out in addition in order to provide a zero polarization calibration of the detectors. The zero measurement cycle reflected exactly the same sequence of operations, differing only in the number of injected particles (less than  $1 \cdot 10^9$ ) and the duration of the spin filtering part (180 s), in order to be as close as possible to the experimental conditions of a standard filtering cycle. A total number of 98 cycles of this type have been collected, in this way the acquired statistic is twice as large as the one of the spin filtering measurements.

## 3.2 The COSY ring

The spin-filtering studies are performed injecting an unpolarized proton beam inside the COSY ring, then measuring the polarization of the stored proton beam after reiterated passages through an internal polarized gas hydrogen target cell. The small effective polarizing cross section  $\tilde{\sigma}_1$  of eq.3.3 demands for long filtering time. Consequently, particle beam dynamics and beam loss mechanisms have been optimized in order to improve the COSY beam lifetime. The COSY ring has a circumference of  $183m$ , provided with two opposite straight sections each  $40m$  long. Two kind of beams are available, protons or deuterons, for external and internal experiments in a momentum range that goes from  $300MeV/c$  up to  $3700MeV/c$ . Moreover the injected beam can be unpolarized or polarized: protons beam transversely polarized with a polarization of about the 70% and an intensity of about  $1 \cdot 10^{10}$  particles, or deuterons beam with a vector polarization value bigger than 70%, a tensor polarization above the 50% and an intensity of about  $3 \cdot 10^{10}$  particles. The stored beam can be cooled by means of an  $100KeV$  electron cooler or by stochastic cooling above  $1500MeV/c$ . The COSY ring hosts different experimental setups (fig.3.1): the PAX interaction point where the spin-filtering process takes place, the Time Of Flight (TOF) spectrometer, the Wide Angle Shower Apparatus (WASA) detector and the Apparatus for studies of Nucleon and Kaon Ejectiles (ANKE) magnetic spectrometer, where the stored beam polarization measurements are performed.

For spin-filtering studies, the COSY accelerator has been operated at an energy of  $T = 49.3 MeV$ , slightly above injection energy. The reasons of this particular choice are twofold: the first reason is the precise analyzing powers  $A_y$  for polarization analysis available at that energy [47] (§3.4), and the second is the fact that the polarization cross section is large at low energies (see [ref]).

An improvement of the beam lifetime to about  $6000s$  without target, indispensable for the spin-filtering experiments at COSY, has been achieved as a result of various machine studies (§3.2.1). These studies included an improvement of the COSY vacuum environment (§3.3.3), the adjustment of the machine tune, closed orbit corrections, adjustment of the electron cooler performance, and studies on single intra-beam scattering effects. A low- $\beta$  section was installed to avoid the acceptance limitation due to the storage cell.

### 3.2.1 Beam lifetime and acceptance

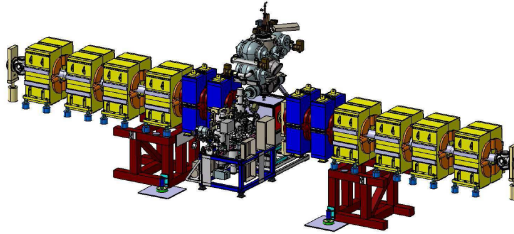


**Figure 3.4:** PAX installation at COSY ring: in yellow the already existing COSY straight section quadrupole magnets and in blue the four additional quadrupoles needed for the low- $\beta$  section. Mounted above the target chamber is visible the atomic beam source.

The interaction of the proton COSY beam with the hydrogen gas target at the PAX-IP requires the beam passing through the storage cell which implies that a substantial amount of the particles of the beam could be scattered out of the acceptance at the target location.

The low- $\beta$  section was installed to avoid the acceptance limitation due to the storage cell. This apparatus includes four additional quadrupole magnets (depicted in blue in fig.3.4) which can be switched on adiabatically, four steerer magnets mounted directly inside the adjacent COSY quadrupole magnets and a pair of **Beam Position Monitors** (BPM).

Excellent vacuum conditions in the COSY ring were provided by the NEG<sup>2</sup> pump (§3.3.3) installed below the target chamber together with the activation of the neighbouring NEG coated tubes (produced at CERN). The combination of the good vacuum and the effect of the low- $\beta$  section at the PAX-IP produced a situation in which almost no effect on the beam lifetime could be detected after injection of the polarized gas in the storage cell of the chamber; the same vacuum configuration is planned to be installed at CERN. During the spin filtering cycles the measured beam lifetime was  $\tau_{beam} > 8000$  s exceeding the expectations and allowing for longer spin filtering cycles than what was initially planned.

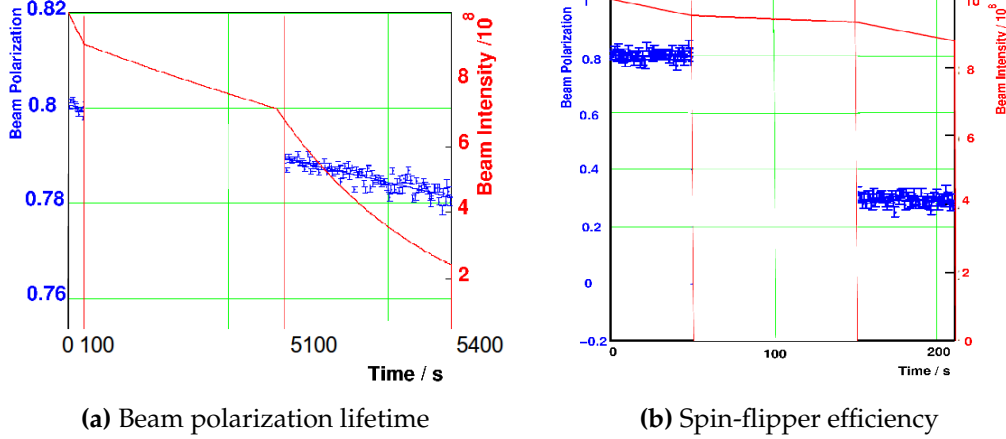


**Figure 3.5:** (a). Measurement of the beam polarization lifetime. A polarized proton beam has been injected in the ring and its polarization measured at injection and after a storing period of 5000 s in the ring. From the comparison of the two values the beam polarization lifetime could be deduced. (b). Measurement of the spin-flipper efficiency. The spin-flipper efficiency has been determined by injecting a polarized beam and comparing its polarization at injection and after 99 induced spin-flips.

### 3.2.2 Beam polarization lifetime and spin flipper efficiency

The polarization lifetime of the COSY beam has been measured prior to the spin filtering experiments. The measurement has been performed by injecting a polarized proton beam into COSY and comparing the polarization at the beginning of a fill and after the beam was stored in the ring for 5000 s (see fig.3.5a). The prediction that no depolarizing resonances are present in the neighbourhood of the chosen machine tunes was confirmed by the fact that during the elapsed time of 5000 s the polarization loss amounted to about the 5% resulting in a polarization lifetime  $\tau_{pol} = (2 \cdot 10^5 \pm 5 \cdot 10^4)$  s. From the point of view of the polarization buildup experiment, the beam polarization lifetime can be considered as infinite.

At every measurement cycle spin flips of the polarization have been introduced in order to reduce systematic errors. The spin flipper employs a resonant RF-solenoid and is part of the standard equipment of the COSY ring (fig.3.2). The spin flipper has been tuned to the proper working conditions and its efficiency has been measured in dedicated runs, before the

---

<sup>2</sup>Non-Evaporable Getter.

measurements. A polarized proton beam was injected in the ring and its polarization was measured; after that the spin flipper was switched on and off for a total number of 99 spin flips induced on the beam, then the polarization of the beam was measured again (see fig.3.5b). From the comparison between the initial and final polarization of the beam, the spin flipper efficiency has been determined as  $\varepsilon_{SF} = 0.987 \pm 0.001$ .

### 3.3 PAX experimental setup

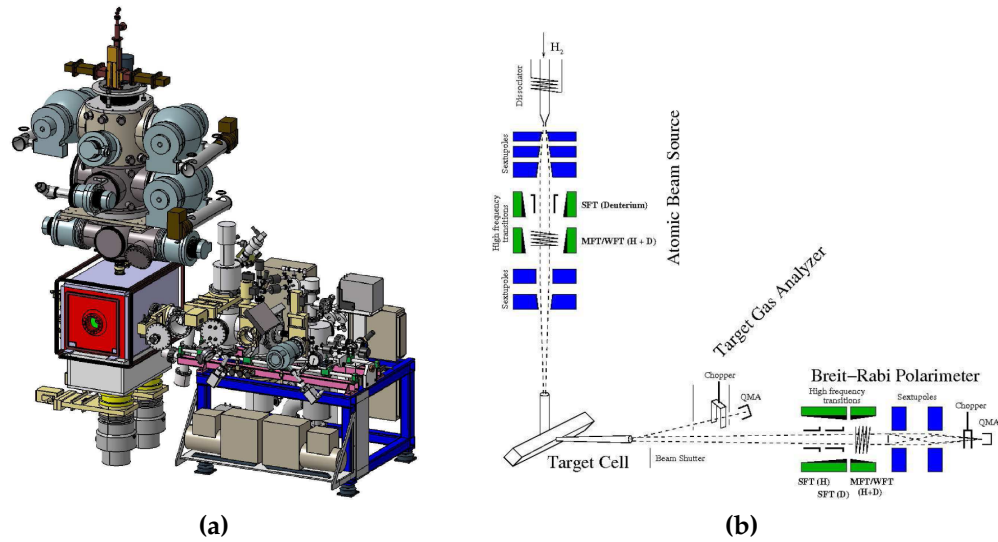


**Figure 3.6:** PAX target. (a). On the top of the target chamber the ABS is installed. Inside the target chamber the storage cell is hosted. On the right side of the chamber is mounted the BRP. (b). Schematic view of the target setup with the sextupole magnet system and the radio-frequency transition units.

At the PAX interaction point the whole setup is assembled in a straight section of the COSY ring (see fig.3.2). The PAX target components are a polarized atomic beam source, a **Breit-Rabi Polarimeter (BRP)** and a storage cell.

In the ABS, polarized hydrogen or deuterium atoms are prepared and then injected into the storage cell. From the storage cell, as depicted in figure 3.6b, a sample of the gas target propagates toward the BRP (where

the atomic polarization is measured, see §3.3.2) and toward the Target Gas Analyzer (TGA) (where the gas ratio of atoms over molecules is measured).

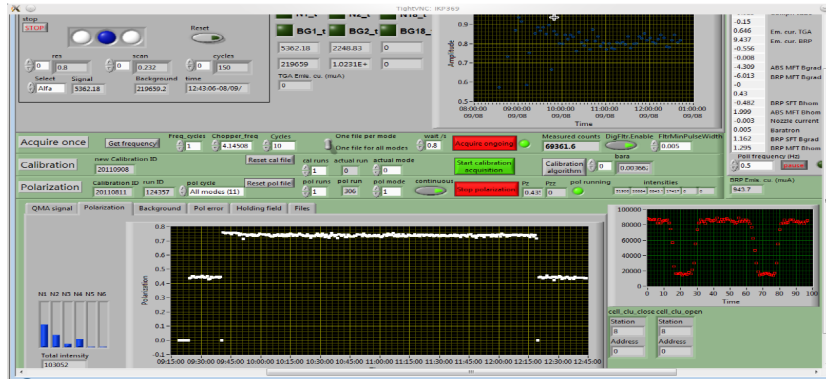


**Figure 3.7:** Online screen shot of the target polarization from the Labview control program. Both the atomic beam polarization (lower plot with white points) and the atomic fraction (upper plot with blue points) were continuously monitored by the Breit-Rabi polarimeter and the Target Gas Analyzer, respectively.

The thickness of the target depends on the diameter of the storage cell which is  $10\text{ mm}$ ; moreover the cell is  $400\text{ mm}$  long and provides a square cross section of  $10 \times 10\text{ mm}^2$ , with target density up to  $5 \cdot 10^{13}\text{ atoms/cm}^2$ . The density in the target cell was measured through the observed beam deceleration induced by the target gas detected by the Schottky signal and resulted in a value larger than  $5 \cdot 10^{13}\text{ atoms/cm}^2$  for one injected hyperfine state from the ABS. Furthermore this value was consistent with the expectations calculated from the known ABS flux ( $3 \cdot 10^{16}\text{ atoms/s}$ ) and the known conductance of the storage cell.

The vertical weak holding magnetic field ( $B = 10\text{ G}$ ) required to define the quantization axis for the target polarization was provided by the coils mounted at the chamber (see §3.3.4).

The target polarization was continuously monitored by the Breit-Rabi polarimeter during data taking; the value was found to be constant in time and larger than  $Q_y = 0.7$ . In fig.3.7 is presented an online screenshot of the Labview control program of the target polarization.

### 3.3.1 Atomic beam source

The atomic beam source constituents are:

- a dissociator;
- a differential pumping system;
- a beam forming system;
- a sextupole magnet system which focuses  $m_s = +\frac{1}{2}$  atoms into the storage cell;
- a set of adiabatic high-frequency transitions in order to manipulate the hyperfine population of the atomic beam.

A scheme of the ABS is given in figure 3.6b, hydrogen fluxes of  $\Phi^{ABS} \approx 6.5 \times 10^{16} \text{ atoms/s}$  (2 two injected hyperfine states) and deuterium fluxes of  $\Phi^{ABS} \approx 5.8 \times 10^{16} \text{ atoms/s}$  (three states injected) have been measured.

### 3.3.2 Target gas analyzer and Breit-Rabi polarimeter

The Breit-Rabi polarimeter measures the total target polarization counting the atoms as well as the molecules that constitute the target, the recombination of target atoms into molecules on the cell surface is taken into account though it is a minor process. The atomic and molecular content of the gas sampled from the storage cell is measured by the target gas analyzer (TGA) which is embedded in the BRP sextupole chamber (pumped by two cryopumps and a titanium sublimation pump<sup>3</sup>). The TGA setup comprises a chopper and a  $90^\circ$  off-axis Quadrupole Mass Spectrometer (QMS) equipped with a cross beam ionizer and a Channel Electron Multiplier (CME) for single ion detector purposes. The TGA vacuum chamber is baked at temperatures up to  $180^\circ\text{C}$  for 48 hours before to start working and during the operation the TGA detector pressure is about  $4 \cdot 10^{-9} \text{ mbar}$ .

The BRP employs two sets of RF-resonators, one for hydrogen, and one for deuterium operation. The frequency for two-level transitions ( $\Delta F = \pm 1$ ) is of the order of the hyperfine splitting energy ( $\Delta W$ ) at  $B = 0$ . For H it corresponds to the transition  $F = 0 \rightarrow F = 1$  at  $B = 0$ , the *famous* 21 cm line in the cosmic microwave background. The transition frequencies in hydrogen (deuterium)  $\Delta W/h$  are 1421.4 Mhz (327.4 Mhz). For the spin-filtering studies at COSY an innovative dual cavity has been implemented which allows to operate the BRP as needed and which provides RF-field

<sup>3</sup>The total pumping speed is up to  $7000 \text{ ls}^{-1}$ .

configuration for two-level transitions, both for hydrogen and deuterium in a tilted-field geometry. In particular, two independent pairs of resonator rods with separate coupling and pick-up loops are arranged parallel to the beam axis in two planes tilted by  $\pm 45^\circ$  with respect to the median plane. It has been demonstrated that they can be tuned independently to their respective transition frequencies at about  $1430\text{ MHz}$  (H) and  $330\text{ MHz}$  (D) without interference. It is then possible to operate the BRP consecutively with H and D (or vice versa) with very short time intervals in between<sup>4</sup>.

### 3.3.3 Target chamber and vacuum system

The PAX-IP is equipped with a high performance differential pumping system which is capable to keep good vacuum conditions in the target chamber as well as in the adjacent storage ring sections. This is fundamental in carrying on a spin-filtering experiment. The residual gas of the COSY sections contributions to the beam lifetime duration was measured during the commissioning of the target chamber and it was decided that the pumping system must be provided with non-evaporable getter coating to the adjacent beam pipes and it must comprise the following elements:

- two turbo pumps for the pre-vacuum;
- a system of ten NEG pumps;
- two flow limiters tubes placed onto the upstream and downstream walls of the target chamber, both  $80\text{mm}$  long and with an inner diameter of  $19\text{mm}$ .

A new NEG pumping system, designed and constructed by the FZJ-IKP mechanical workshop, was installed below the PAX target chamber and put into operation during the 2011 summer shutdown. The pump was realized by a battery of twelve NEG cartridges. A mechanical shutter separating the pump from the chamber was closed during the activation of the cartridges at  $450^\circ\text{C}$  (see fig.3.8), in order to limit the temperature in the target chamber to less than about  $80^\circ\text{C}$ . According to the design specifications a pumping speed of  $12000\text{ l/s}$  was measured by means of a calibrated  $\text{H}_2$  gas inlet.

The use of the pump during the COSY operations allowed the achievement of a target chamber pressure in the  $10^{-10}\text{ mbar}$  range without gas load

---

<sup>4</sup>Mandatory for the implementation at the AD ring.

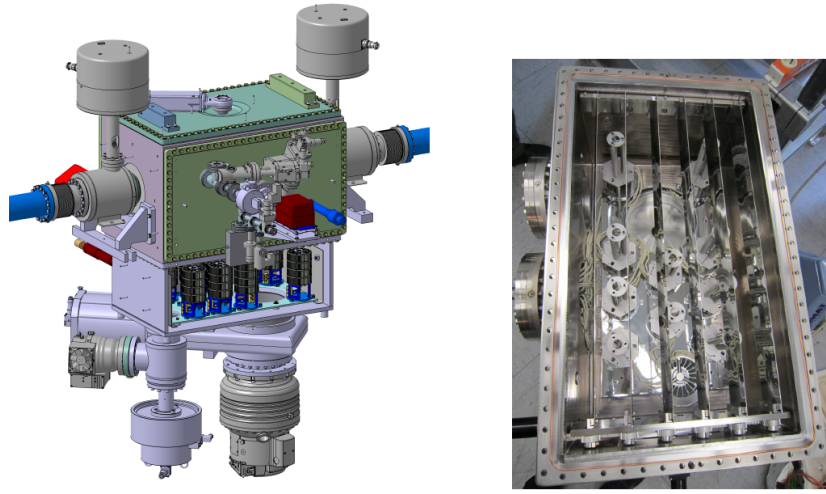


**Figure 3.8:** Schematic view of the target chamber on top of the newly installed NEG pump. Left and right to the target chamber the fast closing shutter valves can be seen as requested by the CERN vacuum regulation. Right panel: inner view of the NEG pump. The NEG cartridges are mounted on the bottom of the chamber; the opened mechanical shutter is clearly visible.

from the ABS and in the low  $10^{-8}$  mbar range with  $H$  gas injected from the ABS in one hyperfine state ( $3 \cdot 10^{16}$   $H$  atoms/s).

### 3.3.4 Holding field

A system of coils which generates magnetic fields in the order of  $1mT$  along the  $x$ ,  $y$  and  $z$  axis has been built by the ZentralAbteilung Technologie (ZAT) of the FZJ [57] in order to provide a guide field system for the operation with the polarized target.

With the vertical ( $y$ ) coils operating in compensation mode and using the frame system, the deflection of the beam in the target chamber was determined: its value was  $0.33$  mm toward the  $x$  direction at the center of the target cell, which fits with the calculations. The model calculations also predicted very well the overall vertical beam orbit changes with uncompensated holding field that were less than  $2$  mm, moreover the holding fields did not affect the beam lifetime.

The use of compensation coils in front and behind the main holding field coils allowed for an almost perfect compensation of the beam displacement:

no transverse displacement of the beam position could be detected by the beam position monitors when powering the holding field coils.

### 3.3.5 Beam polarimeter

The beam polarization after spin-filtering has been measured by detecting the left-right asymmetry in  $p^\uparrow d$  elastic scattering.

The differential cross section for the interaction of a transversely polarized proton beam impinging on a unpolarized deuterium target is given by:

$$\frac{d\sigma}{d\Omega} = \frac{d\sigma_0}{d\Omega}(\Theta)[1 + PA_y(\Theta) \cos(\Phi)] \quad (3.4)$$

where  $d\sigma_0/d\Omega$  is the unpolarized differential cross section,  $A_y(\Theta)$  is the analyzing power and  $\Theta$  and  $\Phi$  the polar and azimuthal scattering angle in the laboratory system. As said before, solid experimental data exist for the analyzing power  $A_y$ , at the energy of which the experiment was performed (49.3 MeV) [47].

At the ANKE interaction point a deuterium cluster target is installed as internal target (see fig.3.9). The cluster target is built of two main part:

**cluster source** which produces the clusters. Gas of pure deuterium (or hydrogen) is cooled below the vapor pressure curve until its temperature reaches a value in the range between  $20 \div 30K$ . The gas then is pressed through a laval nozzle with a pressure of  $15 \div 20bar$ . The nozzle drives the gas into the skimmer chamber and its diameter is of  $20\mu m$ . In the skimmer chamber the gas expands adiabatically and cools down to lower temperatures. In that way the atoms of oversaturated gas condense spontaneously to clusters. The result of this process are clusters containing more or less  $10^3$  atoms that are close to the triple point. The main function of the skimmer is to divide the clusters from the residual gas which constitutes the main part of the total gas load in the skimmer chamber. A shutter closes/opens the skimmer accesses so that the target can be switched on/off in less than 1s. Below the skimmer are installed a collimator, which cuts the cluster beam, and a cryo-pump which is supposed to reduce the gas load into the COSY ring;

**collector** which is made by three cryo-pumps plus one turbomolecular-pump and located under the target chamber. The collector is meant

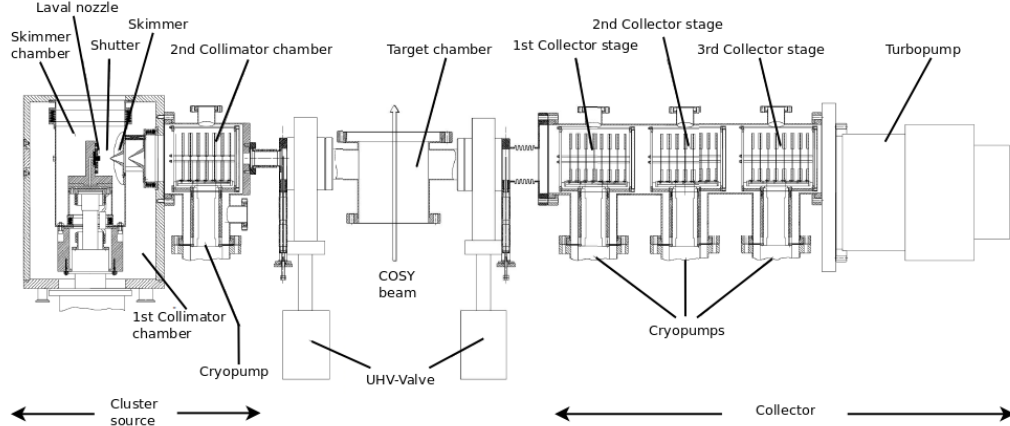


**Figure 3.9:** Schematic view of the ANKE cluster target.

to highly cut down the gas load produced by the cluster beam. The cluster beam directly hits the rotor blades of the turbomolecular-pump and in that way it is directly pumped. The three cryo-pumps act as differential pumping system between the target chamber vacuum and the turbomolecular-pump vacuum which value is over  $10^{-5} \text{ mbar}$ .

The products of the interaction between the stored beam and the cluster target are detected by the silicon tracking telescopes (STTs) located at the sides of the interaction point (fig.3.11). The events collected by the telescopes are then processed by the dedicated Data Acquisition (DAQ) system which serves the online monitoring as well as the data storage. Elastically scattered deuterons and protons were clearly identified by the deposited energy in the different layers. No background for deuterons is expected due to the low energy of the reaction, though some small background coming from deuteron breakup is expected for protons.

The trigger system dedicated to the STTs<sup>5</sup> was configured accordingly to the aim of the polarization measurements. The present apparatus comprises few NIM<sup>6</sup> modules which host the logic gates needed to perform the logic operations to mark the significant collected events. A conceived new trigger system should replace the obsolete system in order to ensure a modular expandible trigger system along with a online programmable trigger logic.

<sup>5</sup>Silicon Tracking Telescopes.

<sup>6</sup>Nuclear Instrumentation Module.

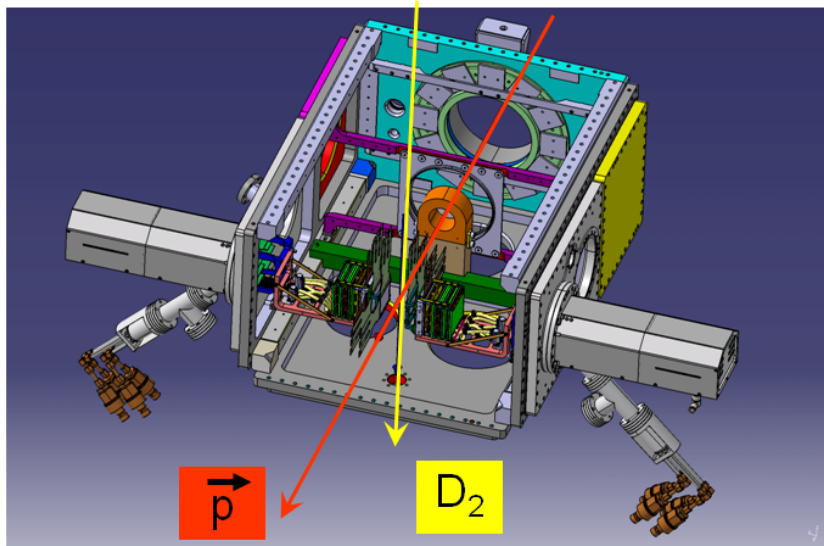


**Figure 3.10:** Experimental setup for the measurement of the beam polarization as it was already used during the beam time. The cluster target beam comes from the top and crosses the polarized proton beam stored in the machine. Elastically scattered deuterons are detected by a couple of silicon telescopes.

In the next chapter (ch.4) the new trigger board and its commissioning will be described.

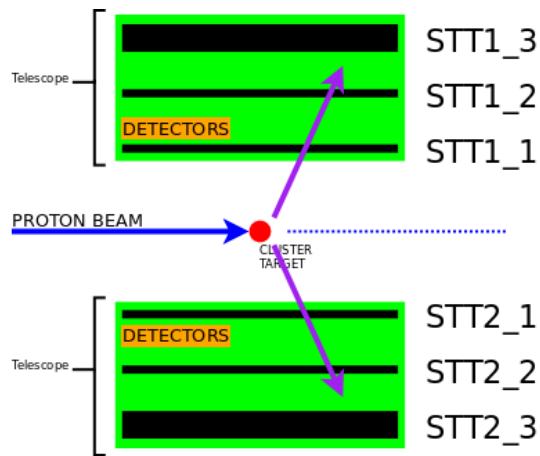


**Figure 3.11:** Schematic top view of the telescopes setup at the ANKE interaction point.

### 3.3.6 Detectors

The elastic events produced by the  $p d$  interaction in the cluster target are revealed by the detectors depicted in fig.3.11. As mentioned in §3.3.5, the detection process is performed by two STTs installed at the ANKE interaction point close to the area where the beam hits the deuterium cluster target. The detection system was conceived to handle the data coming from the double polarized proton-proton ( $p p$ ) or proton-deuteron  $p d$  collisions. The underlying concept of the detection system is to combine the  $\Delta E/E$  identification method of the stopped particle with the particle tracking method over a wide energy range. The main features of the employed double-sided silicon strip detectors are:

**different thickness** each telescope is composed by three detectors of different thickness, the one closest to the interaction area is  $69\mu m$  thick, the one that comes next is  $300\mu m$  thick and they are the so-called *thin detectors* fitting with the particle tracking purposes. The outermost detector is the so-called *thick detector* and it is  $5500\mu m$  thick (this one in particular is meant to improve the *stopping power* of the telescope and along with that it is supposed to precisely measure the particles energy loss and validate the tracks detected by the two innermost detectors);

**self-triggering** each particle crossing event is quickly identified and generates a trigger signal by means of a fast amplifier featured by a peak time of  $75ns$ . In this way the system could work even as a standalone detector.

Furthermore the telescopes are served by high dynamic range chips. A more detailed description of the detectors is given in appendix A, §A.1 and §A.2.

### 3.3.7 Front-end electronics

The detectors installed in the telescopes can work either in vacuum or in air: at the ANKE interaction point they work in vacuum. Working in vacuum leads to the problem of the connection with the external readout system that must be accomplished trying to minimize the number of the required feedthroughs in order to reduce as much as possible the chance of occurring leaks that could spoil the vacuum.

### 3.4. EXTRACTION OF EFFECTIVE POLARIZING CROSS-SECTION $\tilde{\sigma}_1$ 51

At the IKP institute was developed a vacuum compatible front-end board expressly to meet the requirements of the detection system employed at the ANKE interaction point. Besides the need of minimize the number of feedtroughs, one of the most challenging tasks in the realization of the board was dealing with the signals coming from the detectors working in a quite wide energy range. For that reason a chip was conceived on purpose in collaboration with the Norwegian company IDEAS, the VA32TA chip. A more detailed description of the detectors is given in appendix A, §A.3.

## 3.4 Extraction of effective polarizing cross-section

$\tilde{\sigma}_1$

The effective polarizing cross section can be extracted through the polarization buildup rate  $dP/dt$ . The result of deriving eq.3.2 is:

$$\frac{dP}{dt} \approx \frac{1}{\tau_1} = \tilde{\sigma}_1 Q d_i f \quad (3.5)$$

where the meaning of the single terms has already been introduced. In the following we describe how the single terms have been individually measured.

### Target Polarization

The average target polarization  $Q$  can be expressed as

$$Q = \alpha P \quad (3.6)$$

where  $\alpha$  is the hydrogen atomic fraction  $\alpha = n_H/(n_H + 2n_{H_2})$  and  $P$  is the atomic polarization  $P = (N^\uparrow - N^\downarrow)/(N^\uparrow + N^\downarrow)$ . The atomic fraction has been continuously monitored by the target gas analyzer during the measurement and resulted stable within  $\pm 0.01$  with a value of  $\alpha = 0.85 \pm 0.01$ . The atomic polarization has been continuously monitored during the measurement and resulted stable within  $\pm 0.01$  with a value of  $P = 0.79 \pm 0.01$ . The two values combine to a final value for the target polarization of

$$Q = \alpha P = 0.67 \pm 0.014 \quad (3.7)$$

### Target density

The absolute density of the target has been directly measured by means of the variation in Schottky signal caused by the beam deceleration in the interaction with the target gas. The measured value of the target polarization is

$$d_t = (5.5 \pm 0.2) \cdot 10^{13} \text{ atoms/cm}^2 \quad (3.8)$$

### Beam polarization

The beam polarization after spin-filtering has been measured by detecting the left-right asymmetry in  $p^\uparrow d$  elastic scattering.

The asymmetry determination is based on the identification of deuterons stopped in the second or third detector layer by means of the  $\Delta E/E$  method. Since the data are taken below the pion-production threshold, an identified deuteron ensures that elastic scattering took place. The asymmetry  $\epsilon$  used in the extraction of the beam polarization has been evaluated by means of the *cross ratio method*. The method provides cancellation of all first order fake asymmetries caused by difference in acceptance, efficiency and integrated luminosity in the two detectors

$$\epsilon = \frac{\delta - 1}{\delta + 1} = PA_y \quad (3.9)$$

where  $\delta$  is the cross ratio defined by means of the rates  $Y_{R,L,\uparrow,\downarrow}(\Theta, \Phi)$  detected in the left and right (L and R) detectors for the spin up and down states ( $\uparrow$  and  $\downarrow$ ):

$$\delta = \sqrt{\frac{Y_{L\uparrow}(\Theta, \Phi) \cdot Y_{R\downarrow}(\Theta, \Phi)}{Y_{L\downarrow}(\Theta, \Phi) \cdot Y_{R\uparrow}(\Theta, \Phi)}} \quad (3.10)$$

The polarization has been extracted by fitting the asymmetry binned in  $\Theta$  angles of  $3^\circ$  with a  $5^{th}$  order interpolation to the measured analyzing power taken from [47]. The analyzing power in each bin was assumed constant. The effect of the geometrical acceptance over the azimuthal angle can be considered negligible in the given geometry.

# Chapter 4

## Ferrara trigger board

The COSY data acquisition apparatus is triggered by the combination of the forward detection system and silicon tracking telescopes readout. The trigger system is supposed to generate a trigger signal which will mark a detected event accordingly to the trigger logic agreed for the ongoing experiment purposes. The presently existing COSY trigger system consists of NIM<sup>1</sup> modules and cables arranged to build up the trigger logic.

The COSY setup fits the experimental requirements as long as there is no need of making major changes in the trigger logic nor need of handling detection configurations composed by many telescopes. In these last cases indeed NIM based systems have proved themselves to be scarcely adaptable and highly complicated to manage, especially when it comes to set the logic functions which may be based over more than one logic level. The PAX collaboration is building a new detection system which will host 36 detectors, and will require an update of the old NIM trigger system. To fulfill the need of a more flexible and efficient trigger system for the future foreseen PAX Collaboration experiments, the Ferrara University and INFN electronic workshop conceived and realized a new trigger system embedded in an electronic board which comprises programmable and timing devices.

The new trigger board (PAX\_TB), it is a one-unit wide VME<sup>2</sup> 6U module and has been conceived following few basic principles:

- high modularity and flexibility;
- programmable internal logic;

---

<sup>1</sup>Nuclear Instrumentation Module standard.

<sup>2</sup>Versabus Module Eurocard.

- fast time response.

The result of merging these principles with the technical constraints is an electronic board which is mainly featured by two elements: a Field Programmable Gate Array (FPGA) and a Complex Programmable Logic Device (CPLD). Furthermore the board hosts many other devices that contribute to the final aim of having a trigger system embedded in a portable electronic board.

In §4.1 the components of the new trigger board are described, in §4.2 the many steps accomplished during the board development and commissioning are presented.

## 4.1 Trigger board description

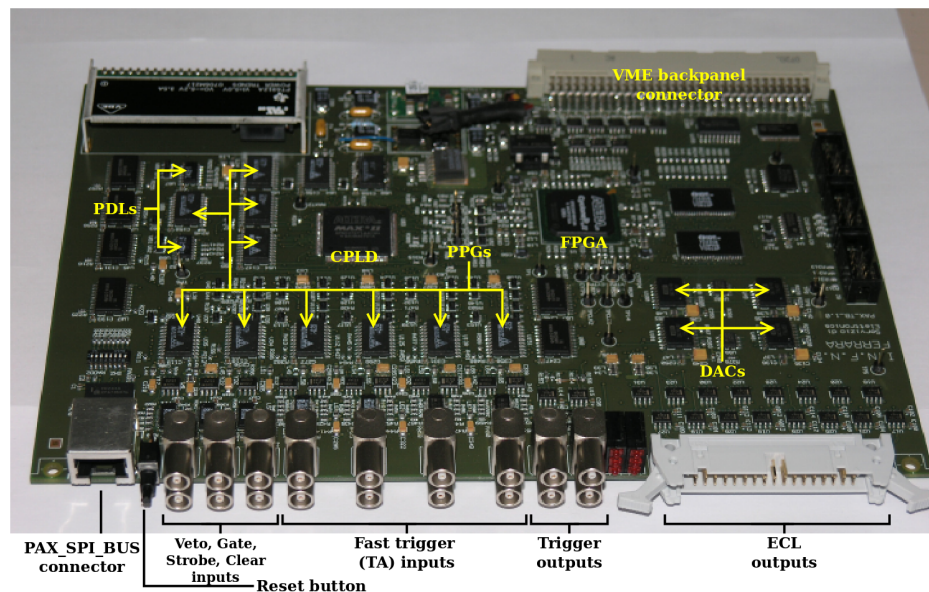


**Figure 4.1:** A global view of the PAX trigger board. The front panel connection are described and some of the onboard chips are highlighted. It is not possible to see the complete set of PPGs and PDLs because part of them is installed on the other side of the board.

The PAX\_TB comprises many different elements: it hosts **Digital-to-Analog Converters (DAC)**, **Programmable Delay Lines (PDL)**, **Programmable**

Pulse Generators (PPG) and, as already mentioned, it hosts an FPGA and a CPLD which oversee all the board functionalities. Moreover it is provided with all the input/output (I/O) connectors needed for the implementation in the COSY ring DAQ framework.

### 4.1.1 Digital-to-Analog Converter

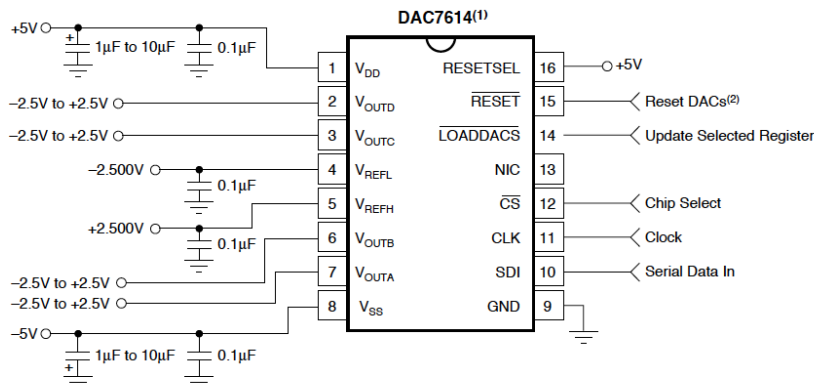


Figure 4.2: DACs pin layout.

The Digital-to-Analog Converters<sup>3</sup> [66] (fig.4.2) are powered by a dual supply  $\pm 5V$  (positive analog supply voltage  $V_{DD} = +5V$  and negative analog supply voltage  $V_{SS} = -5V$ ) which sets the minimum voltage output reference input and the maximum voltage output reference input respectively to  $V_{REFL} = -2500mV$  and  $V_{REFH} = +2500mV$ . The reference input voltage can cover any voltage in the range defined by  $V_{SS} + 2.25V$  and  $V_{DD} - 2.25V$  with the only constraint that  $V_{REFH} - V_{REFL} > 1.25V$ . The maximum output of each DAC corresponds to  $V_{REFH}$  plus a small offset voltage while the minimum output of each DAC is given by  $V_{REFL} - 1LSB$ <sup>4</sup> plus the small offset voltage already mentioned. Note that  $V_{SS}$  sets several bias chip points and for that reason it must either be connected to ground or it must lay in the voltage range  $(-4.75 \div -5.25)V$ . When this condition is not satisfied the bias values may not be properly set.

<sup>3</sup>Quad, Serial Input, 12-Bit, Voltage Output DIGITAL-TO-ANALOG CONVERTER from BURR-BROWN®: model DAC7614U.

<sup>4</sup>LSB=Less Significant Bit.

Each DAC is equipped with four outputs ( $V_{OUTA}$ ,  $V_{OUTB}$ ,  $V_{OUTC}$ ,  $V_{OUTD}$ ) in principle independent from each other except for the fact that they share the reference voltage inputs ( $V_{REFL}$ ,  $V_{REFH}$ ). The digital input (SDI) decodes 16-bit serial words which contain the 12-bit DAC code (used to set the value of the output voltage), the 2-bit address code (to select the output which must be set) and 2 unused bits.

The voltage value of each output, programmed via the serial interface SDI, can be varied over 4095 equal steps from  $V_{REFL}$  to  $V_{REFH}$  according to the formula

$$V_{OUT} = V_{REFL} + \frac{(V_{REFH} - V_{REFL}) \cdot N}{4096} \quad (4.1)$$

where  $N$  is the digital input code which is written as a decimal voltage value.

### 4.1.2 Timing devices

The Programmable Delay Lines<sup>5</sup> (usually called delay chips or delayers) [65] (fig.4.3a) are comprised of four delay lines that operate independently. Each signal which comes to the input of a delay line is reproduced at the corresponding output shifted in time.

Actually a delay line is a memory device: the information coming at the input is stored for a time equal to the delay setting before to be released at the output. Each 4-bit delay line is composed by fifteen delay elements (cells) serially connected, every of which consents to store data for a time interval correspondent to the device increment<sup>6</sup>. The delay chip is provided with a serial interface, serial data in (SI), which is used for the device setting. The setting of a delay value over a line is done connecting the output pin of the delay line with one of the cells that build the line itself. Each delay line can be programmed independently.

The delay lines are featured by the so-called inherent delay. The inherent delay is the time shift wich afflicts every signal passing through a delay line when the delay value of that line has been set to zero, for the PDLs

<sup>5</sup>MONOLITHIC QUAD 4-BIT PROGRAMMABLE DELAY LINE (SERIES 3D7424) produced by *data delay devices*<sup>®</sup>

<sup>6</sup>The PDL chip models are many and they differ for the minimum delay increment that can be performed over each delay line; the delay increments vary in the range  $(0.75 \div 400)ns$ .

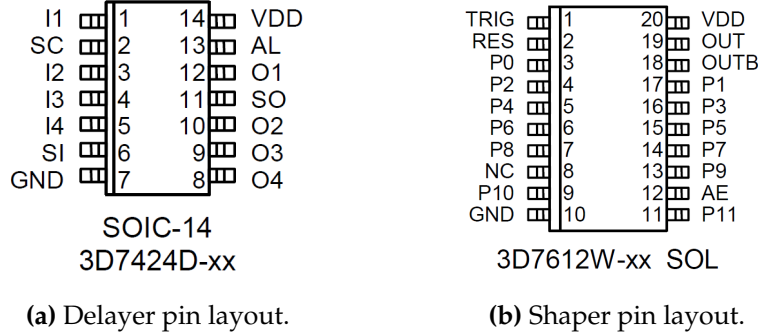


**Figure 4.3:** Layout of the programmable timing devices.

the value of the inherent delay typically corresponds to  $6 \text{ ns}^7$ . The device operates at  $5 \text{ V}$ .

Each line output can be enabled or inhibited by the corresponding *enable bit*. The delay values are programmed through the serial interface and can be set in a range divided in fifteen equal steps, the size of which depends on the device model. For each line the delay time is given by:

$$Delay\_time^{line} = Inherent\_Delay + (Delay\_Step \cdot N^{line}) \quad (4.2)$$

where  $N^{line}$  is the digital input code which is written as a decimal value.

In order to reach delay values bigger than the values allowed from a single delay line, it is possible to serially connect many delay lines. What must be taken into account is the fact that in this case even the inherent delay will increase following the rule:

$$Total\_Inherent\_Delay = Inherent\_Delay \cdot n \quad (4.3)$$

where  $n$  is the number of delay lines connected in series.

The Programmable Pulse Generators<sup>8</sup> (commonly called shapers) [64] (fig.4.3b) are 12-bit programmable devices. The pulse width, programmable via the parallel interface, can vary in a range divided in 4095 equal steps and follows the rule:

$$Pulse\_Width = Inherent\_Width + (Width\_Step \cdot N) \quad (4.4)$$

<sup>7</sup>This has been measured and verified by a test that I performed in 2007 for my bachelor thesis.

<sup>8</sup>12-BIT PROGRAMMABLE PULSE GENERATORS (SERIES 3D7612: PARALLEL INTERFACE) produced by *data delay devices*<sup>®</sup>.

where  $N$  is the digital input code written as a decimal value and  $Width\_Step$  depends on the selected PPG. As for the PDLs, even the 12-bit PPG models are many and differs only for the minimum width increment that can be set; the  $Width\_Step$  values vary in the range  $(0.25 \div 50000)ns$ .

A rising edge on the input (which is referred to as  $TRIG$  in figure 4.3b) gives start to the pulse at the outputs ( $OUT$  and  $OUTB$ ), the pulse expires after the programmed pulse time width has elapsed. The inherent pulse width has been measured to amount to  $13 ns$ <sup>9</sup>. The device is also provided with a reset input (figure 4.3b  $RES$ ) which becomes useful in case comes the need of terminate the pulse before the programmed time has expired.

### 4.1.3 Complex Programmable Logic Device

The Complex Programmable Logic Device implemented on the PAX\_TB is an ALTERA® MAX® II family instant-on, non-volatile CPLD based on a  $0.18\mu m$ , 6-layer-metal-flash process with a density of 1270 logic elements (LEs) and a non-volatile storage memory of 8 *Kbits*. The CPLD contains a two dimensional row- and column-based architecture to implement custom logic; the row and column interconnects provide signal connections between the logic array blocks (LABs).

One LAB comprises ten logic elements, a LE is a small logic unit which provides the implementation of the logic functions. LABs are grouped into rows and columns across the device, moreover the device is provided with a global clock network. A flash memory block is embedded within the CPLD floorplan, the majority of this storage memory is partitioned as the dedicated configuration flash memory (CFM) block. The CFM block provides the non-volatile storage for all the SRAM configuration informations; the CFM automatically downloads and configures the logic and input/output (I/O) at power-up providing instant-on operation.

An LE is a logic unit which contains a four inputs look up table (LUT) that works as a functions generator which can implement any four variables function. Furthermore each LE is provided with a programmable register which can be configured for D, T, JK or SR operations<sup>10</sup>, and with three

<sup>9</sup>The inherent pulse width has been measured by me in 2007 for the job done for my bachelor thesis.

<sup>10</sup>The D, T, JK and SR are different kinds of flip-flop: D means *delay* flip-flop, T *toggle* flip-flop, SR *Set & Reset* flip-flop and JK is basically an SR flip-flop but for the fact that it has no forbidden output states.

outputs which can be driven independently by the LUT and by the register for unrelated functions.

The whole trigger logic implemented by the trigger board is totally housed inside the CPLD, that implies the logic is quickly programmable and completely reprogrammable (which are the main reasons why the PAX\_TB has been conceived).

#### 4.1.4 Field Programmable Gate Array

The Field Programmable Gate Array embedded on the PAX\_TB is an ALTERA® Cyclone® II FPGA, manufactured on 300 *mm* wafers using TSMC's<sup>11</sup> 90 *nm* low-k dielectric process.

The architecture of the FPGA is two dimensional row- and column-based, it embeds logic array blocks (LABs), memory blocks (M4K) and multipliers. The LABs are made by sixteen LEs, the device LEs density is of 14448. The Cyclone® LEs can work in two different operating modes: normal mode or arithmetic mode, where the six available inputs to the LE are directed to different destinations to implement the desired logic function. The normal mode is suitable for general logic applications and combinational functions, while the arithmetic mode is ideal for the implementation of adders, counters, accumulators and comparators.

The embedded memory consists of columns of M4K<sup>12</sup> memory blocks. The memory blocks include input and output registers and can implement various types of memory with or without parity. The multipliers implemented in the FPGA are optimized for multiplier-intensive digital signal processing (DSP) functions and each can work in two different operational modes: one 18-bit multiplier or two independent 9-bit multipliers at up to 250 *MHz*. The FPGA hosted by the PAX\_TB is provided with one column of twenty-six embedded multipliers.

The Cyclone® FPGAs support the Nios® II embedded processor which allows the implementation of custom-fit embedded processing solutions. Single or multiple Nios® II embedded processors can be designed into a Cyclone® II device to provide additional co-processing power or to act as system processors.

---

<sup>11</sup>Taiwan Semiconductor Manufacturing Company, Ltd.

<sup>12</sup>True dual-port memory blocks with 4K-bits of memory plus parity, totally 4608 *bits*.



Figure 4.4: Trigger board GUI.

### 4.1.5 PAX\_TB control software

The trigger board hosts eight inputs dedicated to the collection of the fast trigger signals<sup>13</sup> (TAs) coming from the readout electronic of the STTs<sup>14</sup>, moreover six input dedicated to gate, veto, strobe and clear signals are embedded in the front connection panel (fig.4.1). Beyond the front panel lie the PPGs, the PDLs, the DACs and the programmable devices. As shown in fig.4.5 each of those elements is addressed by a register number, and even the logic gates simulated inside the CPLD are addressed by register numbers.

The PAX\_TB tuning is made through 47 registers composed by more than 90 parameters which makes the setting procedure complicated. For this reason a control software was conceived and written as part of my thesis work. The software is a graphic user interface (GUI) written in C++ and employs the Qt graphic libraries. The purpose of the GUI is to simplify

<sup>13</sup>The readout electronic of the silicon tracking telescopes comprises the VA32TA chips from IDEAS. These chips are composed by two part, one dedicated to the charge collection and the other dedicated to the generation of a fast trigger signal (TA) which is produced whenever a hit is collected from the detector (see §A.3).

<sup>14</sup>Each readout board is assigned to a side of a detector, which means that each detector is served by two readout boards. The PAX\_TB is capable to serve up to four silicon detectors thanks to the eight dedicated inputs which are grouped in pairs, each pair corresponding then to a detector.

the trigger board tuning as well as prevent the user from making mistakes.

In the GUI main window (see fig.4.4a) are grouped four sections addressed to the setting of the channels assigned to the fast trigger signals. Each section allows the tune of the delay and the shape of the TAs which is made respectively via the onboard PDLs and the PPGs. Moreover it is possible to regulate the signals discrimination performed by the onboard DACs and to forbid individually the collection of the TAs which are not needed in the trigger logic. Besides the timing of the signals, these boxes take part in the trigger logic configuration since they allow to select the operation to perform (*And/Or*) between the signals coming from the two sides of a detector. Furthermore each box allows to gate the trigger generated by the PAX\_TB whenever the *master* option on the top of the box is chosen instead of the *enable* option (see fig.4.4a). In the right side of the main window are located five buttons which give access to three more configuration windows (look up table *-LUT-*, auxiliary look up table *-Aux LUT-* and *Advanced Settings*) and to the save file (*Save Configuration*) and read file (*Read Configuration*) windows.

The *LUT* and *Aux LUT* windows (fig.4.4c) are dedicated to the setting of the correspondent look up tables. Each window hosts a  $16 \times 4$  grid of cascade menus each of them provided with 3 options: *ON*, *OFF* and *ANY*. This is the first approach which was conceived<sup>15</sup> in order to allow the most flexible and less error prone look up tables configuration procedure. The modifications made to the cascade menus are stored and even summarized in the right side of the window. The *Advanced Settings* window (fig.4.4b) is assigned to the configuration of the veto, gate, strobe and clear signals and it allows the tuning of some feature of the output trigger signal. This window is intended for experienced users and is not needed in most of the cases.

The values set in the GUI windows undergo the translation process and are then stored in a plain ASCII file, this process is done through the *Save Configuration* window once the name of the file and the path where to store it have been chosen. The translation process has the task to carry out the conversion between the format of the values set by the user and the format of the values needed for the board configuration, that is the register format. The registers are composed of six digits, the first two identifying the related

---

<sup>15</sup>A new GUI version is under development and one of the main features of the new version is a new look up table configuration approach.

device and the remaining four containing the value to be set. Once the file is written, it is used from the **Electronics Message System** (EMS) control software to tune the trigger board.

The EMS is a framework software developed and written by the **Zentralinstitut für Elektronik** (ZEL) of the FZ-Jülich which provides the communication between the control and storage system (i.e. online monitoring) and the experimental apparatus installed inside the COSY ring (i.e. readout modules). I conceived and implemented in the EMS framework the procedures dedicated to the PAX\_TB configuration. These procedures allow both to set manually each trigger board parameter as well as to tune at once the module via the configuration file prepared by the described GUI.

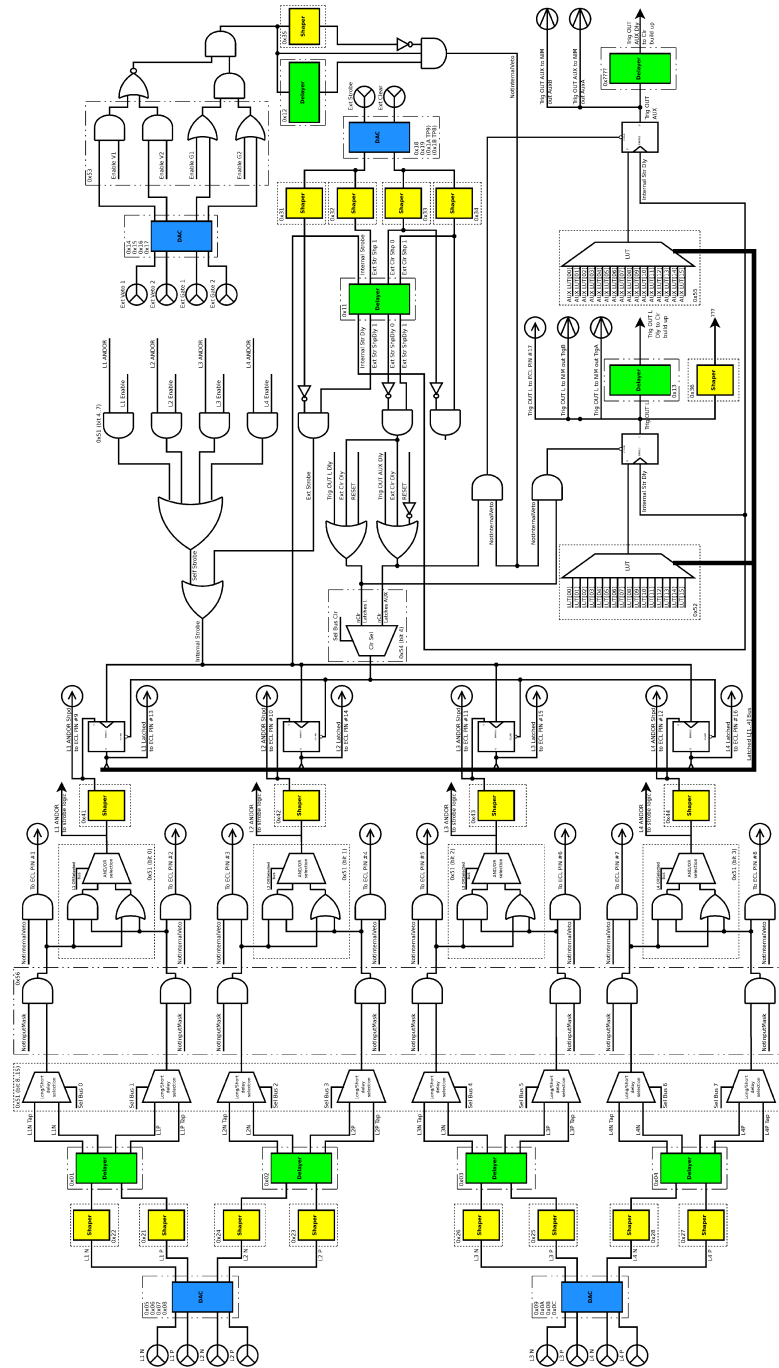


**Figure 4.5:** Logic scheme of the PAX\_TB. The DACs are showed in blu color, the PPGs in yellow and the PDLs in green. All the logic gates presented in this picture are implemented in the CPLD embedded on the trigger board as well as the Look Up Tables. The different kinds of input/output connections are depicted with different symbols in order to separate inputs from outputs and to distinguish between the two kind of outputs (NIM/ECL).

## 4.2 Trigger board commissioning

The PAX\_TB commissioning was carried on in two stages: the first stage consisted in laboratory tests and the second stage in tests performed in the COSY ring DAQ system. The laboratory tests had the aim to characterize the behavior of the programmable pulse generators and of the programmable delay lines implemented on the PAX\_TB and were carried on in two phases: the first phase in which the devices were tested and the second phase in which tests were performed in order to identify possible test bench influences upon the measurements. The laboratory tests led to trigger board improvements which have been afterward implemented.

### 4.2.1 Laboratory: 1<sup>st</sup> phase

At first, the performance of the timing devices embedded in the trigger board (PPGs and PDLs) were probed.

The elements under test were the ones which shape the signals coming from the detection apparatus before they pass through the logic stage which is hosted in the CPLD: in figure 4.5 are shown the shaper (yellow), the delayers (green) and the DACs (blue, which have not been tested).

Aim of the test was the study of the jitter introduced by the programmable PPGs and by the PDLs in order to determine the maximum achievable time resolution. Moreover the *crosstalk*<sup>16</sup> between two signals arriving almost simultaneously (few nanoseconds) to two adjacent inputs was investigated.

In order to perform the measurements a test bench was set up with the following components:

**Strontium (Sr) radiaton source** In order to reproduce similar conditions to the ones in which the trigger board will operate, a Sr radiation source was employed in connection with a scintillator and a photomultiplier to produce real stochastic signals. Assuming that no correlation exists between a produced pulse and the previous or the following ones, a probabilistic method can be applied.

**Discriminator** The discriminator was needed to regulate the wanted working count rate regime. The task of this device was to generate a pulse

---

<sup>16</sup>The crosstalk can be defined as the interference exerted by a signal passing through a line over the adjacent lines.

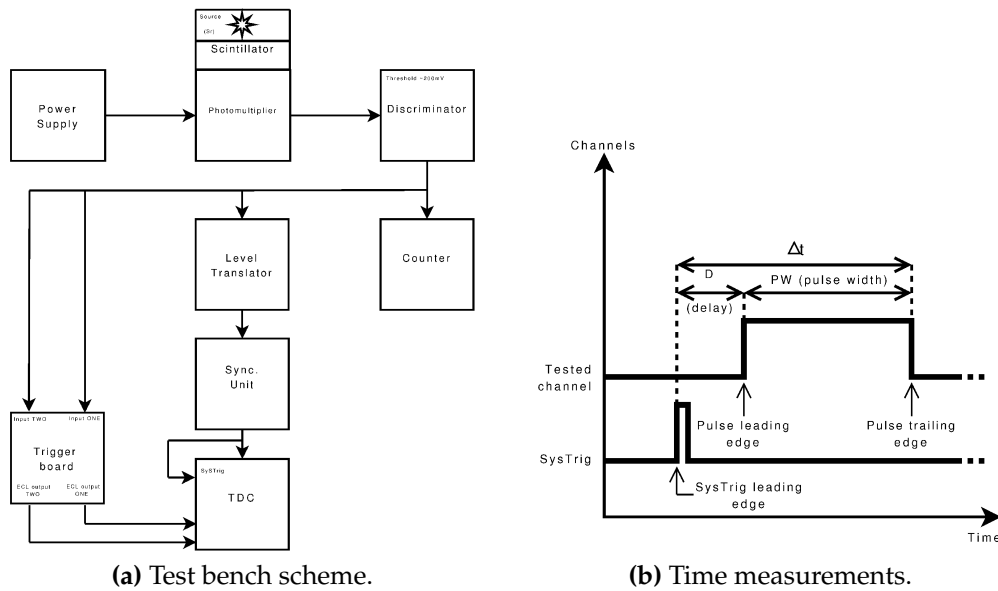


Figure 4.6: Jitter tests setup.

(with a user predefined shape) whenever a signal coming from the photomultiplier exceeded a defined threshold (in this case approximately 200mV). In all the tests a rate of about 2000 counts/sec was maintained as this was expected in the experimental condition. The discriminator signal was provided to four different device inputs (see fig.4.6a and fig.4.10a).

**Level translator (LT)** The level translator was required to convert the signals generated by the discriminator from the NIM levels to the ECL levels needed by the TDC and MSU units.

**Master synchronizing unit (MSU)** The task of the master synchronizing unit was to generate a synchronization signal which triggers the TDC with the signal coming from the discriminator; the synchronization signal was also employed as time reference for our measurements, indeed it was sent even to an input (*SysTrig*) of the TDC in order to include it in the time stamp.

**Time to Digital Converter (TDC)** The TDC was needed in order to perform accurate time measurements. The employed TDC was the GPX TDC produced by the Zentralinstitut für Elektronik (ZEL). It is a 64

channels TDC providing a best time resolution of 0.08ns. The TDC can detect both leading and trailing edges of the pulses sent to its inputs.

When the MSU sends the trigger signal to the TDC the storage process starts and the time distribution of the edges of the pulses is collected referred to an instant  $t = 0$  established by the TDC itself. All the time stamps are referred to  $t = 0$ . Every trigger signal coming from the MCU starts a new storage session resetting the TDC timer to its initial value ( $t = 0$ ). It is important to notice that the *SysTrig* signal does not coincides with  $t = 0$  (see fig.4.7).

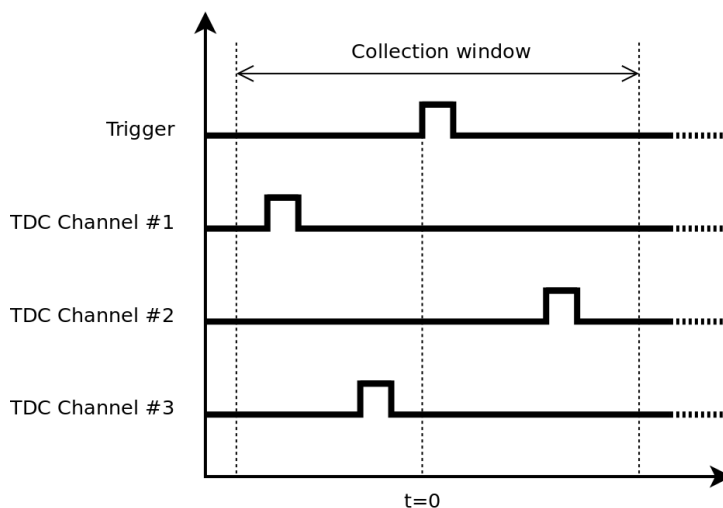


**Figure 4.7:** The TDC runs constantly and records the time position of the signals for a defined time interval (collection window). In case a trigger signal falls in the collection window range, the time positions recorded by the TDC are stored and sent to the DAQ labeled by the trigger signal which started the process. In case no trigger signal comes before the collection window time is elapsed, the recorded data are deleted and a new collection stage begins.

**Trigger board PAX\_TB** The trigger board (fig.4.1) possesses a front connection panel provided with a 34 pins DIN plug connector from which the signals (standard ECL<sup>17</sup> levels) coming from the PPG and PDLs were sent to the TDC without passing through other devices. In

<sup>17</sup>Emitter Coupled Logic

this way the performance of the programmable pulse generators and programmable delay lines were directly tested.

**Data acquisition and analysis** The stage of data collection and elaboration was accomplished through a PC running Kubuntu OS where the ANKE Root Sorter framework was installed. This software allowed the acquisition of the data coming from the TDC and the data sorting and conversion for the final purpose of filling histograms. To sort the data a dedicated analysis code was developed (written in C++) and embedded in the sorter framework.

### 4.2.2 Jitter tests

The timing *jitter* is generally defined as the variation of a measurable quantity of a digital signal from its ideal time position; many factors contribute to random timing jitter including phase noise, spurs (often due to crosstalk and power supply coupling) and thermal noise as well.

The first performed test concerned the measurement of the jitter introduced by the programmable pulse generators, 12-bit programmable devices which can produce pulses widths in a range nominally going from  $0ns$  to  $1023.75ns$  in  $0.25ns$  wide steps.

For the PPGs test the programmed delay value of the digital delay lines was kept fixed ( $D = 12ns$ ) while varying the width of the shaper pulse ( $PW = 13ns$ ,  $PW = 313ns$ ,  $PW = 613ns$ ,  $PW = 913ns$ ). For each step the time position of the leading and trailing edge ( $D$  and  $\Delta t$  respectively) of the generated pulse was measured taking as time reference the time position of the leading edge of the signal *SysTrig* (see fig.4.6). The analysis code performed two different subtractions in order to define the time positions:

$$Pulse_{LE}^A = Pulse_{LE}^R - SysTrig_{LE}^R = D \quad (4.5)$$

$$Pulse_{TE}^A = Pulse_{TE}^R - SysTrig_{LE}^R = \Delta t \quad (4.6)$$

where:

- $LE \rightarrow LeadingEdge$ ;
- $TE \rightarrow TrailingEdge$ ;

- $A \rightarrow Absolute$ ;
- $R \rightarrow Relative$ .

$A$  and  $R$  refer to the time position of the edges of the pulses: *Absolute* is referred to the time position of the leading edge of *SysTrig* and *Relative* is referred to the instant  $t = 0$  of the TDC. The test was performed for two channels of the trigger board (L1N and L2N, fig.4.5).

After the tests of the programmable pulse generators the test of the delay elements was performed. These devices include four separate delay lines, each 4-bit programmable in order to obtain a delay that ranges nominally from  $0ns$  to  $11.25ns$  in  $0.75ns$  wide steps.

In this test the pulse width for the PPGs was kept fixed ( $200ns$ ) while varying the delay value of the PDLs: the range of delay values went from  $19ns$  to  $42ns$  (with two intermediate steps, one at  $27ns$  and another at  $35ns$ ). The time measurements were performed as described above (eq.4.5 and eq.4.6) for the PPGs test.

## Results

The results of the measurements of the jitter introduced by the programmable pulse generators are shown in fig.4.8. The histograms 4.8a, 4.8b, 4.8c and 4.8d represent the distribution of the time position<sup>18</sup> of the trailing edge of the pulse generated by the PPG of the tested line (L1N); here the full width at half maximum (FWHM) is a straightforward representation of the magnitude of the jitter.

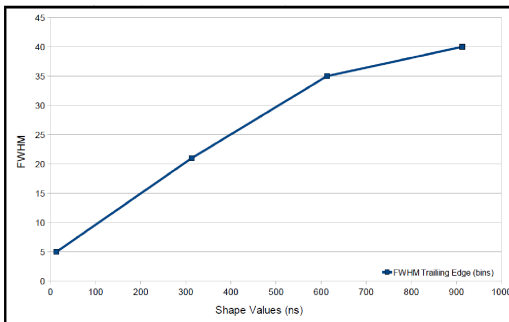
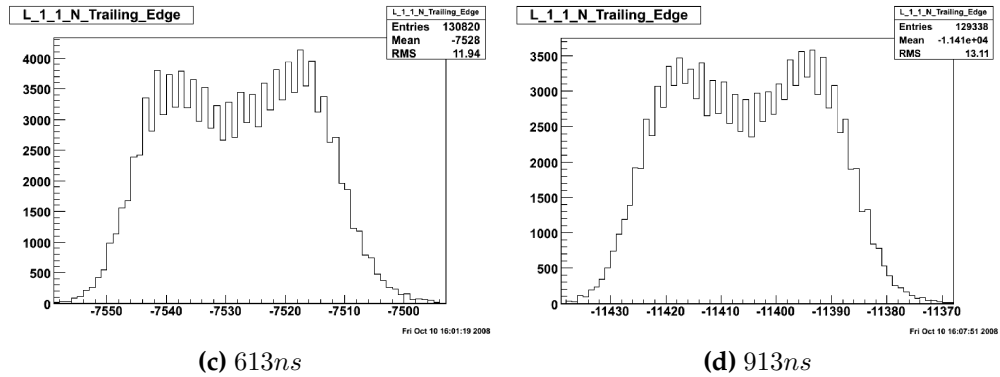
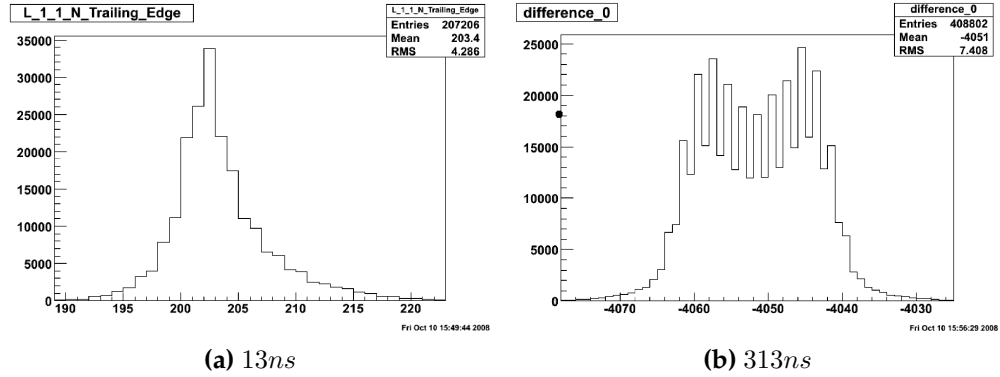
The FWHM of the histograms (fig.4.8e) grows as the programmed width of the pulse grows and reaches values of roughly 40 bins<sup>19</sup>: this means that the value of the jitter affecting the trailing edge is about  $3 \div 4ns$ . In the last two histograms (4.8c and 4.8d) the shapes of the peaks appear to be the sum of at least two gaussian distributions.

Figure 4.9 shows the results of the measurements of the jitter introduced by the programmable delay lines. The histograms are filled in the same way as the previous (fig.4.8), so the FWHM represents the magnitude of the jitter. The value of the jitter remains almost constant (fig.4.9e and it is

<sup>18</sup>As explained before (eq.4.6) the time position of this edge is referred to the time position of the leading edge of the signal *SysTrig*.

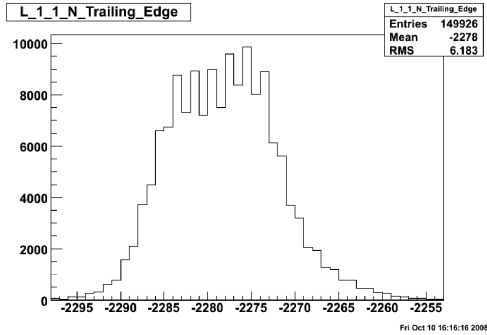
<sup>19</sup>A bin in all the histograms presented and to present corresponds to  $80ps$ .

in agreement with the jitter values expected for the pulse width set by the shapers ( $200ns$ , see the jitter trend fig.4.8e). This is likely due to the small range of delay that the PDLs cover.

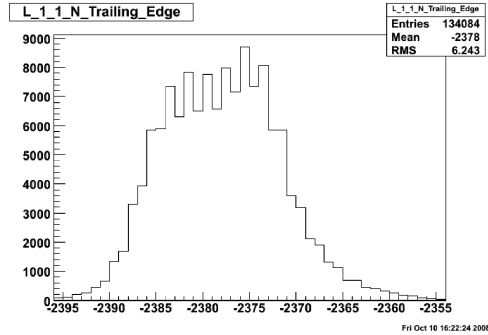


(e) Jitter trend – Here are reported the FWHM of the four previous histograms, the  $y$  axis is represented in *bins of histogram* unit in order to report the width of the distributions.

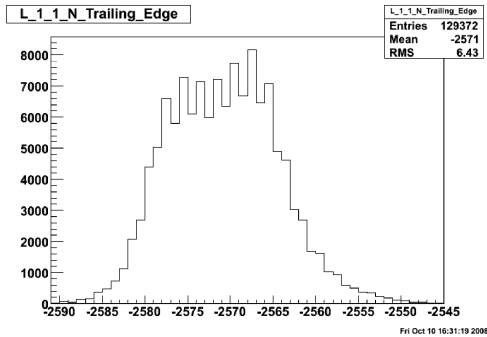
Figure 4.8: L1N trailing edge time distribution – PPGs



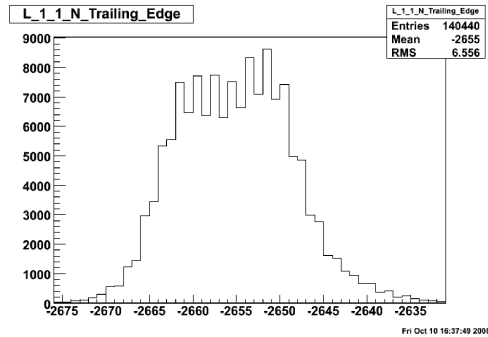
(a) 19ns



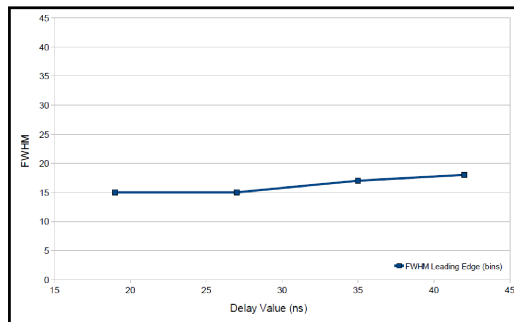
(b) 27ns



(c) 35ns



(d) 42ns



(e) Jitter trend – Here are reported the FWHM of the four previous histograms, the  $y$  axis is represented in *bins of histogram* unit in order to report the width of the distributions.

Figure 4.9: L1N trailing edge time distribution – PDLs

### 4.2.3 Crosstalk test

The crosstalk test was performed by fitting the test bench configuration to the new purposes (fig.4.10a); indeed two channels were employed simultaneously: one channel of the PAX\_TB connected to the discriminator via a fixed delay box (channel tested) and another channel connected to the discriminator via a variable delay box (auxiliary channel). The test was performed twice: the first time the channel L1N was probed employing the channel L1P as auxiliary, and the second time the channel L1N was probed employing the channel L2N as auxiliary.

During the test session the time position (referred to the signal *SysTrig*) of the pulse sent to the tested channel was measured to clarify whether it was influenced by the pulse sent to a near channel for the case of almost simultaneous pulses. Therefore the key role was played by the variable delay box.

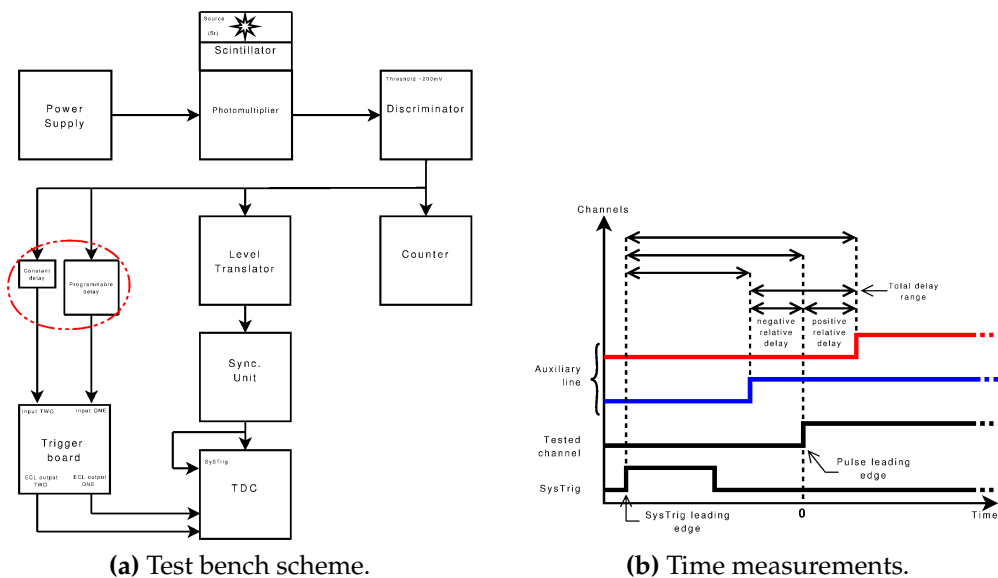


Figure 4.10: Crosstalk tests setup.

The time position of the pulse sent to the tested channel was kept fixed while varying the time position of the pulse sent to the auxiliary channel. The relative delay between the two pulses was calculated taking as time reference the pulse sent to the tested channel. Starting with a relative delay of roughly  $-10ns$  the crosstalk measurements were performed changing

the relative delay in  $1ns$  steps till a relative delay of  $+10ns$  was reached. The analysis code performed the following calculations:

$$Relative\_Delay = TC\_Pulse_{LE}^R - AC\_Pulse_{LE}^R \quad (4.7)$$

$$TC\_Pulse_{LE}^A = TC\_Pulse_{LE}^R - SysTrig_{LE}^R \quad (4.8)$$

where the notations are the same as before and:

- $TC \rightarrow TestedChannel$ ;
- $AC \rightarrow AuxiliaryChannel$ .

## Results

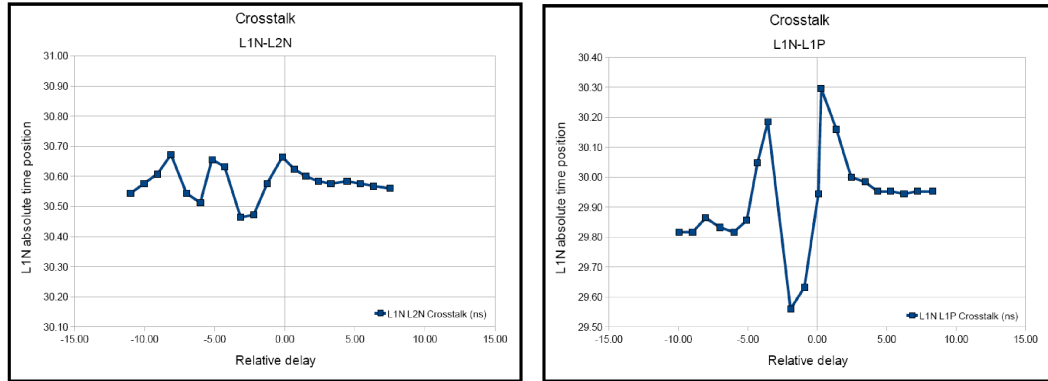
The results of the test about the crosstalk<sup>20</sup> are shown in fig.4.11a and fig.4.11b. In the first set of data collection the tested channel was L1N and the auxiliary channel was L2N (fig.4.11a) whereas in the second set of measurements the role of auxiliary channel was played by L1P (fig.4.11b).

In the first case (fig.4.11a) the time position of the leading edge of the pulse coming to the L1N input ranged from  $30.46ns$  to  $30.67ns$ , that is in a time interval of  $0.21ns$ . In the second case (fig.4.11b) the time position of the leading edge of the pulse coming to the L1N input ranged from  $29.56ns$  to  $30.30ns$ , so the time interval value is  $0.74ns$ . The different influence of the two auxiliary channels over the tested one becomes more clear when the overlap of the results collected in the two stages of the test is taken into account (see fig.4.11c).

The biggest crosstalk effect appeared between the L1N input and the L1P input. The difference between the two input pairs behaviour is explicable looking at the scheme of the trigger board (see fig.4.5): the first pair of inputs share a PDL device, this is likely the reason of the more intense crosstalk measured.

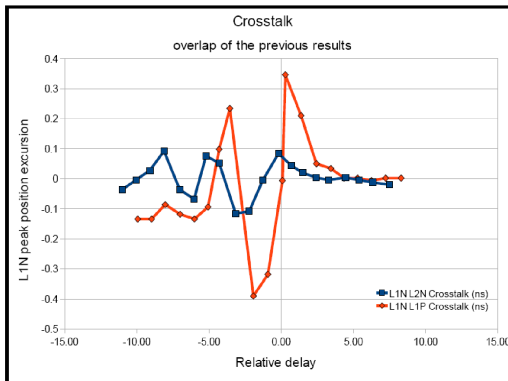
---

<sup>20</sup>For the explanation of the configuration of the system see §4.2.3, fig.4.10a and for the calculations performed see §4.2.3 eq.4.7 and eq.4.8.



(a) L1N/L2N.

(b) L1N/L1P.



(c) Overlap.

Figure 4.11: Crosstalk results

#### 4.2.4 Laboratory: 2<sup>nd</sup> phase

A second set of measurement was carried out to determine whether the influence of the electronic devices which constitute the test bench could affect the PPGs and PDLs test.

The test performed in the first phase were then repeated in order to probe the test bench performances.

In the next sections the modifications made at the test bench will be described along with their purposes.

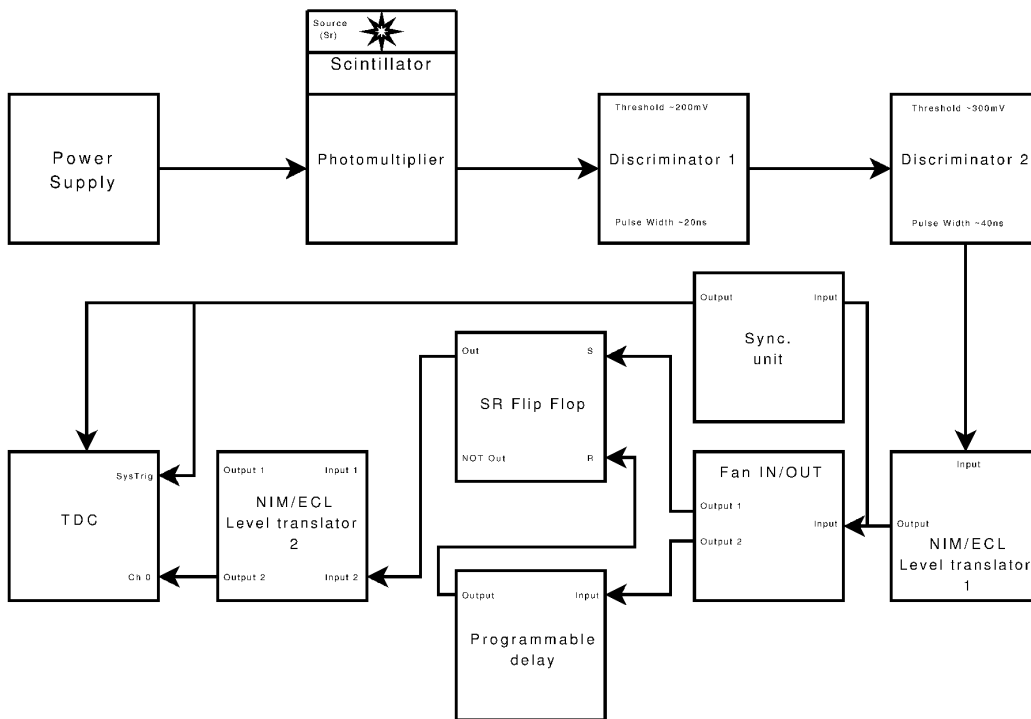


Figure 4.12: Test bench scheme – Jitter tests.

### Set/Reset Flip-Flop

The devices that could give origin to a jitter were the trigger board and the TDC. No knowledge about the used TDC existed as no test about the TDC performance had been made.

A pulse generator of well-known characteristics was needed: the pulse generator had to generate a pulse with extremely stable edges<sup>21</sup>, that is the jitter of the edge of the pulse had to be fixed at a well known and possibly small value while the width of the pulse increased. Therefore the task was to find out such a pulse generator or to realize it. The pulse generator was arranged combining cables (which provided fixed delay) and a "Set/Reset Flip-Flop".

The behavior of the *S/R Flip – Flop* is schemed in figure 4.13. This element is the simplest, asynchronous memory unit. Its main features are to maintain its outputs ( $q$  and  $\bar{q}$ ) fixed when its inputs are low and to switch its outputs when one (and only one) of its input goes high<sup>22</sup> (see its truth table fig.4.13c). The *S/R Flip – Flop* changes the state of its outputs in correspondence with the leading edges of the pulses (see fig.4.13b). If both the inputs S and R are high, the state of the *S/R Flip – Flop* is not predictable.

During the test, the signal coming from the first level translator was sent to a *fan IN/OUT* device to reproduce it over many outputs, then one of those outputs was connected directly to the S-input of the *S/R Flip – Flop* while another was sent to a variable delay box (realized with cables) and after to the R-input of the *S/R Flip – Flop* (fig.4.19).

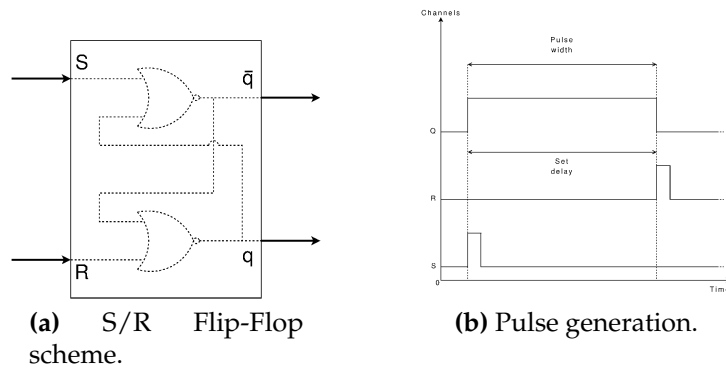
In this configuration (fig.4.12) the *S/R Flip – Flop* produced a pulse of stable width: when the first pulse reached the S-input, the  $q$ -output went high and remained in that status until the second pulse reached the R-input (carrying a delay set by the cable delay box) and the  $q$ -output went low. Therefore the width of the pulse produced was supposed to be exactly of the same value of the delay set by the dedicated box.

In this way a stable pulse generator was realized, affected by minor jitter effect. The width of the generated pulse depended only on the delay introduced by the cable delay box. One of the most likely sources of jitter in that case was the signal loss along the cables (see fig.4.14).

---

<sup>21</sup>Regarding their timing.

<sup>22</sup>Accordingly to the status of its outputs.



(a) S/R Flip-Flop scheme.

(b) Pulse generation.

*Truth table*

<i>S</i>	<i>R</i>	<i>q</i>	<i>q̄</i>
0	0	<i>q</i>	<i>q̄</i>
0	1	0	1
1	0	1	0
1	1	<i>Undefined</i>	

(c) Truth table.

**Figure 4.13:** S/R Flip-Flop.

The pulse that had to pass through the delay box had to cover longer distance with respect to the distance covered by the pulse which went straightforward from the *fan IN/OUT* to the *S/R Flip – Flop* and the shape of the first pulse was more prone to worsening (see fig.4.14b) than the second (see fig.4.14a). In figure 4.14b one of the most likely jitter causes is described.

The jitter effects introduced by the pulse generator were supposed to be of minor significance because the shape of the pulses was supposed to be as close as possible to the ideal case and the *S/R Flip – Flop* performance as well. The data acquisition was implemented employing the apparatus described in §4.2.1.

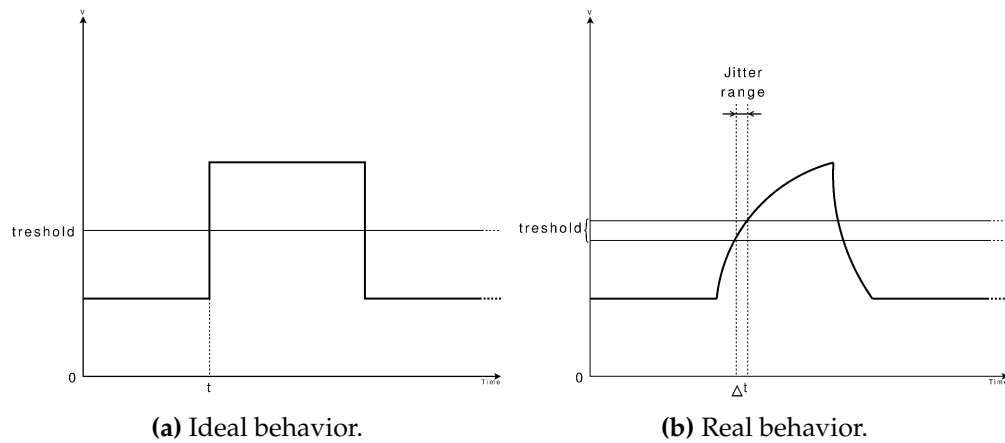


**Figure 4.14:** Flip-Flop jitter. One of the best way to generate a pulse which is almost not affected by jitter is to employ an S/R Flip-Flop and cables of different length, but there are aspects which must be taken into account. The rising slope of a real pulse edge (b) combined with the measurable amplitude of the Flip-Flop activation threshold (which in the ideal case is supposed to be a line and have no thickness (a)), is one of the jitter causes. The sum of these two effects results in the definition of a time interval in which the Flip-Flop set (reset) process can occur (b). This is the reason why the time position of the edges of the pulse generated by the Flip-Flop is affected by a sort of uncertainty.

### 4.2.5 Jitter tests

The test was carried on to clarify whether the TDC was one of the jitter sources in the data collection. The TDC channel zero (*Ch0*) was tested because it was the one employed in the former phase to test the trigger board channel L1N (fig.4.5). The measurements were repeated with four distinct pulse width values ( $30ns$ ,  $100ns$ ,  $200ns$  and  $300ns$ ). The channels one and two (*Ch1* and *Ch2*) were probed as well. The time position of the trailing edge of the pulse was evaluated by the dedicated analysis code employed in the previous phase.

### Results

The results of the jitter test are shown in figures 4.15, 4.16 and 4.17. The time distributions of the trailing edges of the pulses of various width generated by the *S/R Flip – Flop* over the three channels tested, *Ch0*, *Ch1* and *Ch2*

are visible in figures from 4.15a to 4.15d and from 4.16a to 4.17d. It is clear (see fig.4.15e, fig.4.16e and fig.4.17e that the jitter was not introduced by the devices which composed the test bench. Indeed from the charts of the trend it appears that the jitter was almost constant and maintained a value of  $3 \div 4$  bins<sup>23</sup>; Therefore the jitter was generated by the elements of the trigger board.

---

<sup>23</sup>Remember that the value of a bin is  $0.08ns$ .

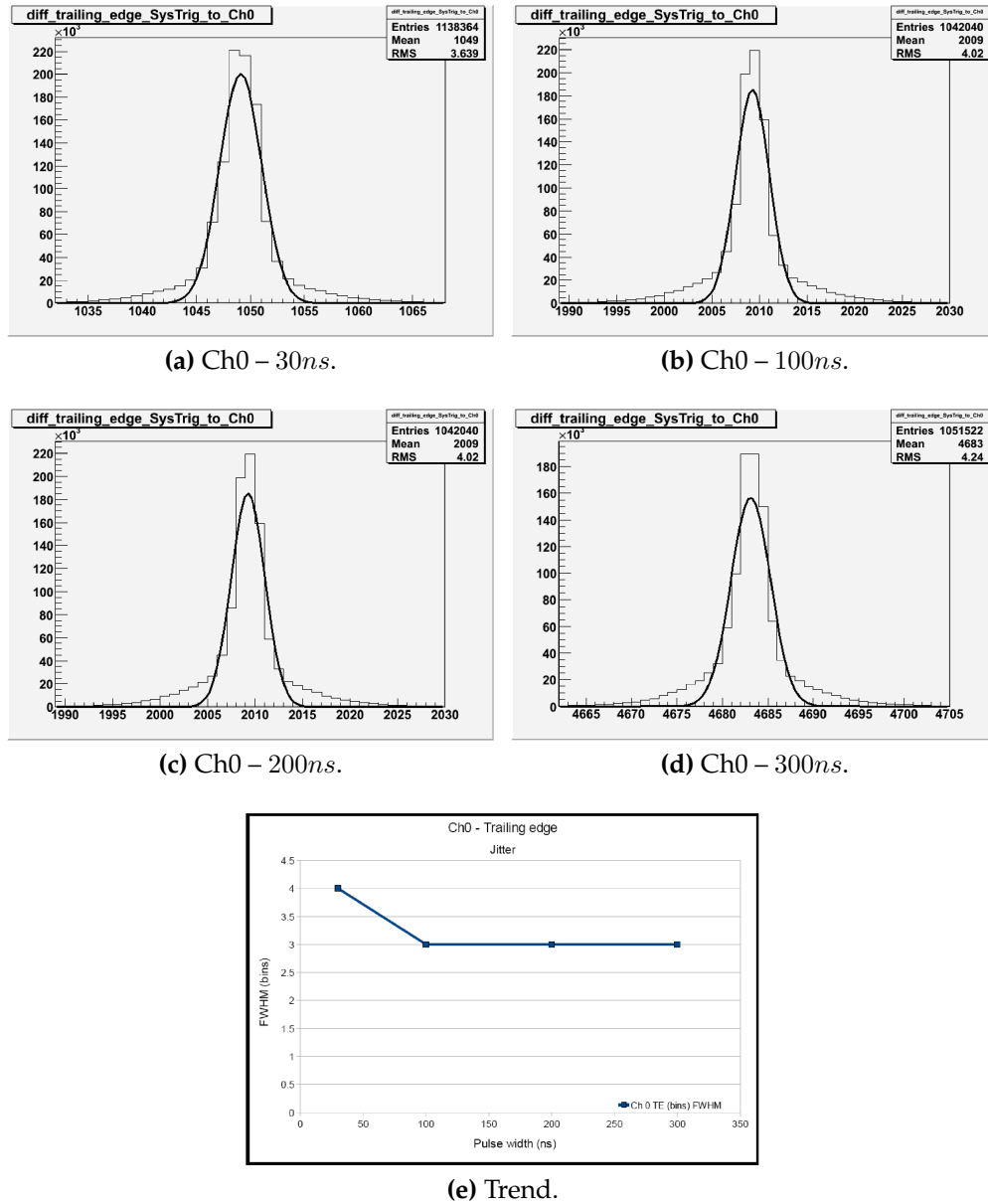
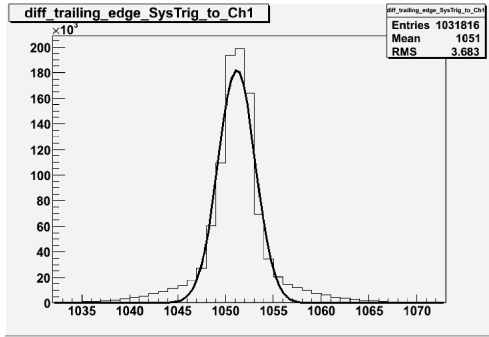
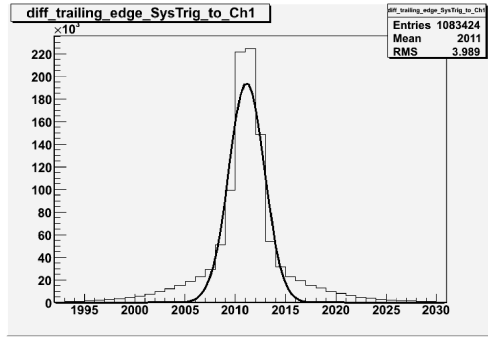


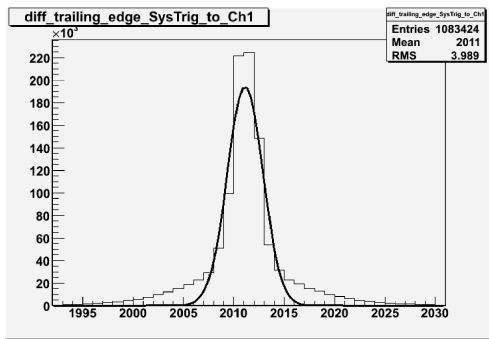
Figure 4.15: Trailing edge time distribution – Ch0



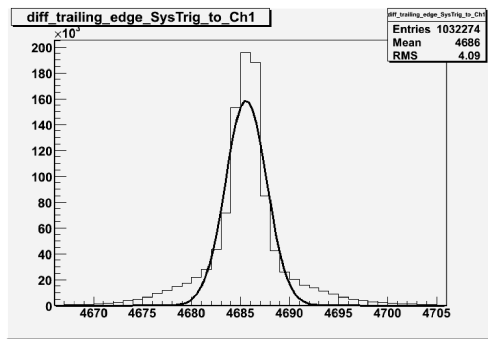
(a) Ch1 – 30ns.



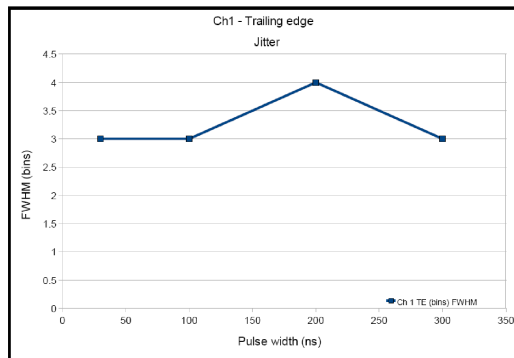
(b) Ch1 – 100ns.



(c) Ch1 – 200ns.

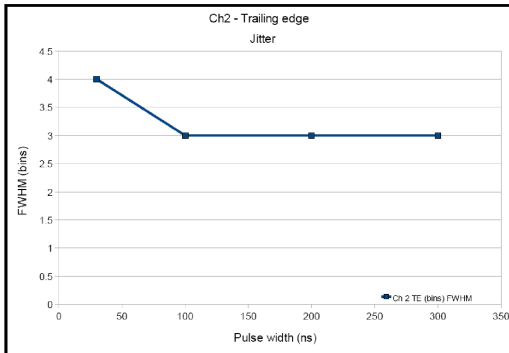
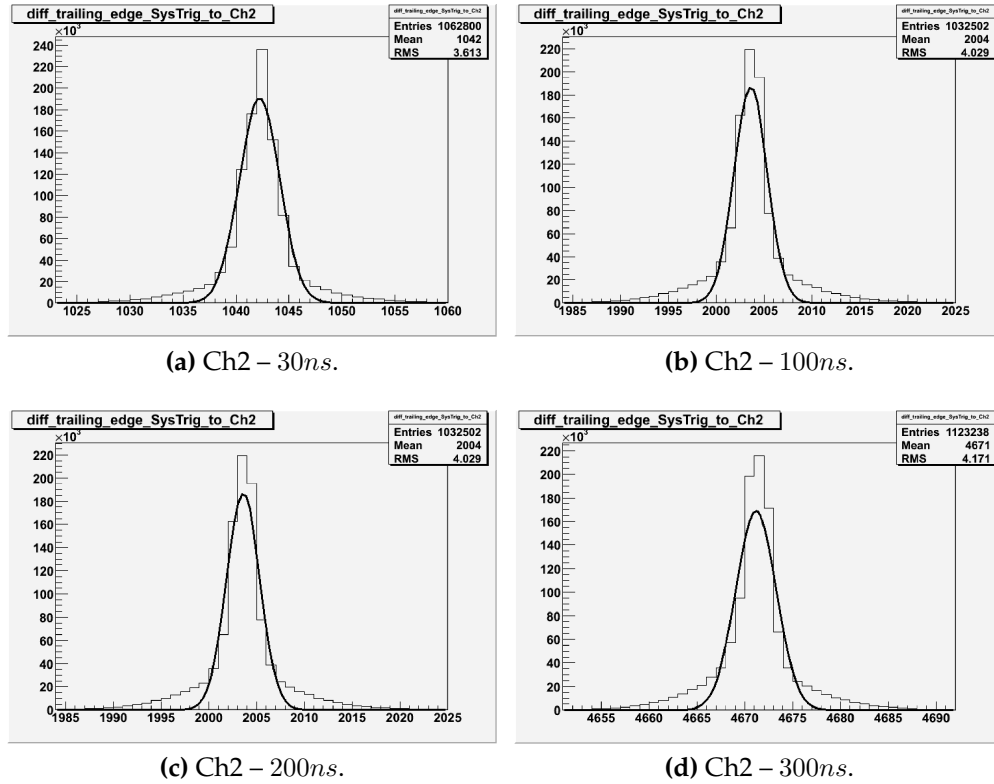


(d) Ch1 – 300ns.



(e) Trend.

Figure 4.16: Trailing edge time distribution – Ch1.



(e) Trend.

Figure 4.17: Trailing edge time distribution – Ch1 &amp; Ch2.

### 4.2.6 Crosstalk tests

The crosstalk effect could have affected the TDC and the level translator (LT). This is why two sessions of data collection<sup>24</sup> were performed: one that included both the TDC and the level translator (see fig.4.19) and one that concerned only the TDC (see fig.4.18). *Ch0* was the tested channel and *Ch1*

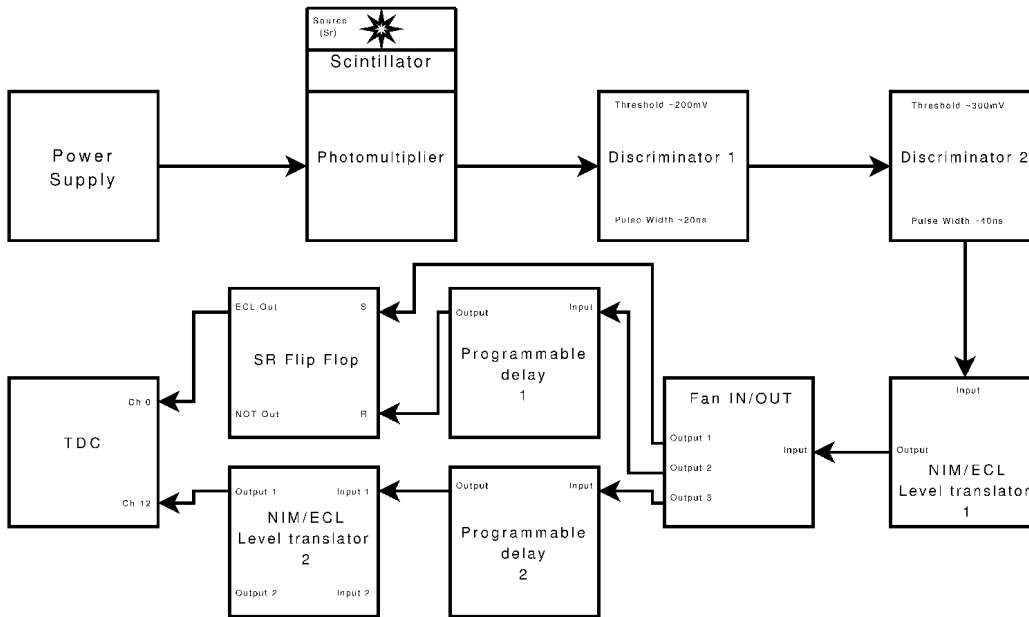


Figure 4.18: Test bench scheme – Crosstalk tests tdc.

and *Ch2* were the auxiliary lines (see fig.4.10b). The relative delay between the leading edge of the pulse that arrives on *Ch0* and the leading edge of the pulse that went on *Ch1* (or *Ch2*) were calculated by the dedicated code (eq.4.7). It is important to underline once more that here the signal *SysTrig* was not employed, which means that the time position of the leading edge of the pulse on *Ch0* was referred to the  $t = 0$  set by the TDC.

The above description is valid both for the test regarding only the TDC and the test including also the LT.

<sup>24</sup>in both the sections the *SysTrig* signal has been excluded because during this stage only relative values are relevant

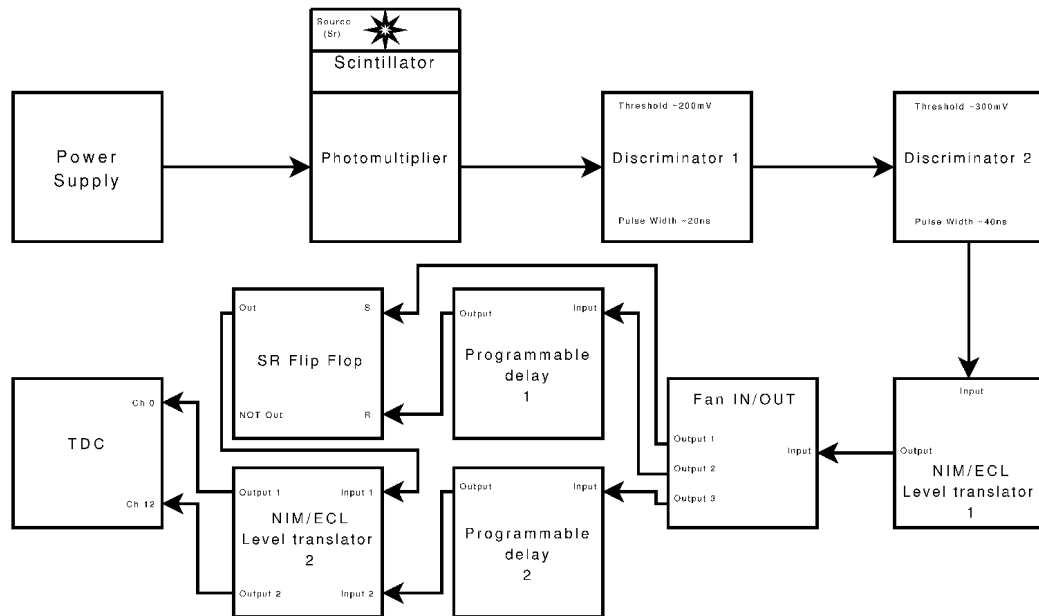


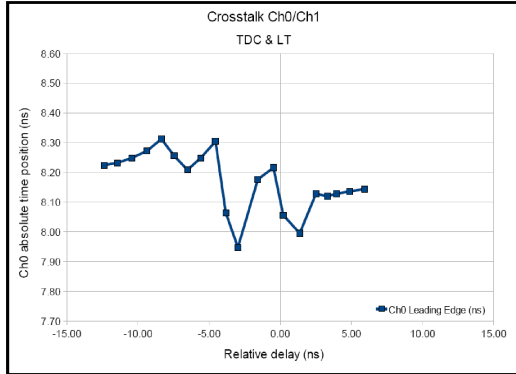
Figure 4.19: Test bench scheme – Crosstalk tests.

## Results

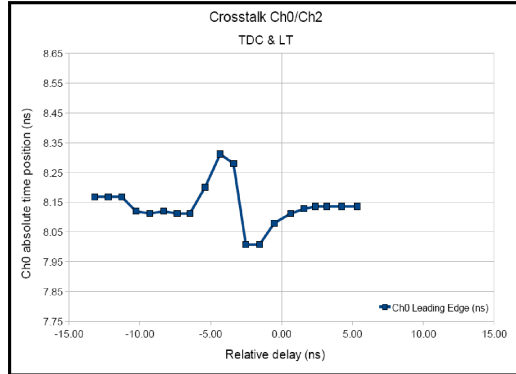
The test about the crosstalk produced the results shown in fig.4.20. The figures 4.20a and 4.20c are relative to the measure of the crosstalk between *Ch0* and *Ch1*, while the figures 4.20a and 4.20d are relative to the measure of the crosstalk between *Ch0* and *Ch2*.

A comparison between the results obtained from the set of measurements performed in the first phase (see fig.4.11a and fig.4.11b) and the results produced by the second phase of test is reported in figures 4.20c, 4.20d, 4.20a and 4.20b.

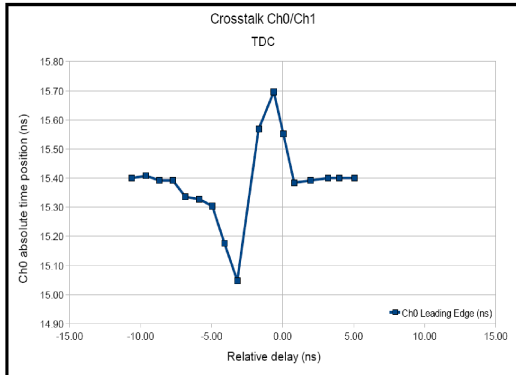
In fig.4.20e is presented the overlap of the results of the crosstalk test for *Ch0/Ch1* and in fig.4.20f is presented the overlap of the results of the of crosstalk test for *Ch0/Ch2*. From what showed by the charts it is not clear which was the major crosstalk source and it is not possible to disentangle the contribution of the single devices.



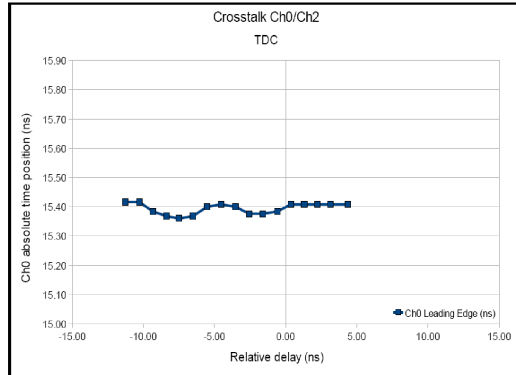
(a) TDC & LT – Ch0/Ch1.



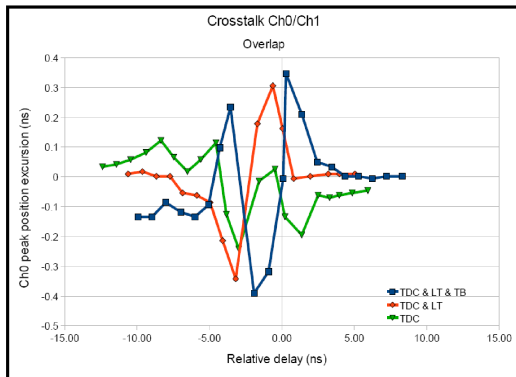
(b) TDC & LT – Ch0/Ch2.



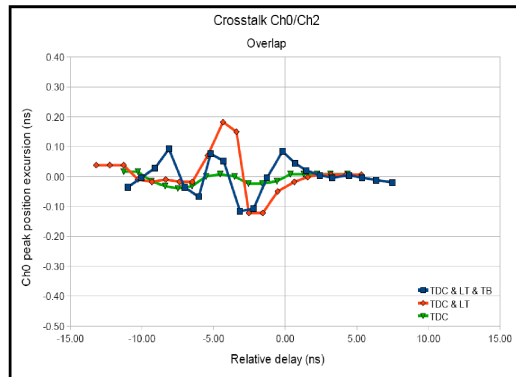
(c) TDC – Ch0/Ch1.



(d) TDC – Ch0/Ch2.



(e) Overlap – Ch0/Ch1.



(f) Overlap – Ch0/Ch2.

Figure 4.20: Crosstalk results.

### 4.2.7 Laboratory tests conclusions

The test performed highlighted many aspects:

- the jitter was mainly introduced by the PPGs whereas the contribution of the delayers did not appear from the collected results. However, while working in the time interval where the PPGs are expected to work during the experiments, the jitter laid within the range established by the realization constraints ( $5\text{ ns}$ ).
- the crosstalk effect resulted from the sum of many elements which were not completely disentangled. Anyway it can be considered a minor effect and it will not need further investigations.

The evidences collected about the jitter effect led to further investigation of the jitter causes. The INFN electronic workshop found that one of the main causes of the jitter was the power supply of the shapers. For this reason dedicated filters were applied to the supply lines and the test performed after that modification showed a good improvement: the jitter was reduced approximately by an order of magnitude [62].

### 4.2.8 Final commissioning

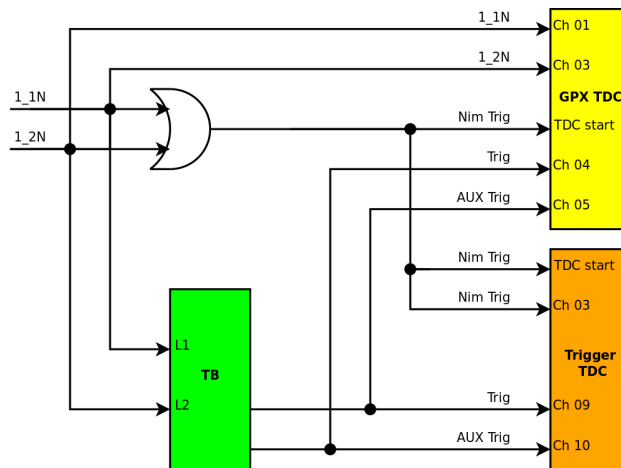


Figure 4.21: STTs trigger apparatus scheme.

To compare the performance of the new trigger board and of the presently employed STTs NIM-based trigger system implemented in the COSY ring, the PAX\_TB was embedded in the DAQ system in order to have both the trigger apparatuses work in parallel under the same conditions during the October 2010 PAX beam time. The STTs trigger was generated by a simple logic operation between the TAs, it was produced whenever a particle hit either the negative side of the first detector or the negative side of the second detector (fig.4.22, in fig.4.21 the logic operation is shown by the *OR* gate connected to the lines  $1_{1N}$  and  $1_{2N}$ ). The TA lines were also connected to the correspondent PAX\_TB inputs and to a pair of TDCs, to which were also connected the outputs of both the trigger apparatuses.

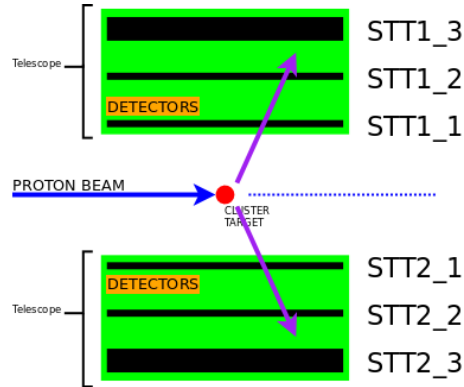


Figure 4.22: Silicon tracking telescopes setup scheme.

In this stage the onboard timing devices were not under examination whereas the look up tables (LUT, AuxLUT) and the logic features of the PAX\_TB were probed. The logic of the STTs NIM trigger system was unchanged during the whole beam time (see fig.4.21) and the first look up table of the trigger board was configured reproducing the same logic scheme, to have a straight feedback from the PAX\_TB. What did change throughout the test phases were the AuxLUT settings and the *master channel* (see fig.4.4a) settings.

The *master channel* selection is an option embedded in the trigger board logic which allows the TAs signals coming from the STTs readout to gate the PAX\_TB trigger output, when one or more channels are selected as *master*. This variable affects the trigger logic significantly and its influence is expected to be clearly visible in the trigger distribution histograms similarly

to the effects of different look up table settings.

Phase	Look Up Table	AUX Look Up Table	Master Channel
<i>First</i>	$L1 \text{ or } L2$	$L1 \text{ and } L2$	$L1$
<i>Second</i>	$L1 \text{ or } L2$	$\bar{L1} \text{ and } L2$	$L2$
<i>Third</i>	$L1 \text{ or } L2$	$L1 \text{ and } L2$	$L1 + L2$

**Table 4.1:** Test phases settings.

The test was carried on in three different phases summarized in table 4.1. In the first phase the settings of the AuxLUT were aimed to disentangle the contribution of the first detector (L1) to the trigger generation, while in the second phase the same was done for the second detector (L2). Indeed in the first set of measurements the AuxLUT generated a trigger signal when a particle hit the first layer (L1) and only it (anticoincidence with the second detector  $\neg L2$ ); L1 was also chosen as *master*. In the second set of measurements L2 was chosen as *master* and tested as formerly done for L1. In the third phase both L1 and L2 were selected as *master* and the AuxLUT was set to generate a trigger signal whenever a particle hit both the detectors; that was supposed to check the effect of the *master channel* selection on the look up tables triggers histogram distributions.

## Results

Comparing the number of entries of histograms fig.4.23a and fig.4.23c and considering the trigger condition of the first phase (tab.4.1) it is evident that the L1 detector gave the major contribution to the trigger generation (almost 96%) since the L1 detector was the only one enabled to gate the trigger generation of the PAX\_TB. Comparing fig.4.23c and fig.4.23e it is visible the different shape of the tails. This is due to the fact that in the histogram in fig.4.23e are isolated the trigger signals generated when a particle hits only the detector L1 while in the histogram fig.4.23c are taken into account also the events in which a particle hits both the detectors L1 and L2. The reason for the tail is visible only in the fig.4.23c and fig.4.23e histograms and not in fig.4.23a is that the TDCs to which the trigger board and the NIM trigger system were connected was synchronized by the NIM trigger system itself. However the **Full Width Half Maximum (FWHM)** of the peaks of fig.4.23d and fig.4.23f are comparable to the FWHM of the peak of fig.4.23b.

Looking at the results of the second phase of the test the most emphasized aspect is the huge difference in the amount of triggers generated by the NIM system with respect to the triggers generated by the trigger board, which is shown by the number of entries of the histogram of figures 4.24a and 4.24c. This effect was due to the trigger board settings in this phase (see tab.4.1), at that time indeed the detector L2 was responsible of the PAX\_TB trigger gating process and the explanation of the lower count can be found looking at the fig.4.22. The layer L2 was installed behind the L1 layer and so the number of particles which hit L2 is lower than the number of particles which hit the first detector. Looking at the shape of the distribution peaks of figures 4.24d and 4.24f there are few aspects to remark: the first is that the FWHM of the shown peaks is still comparable with the FWHM of the peak of the distribution of the NIM triggers shown in fig.4.24b. The second aspect to notice is the double peak of fig.4.24d, which also in this case is to ascribe both to the fact that the TDCs were synchronized by the NIM trigger signals and to the fact that the detector L2 was set as master. Indeed this last condition, combined to the first look up table settings, gives a reasonable answer: the LUT generated a trigger whenever a particle hit one of the detector but the trigger was gated only when the second detector was hit. This means that the histogram of fig.4.24d shows the events generated by L2 only and by L1+L2, which is likely the reason of the two peaks production. This assumption is supported also by the fact that the histogram of fig.4.24f shows no double peak. Accordingly to the AuxLUT settings in fig.4.24f are reported the events generated by particles which hit L2 and only L2 (anticoincidence with L1) and were gated by the detector L2.

In the third phase the results are a check of the performance of the PAX\_TB: comparing the amount of entries in the histogram of the NIM trigger system (fig.4.25a) to the amount of entries in the histogram of the trigger board first look up table<sup>25</sup> (fig.4.25c) it is visible that they are almost equal (the efficiency of the PAX\_TB over the NIM system is about the 99.8%). Taking into account the LUT results and considering that the only difference with the previous stages was that in the third stage both L1 and L2 could gate the trigger signals, it is very likely that this was the reason why the efficiency improved with respect to the first phase. From fig.4.25c is also visible a drastic reduction of the distribution tail to be ascribed to the

---

<sup>25</sup>The first LUT is the one configured replicating the NIM trigger logic.

*master* settings. In fig.4.25e are reported only the events in which a particle hit both L1 and L2, this was the reason of the extremely low amount of entries. In fig.4.25d fig.4.25f are visible the distribution characterized by the two peaks structure which have already been explained. To notice that the position of the two peaks of fig.4.25f are respectively the same position of the peaks of fig.4.23f and fig.4.24f. As for the previous phases, also in this last case the FWHM of the peaks of the fig.4.25d fig.4.25f are comparable with the FWHM of the peak of fig.4.25b.

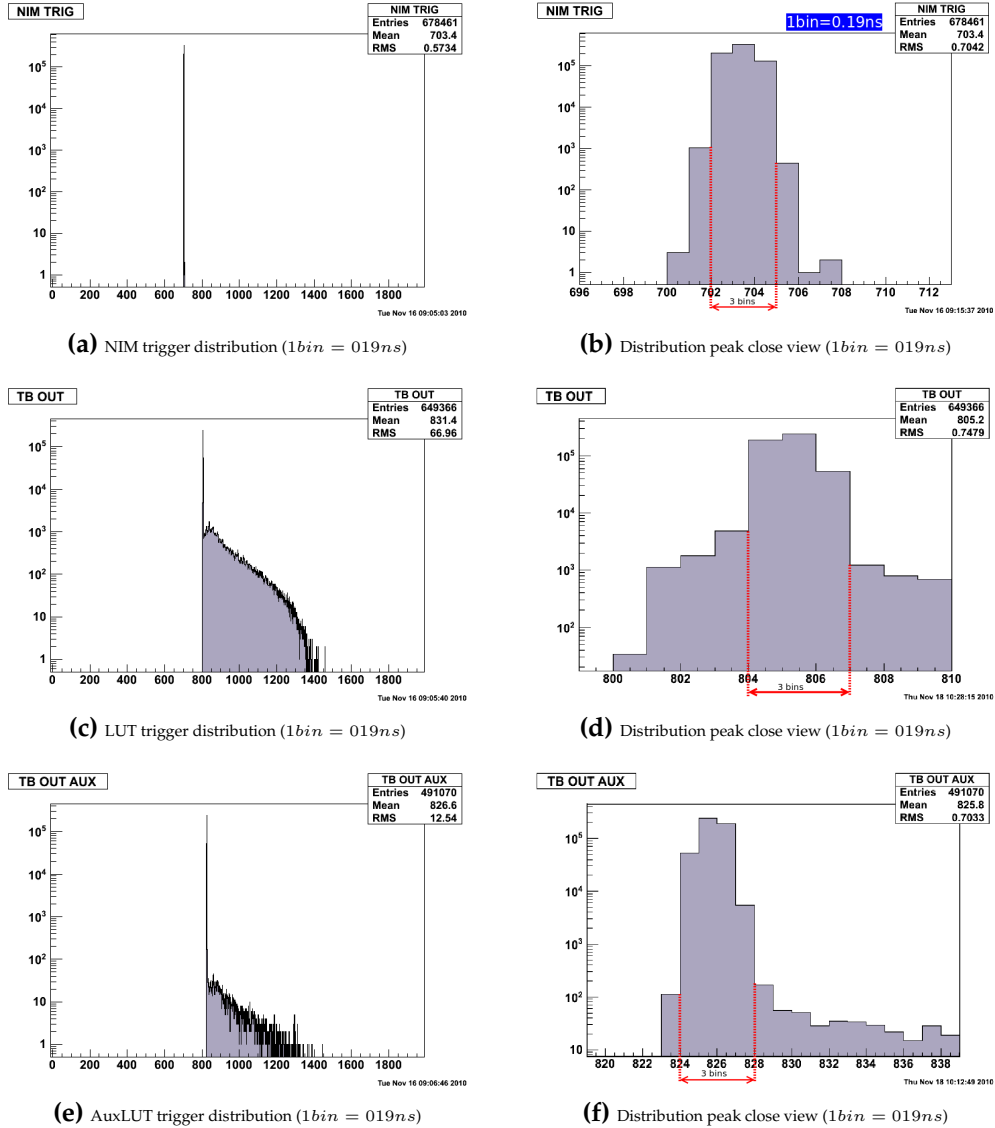


**Figure 4.23:** First phase: the distribution patterns of the look up tables histograms are influenced by the fact that only the L1 channel could gate the trigger output. The difference between the (c) and (e) histograms is that the first is filled by ( $L1$  or  $L2$ ) events while the second is filled by ( $L1$  and  $\bar{L2}$ ) events. The narrow peak of the (a) histogram and the absence of the tail is due to the fact that the NIM trigger is the signal which triggers the TDCs data acquisition. Anyway the width of the peaks of the (d) and (f) histograms is comparable to the width of the peak of the (b) histogram.

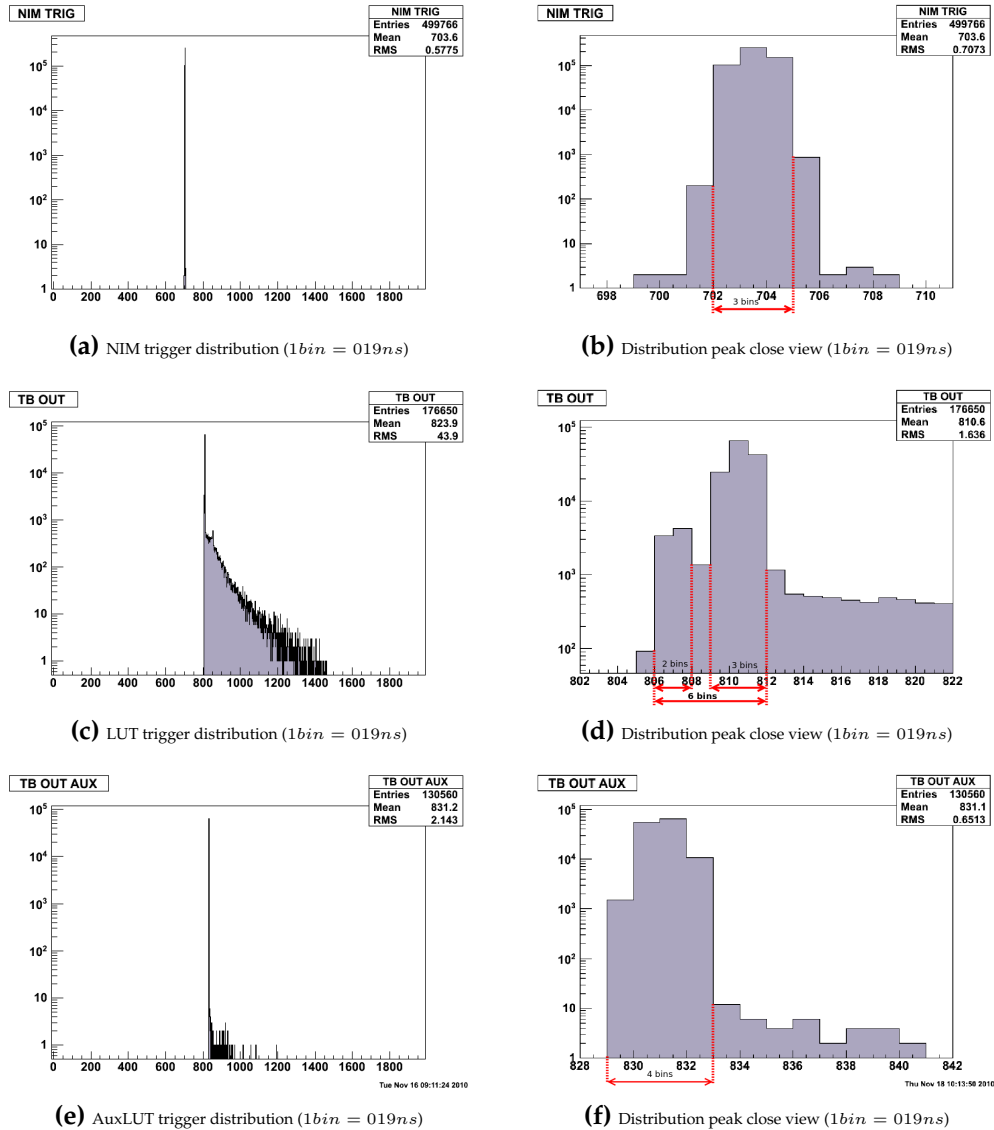


**Figure 4.24:** Second phase: the distribution patterns of the look up tables histograms are influenced by the fact that only the L2 channel could gate the trigger output. The difference between the (c) and (e) histograms is that the first is filled by ( $L1$  or  $L2$ ) events while the second is filled by ( $\bar{L1}$  and  $L2$ ) events. The presence of a double peak in the (d) histogram could be due to the master channel choice, this is supported by the fact that the (f) histogram has only one peak. Also in this case the width of the peaks of the (d) and (f) histograms is comparable to the width of the peak of the (b) histogram.

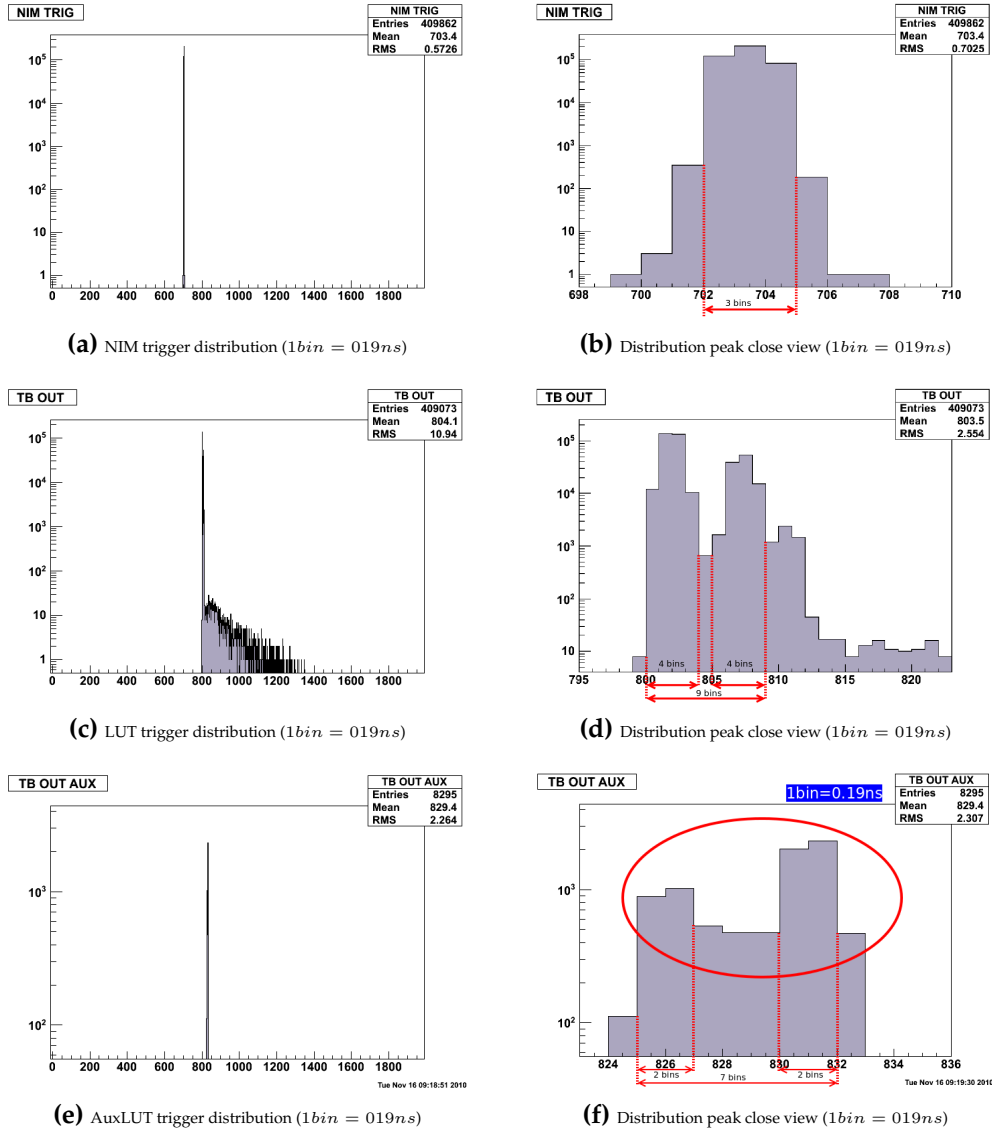


**Figure 4.25:** Third phase: the distribution patterns of the look up tables histograms are influenced by the fact that both L1 and L2 channels could gate the trigger output. The difference between the (c) and (e) histograms is that the first is filled by (*L1 or L2*) events while the second is filled by (*L1 and L2*) events, extremely rare coincidences if compared to the number of event generated by the NIM apparatus. Even in this case the presence of a double peak in the (d) histogram could be due to the master channel choice. The (f) histogram shows two peaks too and a closer look at the histogram (4.23f) and (4.24f) reveals that this two peaks are in the same position of those single peaks. Also in this case the width of the peaks of the (d) and (f) histograms is comparable to the width of the peak of the (b) histogram.

### Conclusions

The PAX\_TB performed as expected. The data collected in each phase prove the reliability of the trigger board. Despite the fact of the distribution tails visible in the histograms (which anyway have already been explained), the sharpness of the peaks confirm the quality of the performances of this new onboard trigger system. Moreover for each modification made to the trigger logic, the results obtained were completely understandable. It was understood that the *master channel* option plays a main role in the trigger generation process and this must be taken into account whenever working without external gating signals.

The PAX\_TB performance are under any aspect comparable to the NIM trigger system performance, this allows to say that the board is commissioned and ready to substitute the present old apparatus.

# Conclusions

The PhD thesis work was performed inside the PAX Collaboration, that has proposed a physics program involving a polarized antiproton-polarized proton collider at the FAIR facility in Darmstadt, Germany.

In the period when my PhD work was developed, the Collaboration has focused its attention to the study of the mechanism for producing the polarized antiproton beam, namely spin-filtering. For this reason, a technical proposal has been submitted to the CERN SPS Committee to study the spin-dependence of the proton-antiproton interaction. Following the recommendation of the Committee, a spin-filtering experiment with protons has been prepared and finally realized in 2011 at the COSY ring in Jülich. Aims of the spin-filtering experiments at COSY performed by the PAX Collaboration were two. The first was to confirm the present understanding of the spin filtering processes in storage rings by determining the spin-dependent total cross sections in  $p p$  scattering, and the second was the commissioning of the experimental setup, which will be used for the experiments with the antiprotons.

The major part of my PhD work consisted in the development and commissioning of a new trigger board to be implemented in the Data Acquisition System (DAQ) of the experiment. The motivation for the project was the replacement of the existing old-fashioned trigger system based on NIM logic modules, with a modern system based on FPGA programmable chips. This, also in perspective of the more complex detection system that the Collaboration is planning to realize for the future experimental activity. During my PhD activity I was supported by a dedicated grant from the Electronic Workshop of the Forschungszentrum-Jülich (ZEL) and I spend most of my research time in Jülich.

The trigger board was designed and realized by the electronic workshop of the University of Ferrara and INFN of Ferrara. My first task was to

write the control-software of the board. After that I performed a series of commissioning tests divided into two stage: the first stage took place in the laboratory and was intended to verify the performance of the single electronic components embedded; the second consisted in the implementation of the board in the DAQ of the COSY ring to test the board behaviour under real experimental conditions. The laboratory stage, allowed to identify some weak points in the board and to improve its performance as shown in section §4.2.7. During the test on the COSY ring, the board showed no difference in performance with the existing system, as shown in section §4.2.8. This test represented the necessary demonstration to proceed with the replacement of the old system which will be accomplished in the coming months.

# Appendix A

## Detectors

As already mentioned in §3.3.6, the elastic events produced by the  $p d$  interaction in the cluster target are revealed by the STTs which comprises three detector layers. Each detector is a double-sided silicon-strip detector, the three layers differ for the individual thickness.

### A.1 Thin detectors ( $69 \mu m$ , $300 \mu m$ )

The thin detectors have been originally designed for the BaBar experiment at the SLAC PEP-II B factory by the British company Micron Ltd., they are named BaBar IV detectors. They have been chosen because of their active area which fits with the ANKE telescopes requirements and because the reuse of already existing production facilities and masks makes the production process easier, faster and cheaper.

This kind of detector can be produced in a thickness range that goes from  $69 \mu m$  to  $500 \mu m$ . On the positively doped side (p-side) the detector hosts 1023 strips while on the negatively doped side (n-side) there are 631 strips which are all capacitively coupled to the bond pads used to connect the strips to the readout electronics. In order to provide AC-coupling to the strips on both the detector sides an additional mask is vacuum metallized.

In the detector build up process is employed a rather complicated connection scheme in order to achieve a strip pitch value of about  $400 \mu m$ . The scheme used for the p-side and n-side connections is shown in figure A.1. In the upper part the p-side scheme is represented in order to show how all the strips are grouped four by four, exception made for the first

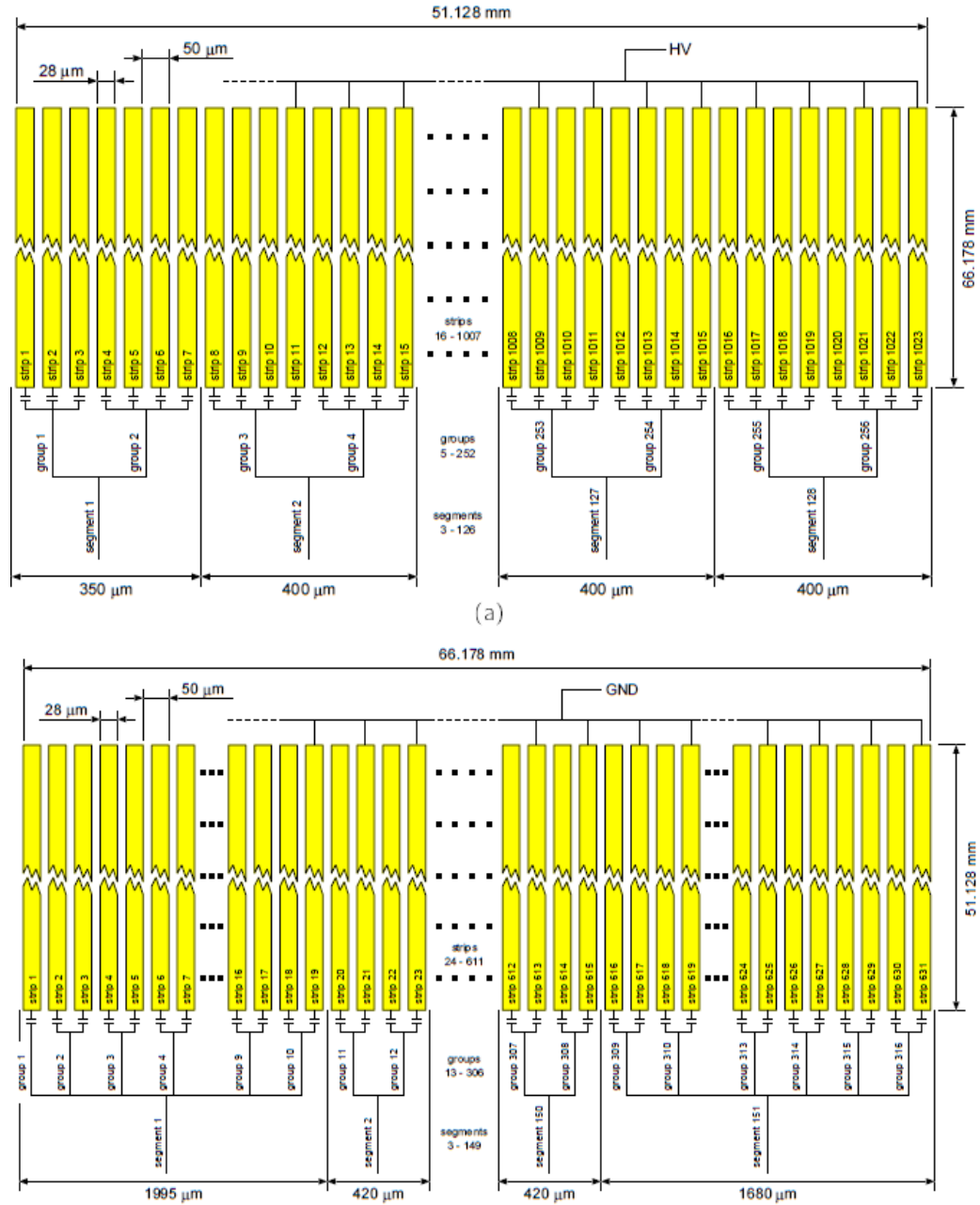


**Figure A.1:** Geometry and connection scheme of the P-doped (a) and N-doped (b) side of the so-called BaBar IV detector.

group composed of three elements. The detector is connected to the front-end electronics by means of a Kapton foil where the 256 strip groups resulting from the described grouping are again sorted in 128 segments. For the n-side of the detector the grouping process is carried out in a different way: the first strip is not grouped at all while the remaining 630 are grouped two by two, resulting in the end in 316 groups. Then the first 10 groups are combined together to constitute the first segment of the Kapton foil while the other segments are each obtained combining two groups; the remaining 8 groups are combined in the last segment.

## A.2 Thick detectors (5500 $\mu m$ )

The thick detector has been developed at the laboratory of the Nuclear Physics Institute (IKP) of the Jülich Research Center (FZ-Jülich) and it is a lithium drifted silicon detector ( $Si(Li)$ )<sup>2</sup>. Its thickness is of about 5.1mm as already mentioned, its active area is  $64 \times 64mm^2$  and the strip pitch is  $666\mu m$  on both sides, which means 96 strip for each side (in fig.A.2 the thick detector connection scheme is drawn, it is easy to see how it is far simpler than the thin detectors connection scheme). Theoretically the voltage needed to achieve the full depletion of the detector is 300V but bias voltages up to 1000V are to be preferred in order to minimize the collection time. Moreover the system is provided with an in-vacuum capacitive divider board which is needed to match the detector signal to the input range of the electronics (even if the input range of the amplifier chips of the front-end is rather large) and in addition to decouple the signals from the high voltage side of the detector. The use of the thick detector as outermost telescope layer grants an operation range of 46MeV for protons and of 62MeV for deuterons.

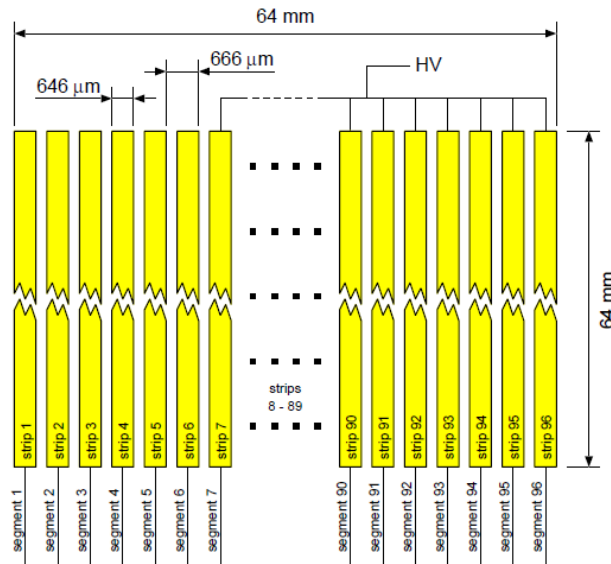


**Figure A.2:** Geometry and connection scheme for both sides of the Lithium drifted  $Si(Li)$  detector.

### A.3 Front-end electronics

As already mentioned in §3.3.7 a vacuum compatible front-end board was developed at the IKP institute to meet the requirements of the detection system employed at the ANKE-IP. The main tasks to deal with were the minimization of the number of feedtroughs between the in-vacuum detectors and the outer DAQ framework and, the most challenging, dealing with the signals coming from the detectors which work in a rather wide energy range.

For that reason the VA32TA chip was conceived in collaboration with the company IDEAS. The chip was built combining two already existent chips: the VA32HDR preamplifier chip, and the TA32cg chip called *trigger chip*, the block scheme of the result is represented in fig.A.3.

The VA32TA chip presents 32 identical channels each connected in parallel to both the amplifying branch (slow branch) and the trigger branch (fast branch) of the chip, in that way a signal provided on one channel is amplified at the preamplifying stage and then split in two part that are sent in parallel to the two chip sections.

In the amplification stage the signal is fed to a  $2\mu s$  pulse generator

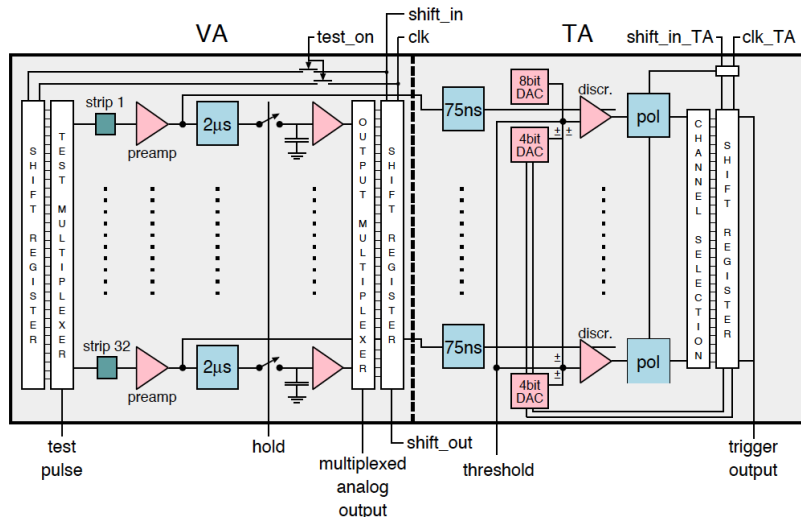


**Figure A.3:** Block scheme of the VA32TA front-end amplifier chip.

(usually called shaper). When the readout cycle begins, that is when the *hold* signal is applied, the output of each shaper is stored in the *sample and hold* frame. When the *shift\_in* and *clk* signals are active (or *high*) one control bit is sent to the readout register which drives the first channel of the output multiplexer to the output bond pad. The *clk* signal gives the timing<sup>1</sup> to shift the control bit through the following remaining registers, connecting one channel per time to the output pad. Each channel is then driven to the output of the chip for a minimum amount of time of  $100ns$ . The VA32TA chips are made foreseeing the possibility to combine them on a daisy chain: the output of the shift register is connected to the *shift\_out* pin. In this way up to ten chips can be organized in a daisy chain in order to get a total number of 320 channels to be serially read. To manage the readout of a chip chain the control signal must be provided simultaneously to all the chips of the chain and the shift register output of one chip must be driven into the *shift\_in* input of the chip next in the chain.

In the trigger stage the signal is shaped with a peaking time of  $75ns$  and then matched with a threshold in order to possibly generate a trigger signal. Each channel is provided with its own threshold level which is the result of the combination of three voltages levels: an external voltage, a chip offset

<sup>1</sup>According to the specifications the maximum clock frequency is  $10MHz$ .

and a channel offset (the last two offset are controlled by a slow control shift register). As it works for the amplification section of the chip, the trigger signals are driven out from the trigger section of the chip by means of a shift register which is in charge of connecting the channels lines to the trigger output pin of the chip; the shift register is controlled by the control signals *clk\_TA* and *shift\_in\_TA*. Moreover in the trigger branch it is possible to exclude separately each channel from the trigger pattern. Furthermore each chip is equipped with a 7-bit digital-to-analog converter (DAC) in order to shift the average of its output level. This feature is particularly of use when many chips are bonded in a daisy chain and there is a major chance that the range of the average output levels of the chips is wide. The DAC is controlled by the control signals as well and it is an extension of the slow control shift register.

Each front-end board hosts five VA32TA chips connected in a daisy chain for a total of 160 chip inputs channels, 9 of which are left floating since the maximum number of output channels of a detector side is 151.

In order to connect the vacuum compatible front-end board to the data acquisition system an additional board has been developed, the so-called repeater board. Moreover this second board decouples the in-vacuum electronics, which can be supplied with high voltage, from the readout electronics. Each vacuum front-end board is served by one repeater board which is equipped with a bus employed to receive the slow control commands from the DAQ system and then to send them to the VA32TA chips; the same bus carries the readout signals coming from the front-end board. The repeater board hosts an 8-channel 12-bit DAC which works as generator of the bias voltages for the chips and at the same time as common threshold for one detector side.

The repeater board exploits the connection between the detector sides and the DAQ system, indeed the signals coming from the detectors are driven to two LEMO connectors as differential signals by a second stage adjustable amplifier embedded on the board, while the trigger output is driven to a third LEMO connector without any previous elaboration stage.

Whenever the DAQ system is processing a signal, it sends to the chips of the front-end boards a *hold* signal in order to prevent the incoming of new signals to process. The repeater board can manage the delay time which elapses between the *hold* signal coming from the DAQ and the *hold* signal which will be sent to the VA32TA chips, this feature is supposed to optimize the charge collection made by the detector.

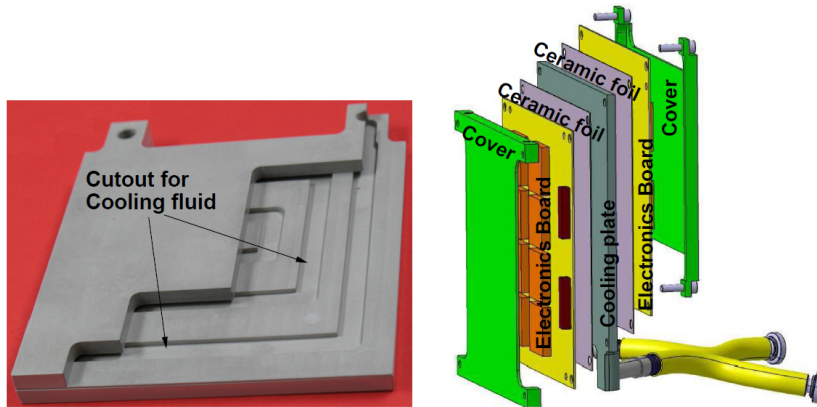


**Figure A.4:** Cooling plate. Left side: half cut which makes visible the bended cutout for the cooling fluid. Right side: Explosion pictures of the front-end cooling system. From left to right are visible a cover, an electronic board, a ceramic foil, a cooling plate, a ceramic foil, an electronic board and a cover.

## A.4 Cooling

A cooling system is required since a constant temperature of the equipment is fundamental for stable operating conditions. Each detector is served by two front-end boards (one board per side) which are mounted behind the detector itself. The two boards are connected to a cooling plate via ceramic foils and shielded by cover plates; a scheme of the configuration of the system is drawn in figure A.4. The temperature gradient on the board must be minimized, the best working condition in order to get a constant energy response from the chips would be to have a drift of the temperature smaller than  $5K$ .

When it comes to the detectors two main issues must be taken into account: the reduction of the dark current (and of the noise as a consequence), and the stabilization of the charge collection process (which means short time and maximum charge collection<sup>2</sup>). The dark current  $I_{dark}$  and the drift velocity  $v_{e^-}$  ( $v_h$ ) of the electrons (holes) are related to the temperature by

<sup>2</sup>Usually this condition is satisfied by stabilizing the time that elapses between the very moment when a particle hits a detector side and the moment when the maximum of the collected charge reaches the preamplifier of the chip.

the equations:

$$I_{dark} \propto T^2 \cdot e^{-\frac{0.62eV}{k_B \cdot T}} \quad (\text{A.1})$$

$$v_{e^-} = 2.1 \cdot 10^{-9} \frac{cm^2}{Vs} \cdot \frac{U}{d} \cdot (T/K)^{-2.5} \quad (\text{A.2})$$

$$v_h = 2.3 \cdot 10^{-9} \frac{cm^2}{Vs} \cdot \frac{U}{d} \cdot (T/K)^{-2.7} \quad (\text{A.3})$$

where  $U$  is the bias voltage,  $d$  the thickness of the detector,  $T$  the temperature of the detector and  $k_b$  the Boltzmann constant: it becomes clear that the detector temperature should be as low as possible in order to ensure good performances. The cooling process is accomplished carrying the cooling fluid as close as possible to the area that must be cooled down, so a mixture of ethanol and water is constantly pumped through the pipes which carry it to the alluminum cooling plate (see fig.A.4) that is where the heat exchange takes place. The cooling fluid is usually kept at the temperature of  $-20^\circ C$ .

## A.5 Assembly

The assembly of the telescopes has been conceived pursuing the aim of the high modularity. Two front-end boards are assembled in a unique structure together with their cooling system and with the detector they serve, as can be seen in figure A.4 and figure A.5. Each detector is mounted on an alluminum frame and each frame is then screwed to the frame of the layer next to it by means of four supports<sup>3</sup>, in this way the telescope structure is assembled. On the frame of the thick detector is fixed one additional cooling plate because the leakage current is not negligible in this case and moreover it grows exponentially with the temperature, this would lead to big damages without additional heat draining.

Each telescope is installed on a CF-DN flange, the whole system is fixed with two *h7 dowel pins* in order to ensure a good mechanical precision. The front-end boards of the detectors are mounted in the rearmost position of the telescope (to avoid the interference with the particle detection) in reverse order with respect to the order in which the detectors are mounted,

---

<sup>3</sup>Many detectors frame have been produced which differs only in the length of their supports in order to allow to adjust the distance between the telescope layers.

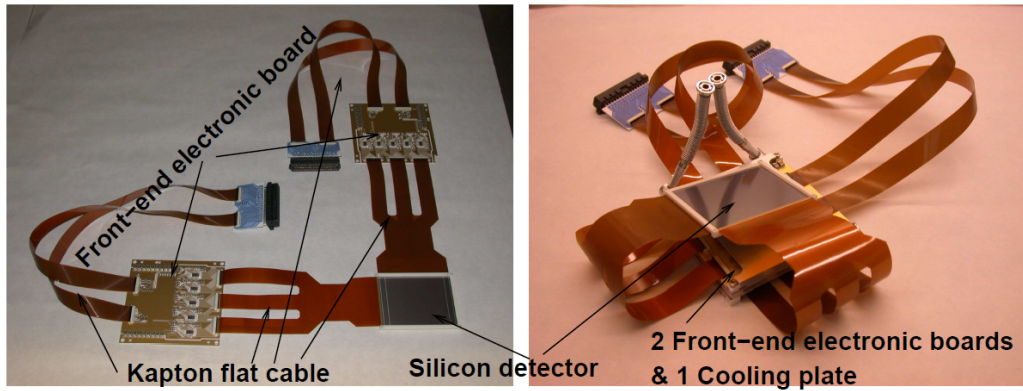


**Figure A.5:** Left side: one detector with its front-end electronic boards bonded by the Kapton flat cables. Right side: complete assembly of one detector with the front-end cooling plate.

with the purpose to not overlap the kapton cables that connect the detectors with their front-end boards.

## A.6 Geometry

Since the polarization has to be measured with the method of the left/right asymmetry in proton-deuteron elastic scattering, the position of the detector is chosen accordingly to few constraint:

- the setup must be aligned so that the protons and deuterons tracks lie in the detection system acceptance;
- in order to implement the double ratio method the detector setup must be  $\phi$ -symmetric;
- the statistical error which afflicts the beam polarization measurement should be small when the luminosity is kept constant;
- the detector must not be placed very close to the beam to reduce the chance of radiation damage.

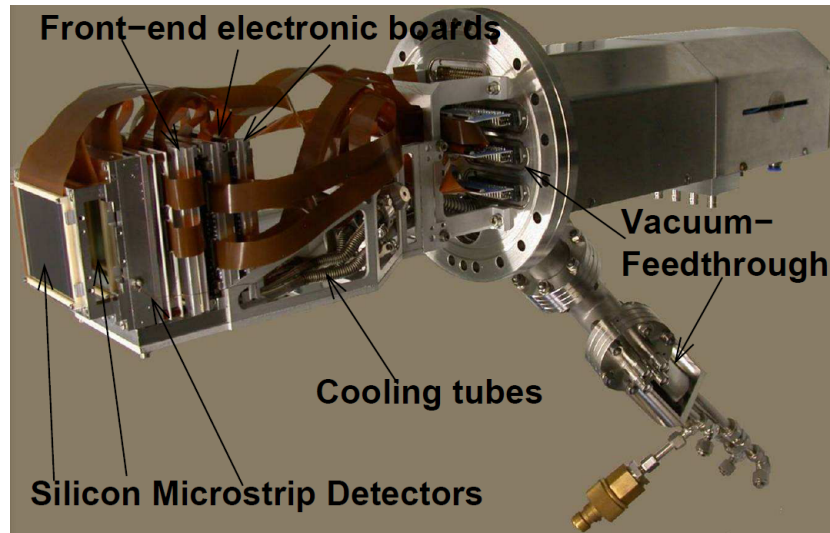


**Figure A.6:** Silicon tracking telescope. Three silicon detectors are visible along with their front-end electronic boards connected by the Kapton flat cable.

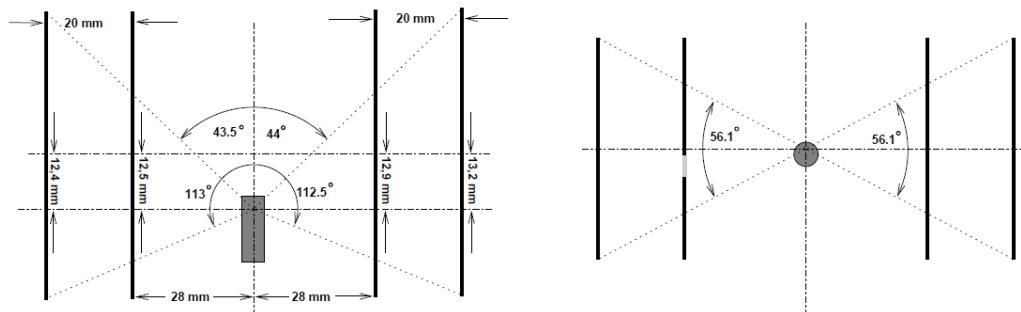


**Figure A.7:** Left side: Schematic top view of the detection setup (the beam points upward). Right side: schematic view of the detection setup from the beam direction. The given angles indicate the geometrical acceptance for the scattering angle  $\theta$  and the azimuthal angle  $\phi$ . The gray detector region indicates a region which is not properly working due to a direct hit of the proton beam.

The whole telescopes setup is located  $12\text{mm}$  downstream<sup>4</sup> with respect to the beam-target interaction point, the innermost layers are located at  $28\text{mm}$  to the center of the beam pipe, the distance between the first and the second layer is of  $20\text{mm}$  and the distance between the second and the third layer is of  $16.5\text{mm}$ . This setup is corroborated by Monte-Carlo simulations which show that the geometrical acceptance is optimized by the described configuration.

To prevent the detectors from the damages that could come from the radiations, a copper layer is placed along the beam pipe  $36\text{cm}$  upstream with respect to the interaction point. The copper layer is  $50\text{mm}$  thick and has a round hole of  $55\text{mm}$  inner diameter which allows the beam to pass through and which is supposed to stop all the secondary particles produced by the beam.

---

<sup>4</sup>*Downstream* with respect to a point along the beam pipe means after that precise point toward the beam circulating direction, while *upstream* means before that precise point.



# List of Figures

1.1	(a). The kinematic region covered by the $\Delta_{Tq}$ measurements at PAX in phase II. In the asymmetric collider scenario antiprotons of $15\text{ GeV}/c$ impinge on protons of $3.5\text{ GeV}/c$ at c.m. energies of $s \sim 200\text{ GeV}^2$ and $Q^2 > 4\text{ GeV}^2$ . (b). The expected asymmetry as a function of Feynman $x_F$ for different values of $s$ and $Q^2 = 16\text{ GeV}^2$ . . . . .	16
1.2	Predicted single-spin asymmetry $A_y = P_y$ for $\theta = 45^\circ$ in the time-like region for selected form factor fits [32]. . . . .	18
2.1	(a). Asymmetry (right scale) and polarization (left scale) measured after filtering the beam in the TSR for different times $t$ . The solid lines are based on an assumed rate of polarization build-up of $1.24 \times 10^{-2}\text{ h}^{-1}$ , which corresponds to $\tau_1 = 80\text{ h}$ . The dashed lines are based on the expected build-up rate ( $\tau_1 = 42\text{ h}$ ) and assumed polarization lifetime of $\tau_p = 81\text{ min}$ [17]. (b). FILTEX experimental setup. . . . .	28
2.2	The polarizing cross section $\sigma_1$ plotted versus the kinetic energy. Indicated is the TSR measurement of FILTEX (red) and the working energy area for spin-filtering at COSY (blue strip). . . . .	31
2.3	The dependence of $\sigma_1$ and $\sigma_2$ ( $mb$ ) on $T_{lab}$ as well as the dependence of $\sigma_1^{int}$ and $\sigma_2^{int}$ ( $mb$ ) (interference contributions) on $T_{lab}$ . The acceptance angles in the lab frame are $\theta_{acc}^{lab} = 10\text{ mrad}$ (solid curve), $\theta_{acc}^{lab} = 20\text{ mrad}$ (dashed curve) and $\theta_{acc}^{lab} = 30\text{ mrad}$ (dashed-dotted curve) [29]. . . . .	33

- 2.4 The dependence of the beam polarization  $P_B(t_0)$  for a target polarization  $P_T = 1$  on  $T_{lab}$  (MeV) for  $P_{\perp} = 0$  and  $P_{\parallel} = 1$ . The acceptance angles in the lab frame are  $\theta_{acc}^{lab} = 10$  mrad (solid curve),  $\theta_{acc}^{lab} = 20$  mrad (dashed curve) and  $\theta_{acc}^{lab} = 30$  mrad (dashed-dotted curve) [29]. . . . . 33
- 3.1 The COSY ring. In green are highlighted the internal experiments and the electron cooler, while in grey one external experiment. The detail of the PAX interaction point is shown in the expansion. . . . . 35
- 3.2 In the straight section the COSY ring, opposite to the electron cooler, the PAX polarized target installation is located, the RF solenoid of the spin-flipper is located in one of the arcs, its use is further clarified in the text of the report. Behind the electron cooler the detector setup for the beam polarimetry is shown. . . . . 37
- 3.3 Schematic representation of a typical spin-filtering cycle. The black curves represent the beam current, while the red ones show the polarization, induced in the beam. While the beam current decreases, the polarization in the beam builds up. At the end of the spin-filtering cycle the spin-flipper was switched on twice to allow for the measurement of the polarization. In the picture, two cycles for different orientations of the target holding field are indicated. . . . . 38
- 3.4 PAX installation at COSY ring: in yellow the already existing COSY straight section quadrupole magnets and in blue the four additional quadrupoles needed for the low- $\beta$  section. Mounted above the target chamber is visible the atomic beam source. . . . . 40
- 3.5 (a). Measurement of the beam polarization lifetime. A polarized proton beam has been injected in the ring and its polarization measured at injection and after a storing period of 5000 s in the ring. From the comparison of the two values the beam polarization lifetime could be deduced. (b). Measurement of the spin-flipper efficiency. The spin-flipper efficiency has been determined by injecting a polarized beam and comparing its polarization at injection and after 99 induced spin-flips. . . . . 41

3.6	PAX target. (a). On the top of the target chamber the ABS is installed. Inside the target chamber the storage cell is hosted. On the right side of the chamber is mounted the BRP. (b). Schematic view of the target setup with the sextupole magnet system and the radio-frequency transition units. . . .	42
3.7	Online screen shot of the target polarization from the Lab-view control program. Both the atomic beam polarization (lower plot with white points) and the atomic fraction (upper plot with blue points) were continuously monitored by the Breit-Rabi polarimeter and the Target Gas Analyzer, respectively. . . . .	43
3.8	Schematic view of the target chamber on top of the newly installed NEG pump. Left and right to the target chamber the fast closing shutter valves can be seen as requested by the CERN vacuum regulation. Right panel: inner view of the NEG pump. The NEG cartridges are mounted on the bottom of the chamber; the opened mechanical shutter is clearly visible. . . . .	46
3.9	Schematic view of the ANKE cluster target. . . . .	48
3.10	Experimental setup for the measurement of the beam polarization as it was already used during the beam time. The cluster target beam comes from the top and crosses the polarized proton beam stored in the machine. Elastically scattered deuterons are detected by a couple of silicon telescopes. . . .	49
3.11	Schematic top view of the telescopes setup at the ANKE interaction point. . . . .	49
4.1	A global view of the PAX trigger board. The front panel connection are described and some of the onboard chips are highlighted. It is not possible to see the complete set of PPGs and PDLs because part of them is installed on the other side of the board. . . . .	54
4.2	DACs pin layout. . . . .	55
4.3	Layout of the programmable timing devices. . . . .	57
4.4	Trigger board GUI. . . . .	60

4.5	Logic scheme of the PAX_TB. The DACs are showed in blu color, the PPGs in yellow and the PDLs in green. All the logic gates presented in this picture are implemented in the CPLD embedded on the trigger board as well as the Look Up Tables. The different kinds of input/output connections are depicted with different symbols in order to separate inputs from outputs and to distinguish between the two kind of outputs (NIM/ECL). . . . .	63
4.6	Jitter tests setup. . . . .	65
4.7	The TDC runs constantly and records the time position of the signals for a defined time interval (collection window). In case a trigger signal falls in the collection window range, the time positions recorded by the TDC are stored and sent to the DAQ labeled by the trigger signal which started the process. In case no trigger signal comes before the collection window time is elapsed, the recorded data are deleted and a new collection stage begins. . . . .	66
4.8	L1N trailing edge time distribution – PPGs . . . . .	70
4.9	L1N trailing edge time distribution – PDLs . . . . .	71
4.10	Crosstalk tests setup. . . . .	72
4.11	Crosstalk results . . . . .	74
4.12	Test bench scheme – Jitter tests. . . . .	75
4.13	S/R Flip-Flop. . . . .	77
4.14	Flip-Flop jitter. One of the best way to generate a pulse which is almost not affected by jitter is to employ an S/R Flip-Flop and cables of different length, but there are aspects which must be taken into account. The rising slope of a real pulse edge (b) combined with the measurable amplitude of the Flip-Flop activation threshold (which in the ideal case is supposed to be a line and have no thickness (a)), is one of the jitter causes. The sum of these two effects results in the definition of a time interval in which the Flip-Flop set (reset) process can occur (b). This is the reason why the time position of the edges of the pulse generated by the Flip-Flop is affected by a sort of uncertainty. . . . .	78
4.15	Trailing edge time distribution – $Ch0$ . . . . .	80
4.16	Trailing edge time distribution – $Ch1$ . . . . .	81
4.17	Trailing edge time distribution – $Ch1$ & $Ch2$ . . . . .	82

<i>LIST OF FIGURES</i>	113
4.18 Test bench scheme – Crosstalk tests tdc. . . . .	83
4.19 Test bench scheme – Crosstalk tests. . . . .	84
4.20 Crosstalk results. . . . .	85
4.21 STTs trigger apparatus scheme. . . . .	86
4.22 Silicon tracking telescopes setup scheme. . . . .	87
4.23 First phase: the distribution patterns of the look up tables histograms are influenced by the fact that only the L1 channel could gate the trigger output. The difference between the (c) and (e) histograms is that the first is filled by ( $L1$ or $L2$ ) events while the second is filled by ( $L1$ and $\overline{L2}$ ) events. The narrow peak of the (a) histogram and the absence of the tail is due to the fact that the NIM trigger is the signal which triggers the TDCs data acquisition. Anyway the width of the peaks of the (d) and (f) histograms is comparable to the width of the peak of the (b) histogram. . . . .	91
4.24 Second phase: the distribution patterns of the look up tables histograms are influenced by the fact that only the L2 channel could gate the trigger output. The difference between the (c) and (e) histograms is that the first is filled by ( $L1$ or $L2$ ) events while the second is filled by ( $\overline{L1}$ and $L2$ ) events. The presence of a double peak in the (d) histogram could be due to the master channel choice, this is supported by the fact that the (f) histogram has only one peak. Also in this case the width of the peaks of the (d) and (f) histograms is comparable to the width of the peak of the (b) histogram. . . . .	92

4.25	Third phase: the distribution patterns of the look up tables histograms are influenced by the fact that both L1 and L2 channels could gate the trigger output. The difference between the (c) and (e) histograms is that the first is filled by ( <i>L1 or L2</i> ) events while the second is filled by ( <i>L1 and L2</i> ) events, extremely rare coincidences if compared to the number of event generated by the NIM apparatus. Even in this case the presence of a double peak in the (d) histogram could be due to the master channel choice. The (f) histogram shows two peaks too and a closer look at the histogram (4.23f) and (4.24f) reveals that this two peaks are in the same position of those single peaks. Also in this case the width of the peaks of the (d) and (f) histograms is comparable to the width of the peak of the (b) histogram. . . . .	93
A.1	Geometry and connection scheme of the P-doped (a) and N-doped (b) side of the so-called BaBar IV detector. . . . .	98
A.2	Geometry and connection scheme for both sides of the Lithium drifted <i>Si(Li)</i> detector. . . . .	100
A.3	Block scheme of the VA32TA front-end amplifier chip. . . . .	101
A.4	Cooling plate. Left side: half cut which makes visible the bended cutout for the cooling fluid. Right side: Explosion pictures of the front-end cooling system. From left to right are visible a cover, an electronic board, a ceramic foil, a cooling plate, a ceramic foil, an electronic board and a cover.	103
A.5	Left side: one detector with its front-end electronic boards bonded by the Kapton flat cables. Right side: complete assembly of one detector with the front-end cooling plate. .	105
A.6	Silicon tracking telescope. Three silicon detectors are visible along with their front-end electronic boards connected by the Kapton flat cable. . . . .	106
A.7	Left side: Schematic top view of the detection setup (the beam points upward). Right side: schematic view of the detection setup from the beam direction. The given angles indicate the geometrical acceptance for the scattering angle $\theta$ and the azimuthal angle $\phi$ . The gray detector region indicates a region which is not properly working due to a direct hit of the proton beam. . . . .	106

# Bibliography

- [1] H.Ströher, *Proceedings of the 17th Intl. Spin Physics Symposium, SPIN2006*, Kyoto, Japan, (October 2006).
- [2] Spokespersons: P.Lenisa and F.Rathmann, *PAX technical proposal for the HESR at FAIR*, Jülich 2004, e-Print Archive: hep-ex/0505054 (for updates see <http://www.fz-juelich.de/ikp/pax>).
- [3] *Proc.of the Workshop on Polarized Antiproton*, Bodega Bay, CA, (1985), Eds.A.D.Krisch, A.M.T.Lin, and O.Chamberlain, AIP Conf.Proc.145 (AIP, New York,1986).
- [4] *Proceedings Workshop on Polarized Antiproton Beams. How?*, Daresbury, UK, (2007), AIP Conf.Proc.1008 (2008).
- [5] 409. WE-Heraeus-Seminar Polarized Antiprotons, Organizers: Dr. Paolo Lenisa and Dr. Frank Rathmann, 23-25 June 2008. <http://www.fe.infn.it/heraeus/>
- [6] E.Steffens, *Short History of Polarized Antiprotons*, AIP Conf.Proc.1008, 1 (2008).
- [7] E.Steffens and W.Haeberly, *Polarized Gas Targets*, Rep.Prog.Phys.66, 1887 (2003).
- [8] E.Steffens et al., Proc.3<sup>rd</sup> LEAR Workshop, 245 (1985), Tignes and CERN Proposal CERN/PSCC/85-80 (Nov. 5, 1985).
- [9] D.P.Grosnick et al., *The design and performance of the FNAL high-energy polarized-beam facility*, Nucl.Instrum.Meth.A290, 269 (1990).

- [10] H.Spinka et al., *Proceedings of the 8<sup>th</sup> International Symposium on Polarization Phenomena in Nuclear Physics*, Bloomington, Indiana, (1994), Eds.E.J.Stephenson and S.E.Vigdor, AIP, Conf.Proc.339, 713 (AIP, Woodbury, NY, 1995).
- [11] A.Nass et al., *The HERMES polarized atomic beam source*, Nucl.Instr.Meth.A505, 633 (2003).
- [12] H.Arenhovel, *Coulomb effects in polarization transfer in elastic antiproton and proton electron scattering at low energies*, Eur.Phys.J A 34, 303 (December 2007).
- [13] Th.Walcher et al., *A surprising method for polarizing antiprotons*, Eur.Phys.J A 34, 447 (2007).
- [14] Th.Walcher et al., *Erratum, a surprising method for polarizing antiprotons*, Eur.Phys.J bf A 39, 137 (2009).
- [15] D.Oellers et al., *Polarizing a stored proton beam by spin-flip?*, Phys.Lett.B 674, 269 (2009).
- [16] P.L.Csonka, NIM 63 247 (1968).
- [17] F.Rathmann et al. *New method to polarize protons in a storage ring and implications to polarize antiprotons*, Phys,Rev,Lett.71 1379 (1993).
- [18] H.O.Meyer, *Effect of a polarized hydrogen target on the polarization of a stored proton beam*, Phys.Rev.E50 1485 (1994).
- [19] C.J.Horowitz and H.O.Meyer, *Polarizing stored beams by interaction with polarized electrons*, Phys.Rev.Lett.72 3981 (1994).
- [20] A.I.Milstein and V.M.Strakhovenko *Polarizing mechanisms for stored  $p$  and  $\bar{p}$  beams interacting with a polarized target*, Phys.Rev.E72 066503 (2005).
- [21] N.N.Nikolaev and F.F.Pavlov *Spin Filtering in Storage Rings, and Polarization Buildup of Stored Protons and Antiprotons: Filtex Result and Implications for Pax at Fair*, e-Print Archive: hep-ph/0512051 (2005), hep-ph/0601184 (2006).

- [22] A comprehensive review about the transverse spin structure of the proton can be found in V.Barone, A.Drago and P.Ratcliffe, *Phys.Rep.*359, 1 (2002).
- [23] J.Collins, *Fragmentation of transversely polarized quarks probed in transverse momentum distributions*, *Nucl.Phys.*B396, 161 (1993).
- [24] A.Airapetian et al. (HERMES Collaboration), *Single-Spin Asymmetries in Semi-Inclusive Deep-Inelastic Scattering on a Transversely Polarized Hydrogen Target*, *Phys.Rev.Lett.*94, 012002 (2005).
- [25] E.S.Ageev et al. (COMPASS Collaboration), *A new measurement of the Collins and Sivers asymmetries on a transversely polarised deuteron target*, *Nucl.Phys.*B765, 31 (2007).
- [26] R.Seidl et al. (Belle Collaboration), *Measurement of Azimuthal Asymmetries in Inclusive Production of Hadron Pairs in  $e^+e^-$  Annihilation at Belle*, *Phys.Rev.Lett.*96, 232002 (2006).
- [27] M.Anselmino et al., *Transversity and Collins functions from SIDIS and  $e^+e^-$  data*, *Phys.Rev.*D75, 054032 (2007).
- [28] V.Barone, T.Calarco and A.Drago, *Double-spin transverse asymmetries in Drell-Yan processes*, *Phys.Rev.*D56, 527 (1997).
- [29] V.F.Dimitriev, A.I.Milstein and S.G.Salnikov, *Spin-dependent part of  $p\bar{p}$  interaction cross section and Nijmegen potential*, *Phys.Lett.*B690, 427 (2010).
- [30] Y.N.Uzikov and J.Haidenbauer, *Spin-dependent  $\bar{p}d$  cross sections at low and intermediate energies*, *Phys.Rev.*C79, 024617 (2009).
- [31] A.Kaidalov, L.Kondratyuk and D.Tchein, *Electromagnetic Pion and Nucleon Form Factors at Positive and Negative  $q^2$  Within the Framework of Quark-Gluon Strings Model*, *Phys.Atom.Nucl.*63, 1395 (2000).
- [32] S.J.Brodsky, C.E.Carlson, J.R.Hiller and D.S.Hwang, *Single-spin polarization effects and the determination of timelike proton form factors*, *Phys.Rev.*D69, 054022 (2004).
- [33] H.W.Hammer, U.G.Meissner and D.Drechsel, *Dispersion-theoretical analysis of the nucleon electromagnetic form factors: Inclusion of time-like data*, *Phys.Lett.*B385, 343 (1996).

- [34] S.Dubnicka and A.Z.Dubnickova, *Jlab Proton Polarization Data in Aspect to Global Unitary and Analytic Model of Nucleon Electromagnetic Structure*, *Fizika B* 13, 287 (2004).
- [35] M.Ambrogiani et al. (E835 Experiment), *Measurements of the magnetic form factor of the proton in the timelike region at large momentum transfer*, *Phys.Rev.D*60, 032002 (1999).
- [36] M.K.Jones et al.,  *$G_{E_p}/G_{M_p}$  Ratio by Polarization Transfer in  $\vec{e}p \rightarrow e\vec{p}$* , *Phys.Rev.Lett.*84, 1398 (2000).
- [37] A.Z.Dubnickova, S.Dubnicka and M.Rekalo, *Investigation of the baryon electromagnetic structure by polarization effects in  $e^+e^- \rightarrow B\bar{B}$  processes*, *Nuovo Cim.*A109, 241 (1966).
- [38] E.Tomasi Gustafsson and M.Rekalo, *QCD-view on hadron form factors in space-like and time-like momentum transfer regions*, e-Print arXiv: nucl-th/0307065.
- [39] E.Klempt, F.Bradamante, A.Martin and J.M.Richard, *Antinucleon-nucleon interaction at low energy: scattering and protonium*, *Phys.Rep.*368, 119 (2002).
- [40] J.R.O'Fallon et al., *Spin Spin Interactions of High- $P_{\perp}^2$  Elastic  $p-p$  Scattering*, *Phys.Rev.Lett.*39, 733 (1977).
- [41] D.G.Crabb et al., *Spin Dependence of High- $P_{\perp}^2$  Elastic  $p-p$  Scattering*, *Phys.Rev.Lett.*41, 1257 (1978).
- [42] H.A.Neal and H.B.Nielsen, *A recurrence relation for the polarization in elastic  $p-p$  scattering in the framework of a parton model*, *Phys.Lett.*B51, 241 (1974).
- [43] H.A.Neal, J.B.Kuah and H.B.Nielsen, *Studies of elastic  $p-p$  polarization and differential cross section in a simple parton scattering model*, *Phys.Lett.*B439, 407 (1998).
- [44] J.P.Ralston and B.Pire, *Comment on "Energy Dependence of Polarization Effects in Exclusive Hadron Scattering"* *Phys.Rev.Lett.*57, 2330 (1986).
- [45] G.P.Ramsey and D.W.Sivers, *NN scattering amplitudes from  $90^\circ$  c.m. into the Landshoff region*, *Phys.Rev.D*52, 116 (1995).

- [46] S.J.Brodsky and G.F.de Teramond, *Spin Correlations, QCD Color Transparency, and Heavy-Quark Thresholds in Proton-Proton Scattering* Phys.Rev.Lett.60, 1924 (1988).
- [47] N.King et al., *Polarization in proton-deuteron scattering at 50 MeV*, Phys.Lett.69B, 151 (1977).
- [48] K.Zapfe et al., *Detailed studies of a high-density polarized hydrogen gas target for storage rings*, Nucl.Instrum.Meth.A368, 293 (1996).
- [49] K.Zapfe et al., *High density polarized hydrogen gas target for storage rings*, Rev.Sci.Instrum.66, 28 (1995).
- [50] J.Bystricky, F.Lehar and P.Winternitz, *Formalism of nucleon-nucleon elastic scattering experiments*, J.Phys.(France)39, 1 (1978).
- [51] S.Bilenky and R.Ryndin, *On the total cross sections for reactions with polarized beams and polarized targets*, Phys.Lett.6, 217 (1963).
- [52] M.Ukhanov, *Polarized Antiprotons Beams – How?*, An International Workshop, Warrington, UK, 2007, AIP Proceedings, 1008 (2008).
- [53] F.L.Shapiro, *Nuclear Structure Studies with Neutrons*, Proc.Int.Conf.Study of Nuclear Structure with Neutrons, 588 Antwerp (1965), NL, Amsterdam (1966).
- [54] G.A.Keyworth and J.R.Lemley, Proc.3<sup>rd</sup> Int.Symp.on Polarization Phenomena in Nuclear Reactions, 873 (1970), Madison.
- [55] K.P.Coulter et al., *Neutron polarization with a polarized  $^3\text{He}$  spin filter*, Nucl.Instr.Meth.A288, 463 (1990).
- [56] SAID, *Nucleon Nucleon Scattering Database*, available from Center For Nuclear Studies, Department of Physics, George Washington University, USA, website <http://gwdac.phys.gwu.edu/analysis/nnanalysis.html>.
- [57] Dr.H.Soltner, private communication.
- [58] K.Kilian and D.Möhl, Proc.2<sup>nd</sup> LEAR Workshop, 701 (1982), Erice.
- [59] A.Musgiller, *Identification and tracking of low energy spectator protons*, Universität zu Köln, (2006).

- [60] D.Oellers, *Polarizing a stored proton beam by spin-flip?*, Universität zu Köln, (2010).
- [61] C.Weidemann, *Preparations for the spin-filtering experiments at COSY/Jülich*, Universität zu Köln, (2011).
- [62] A.Cotta Ramusino, *The PAX Trigger Board (PAX\_TB)*. (March 2009).
- [63] P.Benati, *Caratterizzazione di una nuova scheda di trigger per esperimenti di filtraggio in spin*, 2008.
- [64] Data Delay Devices, Inc., *8-BIT & 12-BIT PROGRAMMABLE PULSE GENERATORS (SERIES 3D7608 & 3D7612: PARALLEL INTERFACE)*, (2007).
- [65] Data Delay Devices, Inc., *MONOLITHIC QUAD 4-BIT PROGRAMMABLE DELAY LINE (SERIES 3D7424)*, (2007).
- [66] Burr-Brown Corporation, *Quad, Serial Input, 12-Bit, Voltage Output DIGITAL-TO-ANALOG CONVERTER*, (2005).

# Acknowledgements

I would like to thank Dr. Paolo Lenisa acting as my supervisor and Prof. Paola Ferretti Dalpiaz for the many advices and contribution to my thesis work. I would also like to thank Prof. Dr. Hans Ströher for his contribution and Dr. Harald Kleines for providing the possibility to perform my work at the ZEL. Moreover I would like to thank Dr. Sergey Trusov and Dr. Sergey Mikirtychiants for the large and evaluable contributions to this work.

I would also mention all my friend one by one but may be it is not a great idea, then thank you all my friends<sup>5</sup>. Last but not least I thank my family: papà, mamma and Cesare.

---

<sup>5</sup>TIB.

.